UiO : University of Oslo

Sigbjørn Løland Bore

Advances in the Hybrid Particle-Field Approach: Towards Biological Systems

Thesis submitted for the degree of Philosophiae Doctor

Department of Chemistry
Faculty of Mathematics and Natural Sciences

Hylleraas Centre for Quantum Molecular Sciences

2020

Series of dissertations submitted to the
Faculty of Mathematics and Natural Sciences, University of Oslo

ISSN ISSN

Cover: Hanne Baadsgaard Utigard.
Print production: Reprosentralen, University of Oslo.

Preface

This thesis is submitted in partial fulfillment of the requirements for the degree of *Philosophiae Doctor* at the University of Oslo. The research presented here is conducted under the supervision of Professor Michele Cascella.

Acknowledgments

I acknowledge the Department of Chemistry at the University of Oslo, the Hylleraas Centre for Quantum Molecular Sciences (Grant No. 262695) and the Norwegian Supercomputing Program (NOTUR) for financial support through a grant of computer time (Grant No. NN4654K).

In the process of writing this thesis, I have received constructive feedback in form of corrections and suggestions. Therefore, I thank the following people: Gaute Linga, Manuel Carer, Thomas K. Sæbøe, Erik Tellgren and David Balcells.

I am very grateful to have been a part two centers of excellence, the Centre for Theoretical and Computational Chemistry and the Hylleraas center for Quantum Molecular Sciences. This has given me the opportunity to meet and learn from a strong community of theoretical chemists and has provided me with excellent working conditions. Special thanks goes to Jan Ingar Johnsen and Trygve Ulf Helgaker, who have been very helpful in terms of everyday logistics.

The work presented in this thesis would not have been possible without my collaborators. Special thanks goes to my Italian and Japanese collaborators Antonio de Nicola, Antonio Pizzirusso, Toshiro Kawakatsu and Giuseppe Milano. They have been exceptionally helpful in sharing their knowledge on hybrid particle-field molecular dynamics and have assisted me in day-to-day operations. At the University of Oslo I would like to especially thank Hima Bindu Kolli, Victoria Ariel Bjørnestad and Morten Ledum. It has been very useful having you working on the same topic as me. I strongly believe that our research output has benefited from us standing together.

Last, but most of all people, I must thank my supervisor, Professor Michele Cascella. We have had many tough scientific discussions, but always with our eyes on the prize.

Oslo, December 2019
Sigbjørn Løland Bore

List of Papers

The thesis is comprised by results included in the following papers.

Paper I: *Hybrid Particle-Field Model for Conformational Dynamics of Peptide Chains*
Sigbjørn Løland Bore, Giuseppe Milano and Michele Cascella
Journal of Chemical Theory and Computation **14**, 1120–1130 (2018)

Paper II: *Hybrid Particle-Field Molecular Dynamics Simulations of Charged Amphiphiles in Aqueous Environment*
Hima Bindu Kolli, Antonio De Nicola, **Sigbjørn Løland Bore**, Ken Schäfer, Gregor Diezemann, Jürgen Gauss, Toshihiro Kawakatsu, Zhongyuan Lu, You-Liang Zhu, Giuseppe Milano and Michele Cascella
Journal of Chemical Theory and Computation **14**, 4928–4937 (2018)

Paper III: *Mesoscale Electrostatics Driving Particle Dynamics in Nonhomogeneous Dielectrics*
Sigbjørn Løland Bore, Hima Bindu Kolli, Toshihiro Kawakatsu, Giuseppe Milano and Michele Cascella
Journal of Chemical Theory and Computation **15**, 2033 (2019)

Paper IV: *Aggregation of Lipid A Variants: a Hybrid Particle-Field Model*
Antonio De Nicola, Thereza A. Soares, Denys E. S. Santos, **Sigbjørn Løland Bore**, G. J. Agur Sevink, Michele Cascella and Giuseppe Milano
Biochimica et Biophysica Acta, in press (2020)

Paper V: *Beyond the Molecular Packing Model: Understanding Morphological Transitions of Charged Surfactant Micelles*
Ken Schäfer, Hima Bindu Kolli, Mikkel Killingmoe Christensen, **Sigbjørn Løland Bore**, Gregor Diezemann, Jürgen Gauss, Giuseppe Milano, Reidar Lund and Michele Cascella
Submitted for peer-review (2020)

Paper VI: *Hybrid Particle-Field Molecular Dynamics Under Constant Pressure*
Sigbjørn Løland Bore, Hima Bindu Kolli, Antonio De Nicola, Maksym Byshkin, Toshihiro Kawakatsu, Giuseppe Milano and Michele Cascella
The Journal of Chemical Physics, in press (2020)

The following papers were published in peer reviewed journals during the course of the PhD, but are not included in the thesis.

- *Coupling Spin to Velocity: Collective Motion of Hamiltonian Polar Particles*
  Sigbjørn Løland Bore, Michael Schindler, Khanh-Dang Nguyen Thu Lam, Eric Bertin and Olivier Dauchot
  Journal of Statistical Mechanics: Theory and Experiment **3**, 033305 (2016)

- High-Resolution Large Time-Step Schemes for Inviscid Fluid Flow
  Sigbjørn Løland Bore and Tore Flåtten
  Applied Mathematical Modelling **81**, 263–278 (2020)

Contents

Chapter 1

Introduction

1.1 State of the art

Can we understand complex biological systems, such as bacterias, organelles and cells, by considering their constituents, the atoms? Such a bottom-up approach is attractive as it offers an understanding at the most fundamental level.

Already in 1929, Paul M. Dirac stated [1]:

> *The underlying physical laws necessary for the mathematical theory of a large part of physics and the whole of chemistry are thus completely known, and the difficulty is only that the exact application of these laws leads to equations much too complicated to be soluble.*

Years of research have strengthened the validity of Dirac's powerful statement. Beyond a single hydrogen atom, the innate complexity of chemical systems makes investigation by pen and paper an intractable endeavor. Since the invention of the transistors and the ensuing informatics revolution in the fifties, major effort has been put into developing reliable computational methods that can deal with complicated chemical and biological systems. This effort has resulted in the establishment of *computational chemistry*. Within this field, the problem of investigating chemical systems by means of theoretical models is solved by algorithms performed by the brute force of computers.

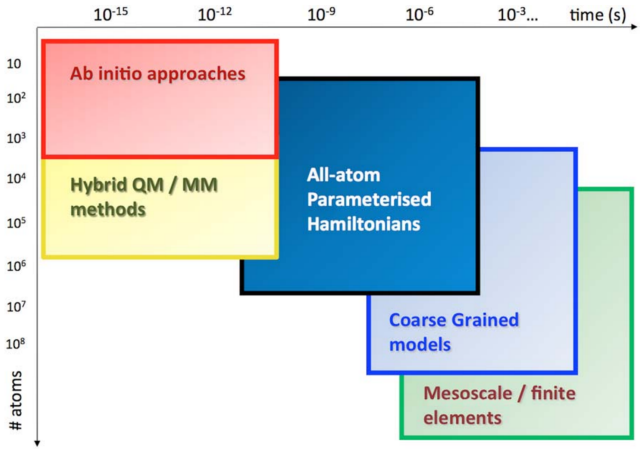

Figure 1.1: Accessible time- and size-scales for different computational methods in routine studies using state of the art implementations and architectures. Reprinted from [2].

The bottom-up approaches of computational chemistry are constituted by a set of methods for modeling of biomolecular phenomena at different resolutions (Figure 1.1). At the most fundamental level, *ab initio* approaches aim to numerically solve the quantum mechanical problem of the *Schrödinger equation* for the electrons of atoms composing the molecular system. Within the limitations of the validity of the Schrödinger equation (nonrelativistic approximation), ab initio approaches offer a route with very few assumptions. The major advances in both methodology (primarily computational cheap *Density functional theory* (DFT) and highly reliable *Coupled-cluster methods*) and software (such as Gaussian [3]), have resulted in an extensive adoption of ab initio modelling. Nevertheless, solving the electronic structure problem for systems beyond thousands of atoms acting over nanoseconds is still computationally expensive. Consequently, even a single biological molecule interacting with solvent quickly becomes intractable[1].

To treat larger molecules interacting with solvent, *all atom parameterized models* (AA) are more appropriate [5]. In AA, the *Born–Oppenheimer approximation* is used to consider the nuclei as point particles, and the interactions between atoms are approximated by simple interaction potentials (force-field). Even though AA reduces the number of degrees of freedom by about one order of magnitude, well parameterized potentials, such as the CHARMM force-field for proteins [6], are sufficiently reliable to predict the folding of proteins, and are used by pharmaceutical companies in drug discovery. Sometimes even, as is the case for liquid water models at room temperature, AA models achieve better modeling water-structure than the ab initio DFT [5].

To date, world-leading groups in molecular simulations have pushed molecular dynamics (MD) studies of proteins to reach time scales in the millisecond range and sizes as big as 10^7 atoms. These technical progresses have allowed researchers to investigate, for example, the folding of several globular proteins [7, 8], to elucidate signal transduction in G-protein coupled receptors [9], and to achieve structural refinement of low-resolution Cryogenic electron microscopy images of the HIV-1 capsid [10]. Nonetheless, these dimensionalities are on one hand not accessible to the broad computational scientific community, and on the other hand not sufficient to cover the scales pertinent to large in vivo macromolecular complexes.

Similarly for lipid bilayers, the progress in both software and hardware has allowed for the expansion of time scales reached by all-atom MD simulations of membranes from the hundreds of picoseconds, reported in the first studies of fully solvated phospholipid bilayers [11], up to microseconds in current simulations [12]. However, the lateral dimensions of MD simulations of lipid bilayers have only marginally increased, remaining confined to box sizes of approximately $10\,\mathrm{nm} \times 10\,\mathrm{nm}$. This limitation not only prevents investigation of large-scale membrane remodeling phenomena that are crucial in cellular pro-

[1] Such methods play however an important role in multiresolution methods, including the QM/MM method [4], where a part of the molecular system is described by quantum mechanics and the rest by classical physics. Multiresolution approaches allow us to simulate much larger system sizes (see Figure 1.1).

cesses, but also does not permit a direct comparison between all-atom bottom-up numerical simulations and continuum theories that historically have been successful in investigating membrane properties at larger scales. Consequently, this thesis considers coarse-grained (CG) modeling [13–15].

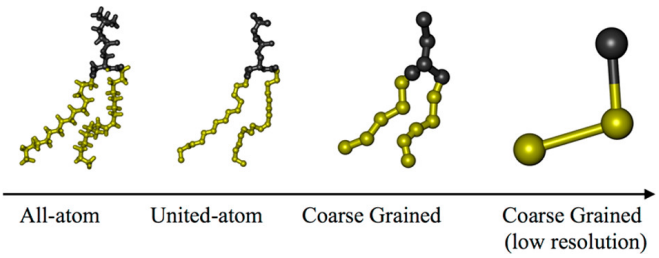

Figure 1.2: Resolutions of description of a Lipid, from AA to CG. Reprinted from [16]

In CG models, a lower resolution representation of the molecular system of interest is obtained by clustering atoms into beads (Figure 1.2), which interact through effective model potentials. While the detailed atomic resolution is lost, some information on the topological structure of the molecular assembly is retained. Computational efficiency is gained by lowering the number of degrees of freedom, which reduces the amount of interactions needed to be computed. Furthermore, the CG-procedure generally leads to a filtering out of high frequency modes present in the AA, thereby speeding up the dynamics. These models can efficiently represent molecular systems composed of several millions of atoms, for effective times that can reach the second scale; they are therefore well-adapted to investigate the structure and dynamics of large macromolecular assemblies and multi-phase systems. Consequently, CG modeling opens up the possibility of bridging the all-atom and mesoscopic scales. However, for the problems of computational efficiency of AA that CG solves, CG introduces new problems to the theoretical modeling: how should the the CG-beads be constructed, and how do we model interactions among the CG-beads?

These questions are partly answered by *statistical physics*. Generally, the statistical properties of a molecular system is determined by the partition function:

$$Z = \int \mathrm{d}\mathbf{\Gamma} \;\; \exp\left[-\beta H\left(\mathbf{\Gamma}\right)\right], \tag{1.1}$$

where $\mathbf{\Gamma}$ is the full set degrees of freedom describing a system subject to Hamiltonian H and $\beta \equiv 1/k_{\mathrm{b}}T$. A rigorous coarse-grained simulation aims at approximating the partition function:

$$Z \simeq \int \mathrm{d}\mathbf{\Gamma}_{\mathrm{CG}} \;\; \exp\left[-\beta H_{\mathrm{CG}}\left(\mathbf{\Gamma}_{\mathrm{CG}}\right)\right], \tag{1.2}$$

where $\mathbf{\Gamma}_{\mathrm{CG}}$ are now the degrees of freedom in the coarse grained representation. Theoretically, an exact relationship exists. Let $\mathbf{M}(\mathbf{\Gamma})$ be the mapping of the

fine grained positions to a CG-site. Using the δ function, we have

$$\begin{aligned} Z &= \int \mathrm{d}\mathbf{\Gamma}\mathrm{d}\mathbf{\Gamma}_{\mathrm{CG}}\ \delta(\mathbf{M}(\mathbf{\Gamma}) - \mathbf{\Gamma}_{\mathrm{CG}}) \exp\left[-\beta H\left(\mathbf{\Gamma}\right)\right] \\ &= \int \mathrm{d}\mathbf{\Gamma}_{\mathrm{CG}}\ \exp\left[-\beta H_{\mathrm{CG}}\left(\mathbf{\Gamma}\right)\right], \end{aligned} \tag{1.3}$$

where we define H_{CG} by:

$$\exp\left[-\beta H_{\mathrm{CG}}\left(\mathbf{\Gamma}_{\mathrm{CG}}\right)\right] \equiv \int \mathrm{d}\mathbf{\Gamma}\ \delta(\mathbf{M}(\mathbf{\Gamma}) - \mathbf{\Gamma}_{\mathrm{CG}}) \exp\left[-\beta H\left(\mathbf{\Gamma}\right)\right], \tag{1.4}$$

or

$$H_{\mathrm{CG}}(\mathbf{\Gamma}_{\mathrm{CG}}) = -\frac{1}{\beta} \ln\left[\int \mathrm{d}\mathbf{\Gamma}\ \delta(\mathbf{M}(\mathbf{\Gamma}) - \mathbf{\Gamma}_{\mathrm{CG}}) \exp\left[-\beta H\left(\mathbf{\Gamma}\right)\right]\right]. \tag{1.5}$$

Although (1.5) is a simple formula from a simple derivation, this formula illustrates many of the complications faced when coarse-graining. Firstly, obtaining H_{CG} requires integrating out microscopic degrees of freedom. This means that entropic contributions to the free energy are absorbed into H_{CG}. Secondly, H_{CG} is a state-dependent function as it depends on temperature, pressure and other system properties, such as concentration of salt and the pH. Finally, for CG to be useful, H_{CG} needs to be simpler and more efficient to compute than H. All of these factors force us to apply approximations and modeling in the search for H_{CG}.

Approaches to CG can be divided into two classes: top-bottom and bottom-up. In top-bottom approaches, H_{CG} is parameterized to reproduce properties of a higher level, such as experimental, thermodynamic and/or structural properties. For example, in the *MARTINI* [17], which is the most widely applied CG-force-field, the *Lennard-Jones potentials* used to model nonbonded interactions, are parameterized to reproduce water/oil-partitioning coefficients. Bottom-up approaches use information from a lower molecular scale to construct H_{CG}. In implicit solvent models (no beads for solvent), salt-salt interactions can be derived to reproduce the radial distribution function by *iterative Boltzmann Inversion* [18] or by *Inverse Monte Carlo* [19]. Also, widely used is the *force-matching* technique developed by, among others, the Voth group [14], where H_{CG} is parameterized to reproduce forces of the lower molecular scale, either from electronic structure calculations or all-atom force fields.

While the usefulness of CG is related to how well H_{CG} is able to accurately approximate (1.2), it is also important to consider its computational efficiency. An introduction of many-body interactions to model H_{CG} can quickly become less efficient than AA. For this reason, H_{CG} is often limited to two-body pair interactions, ignoring many-body terms. For example, the MARTINI force-field models nonbonded interactions with all-atom Lennard-Jones potentials, despite there being little physical justifications for it. Here, the main advantage lies in the computational efficiency which the all-atom MD softwares, such as GROMACS [20], can compute such interactions.

Similar in spirit, and going even one step further in using computational cheap potentials, is the *single chain in mean field method* (SCMF), which is actively being developed in the group of Marcus Müller [21, 22]. The SCMF method models polymers by particle-based coarse-grained polymer chains, subject to intramolecular interactions. Inspired by *self-consistent field theory* (SCFT) for polymers [23–25], the intermolecular interactions between chains are modeled by a purely density-dependent interaction energy. This gives rise to a species-dependent instantaneous inhomogenous external potential, which acts on the chains. Statistical sampling is achieved by Monte Carlo (MC) moves. Since there are no pair interactions, the polymer chains can be efficiently divided among processors, needing only to communicate for the update of the external potential. Because the external potential is a slow changing variable, a multiple time-step approach can be used, where the external potential is kept constant across many MC moves. The achieved net effect is excellent scaling with processors for small and large systems. Recently, a GPU-based implementation reached the milestone of 10 billion particles, outperforming in relaxation of copolymer melts, the state of the art Lennard-Jones based HOOMD-blue software [26, 27].

Inspired by the SCMF method, Giuseppe Milano proposed the hybrid Particle-Field molecular dynamics method (hPF-MD) [28]. Instead of using MC moves, molecular dynamics is performed by integrating equations of motion, with forces computed from spatial derivatives of the external potential (particle-field forces). This procedure retains many of the computational advantages present in the SCMF method. From the dense polymer melts [29], that are prototypical applications of SCFT and SCMF, hPF-MD has found a wide range of applications, including non-lamellar and lamellar phases of lipids [30–32], vesicles [33] and percolation phenomena for carbon nanotubes in polymer melts [34], all paving a way towards closing the gap between all-atom and mesoscopic dimensionalities for biomolecular systems [2, 16, 35].

1.2 Scope, challenges and objectives

The scope of this thesis has been to develop new hPF-MD methods and models that can be used in the study of macromolecular biological systems. In particular, the thesis aims to extend the capability of hPF-MD to represent:

- Polypeptides
- Electrostatics
- Multiphase electrolytic systems
- Constant-pressure simulations

CG modelling of polypeptides is generally considered a challenging task. Contrary to simpler organic polymers, proteins exhibit complex local *secondary* structures, for example α-helices and β-sheets, that assemble in more complex

tertiary folded structures. These motifs, that can involve only a few amino acids, as well as tens to hundreds, are crucial not only as structural scaffold, but can be directly involved in the protein function. As the folding of secondary structure elements depends on the balance of both local and nonlocal interactions, their stability is very difficult to capture when coarse-graining, as important information can easily be lost. Given these challenges, the main research objective for the work on polypeptides is to provide:

- A proof of principle hPF-MD model that can represent conformational dynamics of polypeptides.

The polyelectrolyte nature of many biological molecules, such as proteins and DNA, plays a crucial role in determining their function. Therefore, the modeling of a large number of biological molecules requires an adequate description of electrostatics. The efficiency of the hPF-MD approach requires not using pair interactions, hence specialized methodology ans software is required. With this in mind, one of the main research objectives is to develop:

- Efficient hPF-MD software for computing electrostatic interactions.

Achieving accurate modeling of electrostatics in CG models is particularly challenging, as the molecular organization on a detailed level, which gives rise to dielectrics and screening of electrostatic interactions, is lost in the coarse-grained representation. This is especially detrimental for multiphase systems, where the value of relative dielectric, can vary by almost two orders of magnitude. Therefore a particular focus of this thesis is to develop:

- Accurate modeling of electrostatics in multiphase systems.

The utility of methodology and software development depend on applications. The hPF-MD method is particularly well suited to study multiphase phenomena, such as aggregation and phase-separation. With electrostatics in hPF-MD, we can model multiphase systems involving polyelectrolytes. Therefore, a key research objective is to develop:

- New models for polyelectrolytes that can assist in understanding multiphase-phenomena.

hPF-MD has yet to incorporate constant-pressure simulations. This is problematic for many biological systems, and in particular lipid membranes. The properties of lipid membranes are typically defined at a given surface tension, and this can only be obtained with constant-pressure simulations. With these considerations in mind, it is crucial for the applicability of hPF-MD to develop:

- Methodology for constant-pressure simulations with hPF-MD.

1.3 Structure of the thesis

The thesis is composed of four chapters. Chapter 1 aims at providing a context, as well as a motivation, for the work presented in this thesis. Chapter 2 introduces hPF-MD methodology in detail. Chapter 3 presents the papers which have resulted from the work of this thesis. Finally, chapter 4 sets out the main conclusion and outlook of this thesis.

Chapter 2

Methods

In this chapter we introduce the methods used throughout the thesis. While *molecular dynamics* is a central part of this thesis, the novelty of the work lies mostly in the use of density-field formalism to model intermolecular interactions among molecules. Hence the focus is put on the hybrid particle-field (hPF) part. For a thorough introduction into the foundations of molecular dynamics, the interested reader is referred to the excellent books by Dennis C. Rapaport [36] and by Daan Frenkel and Berend Smit [37].

2.1 Hybrid particle-field molecular dynamics

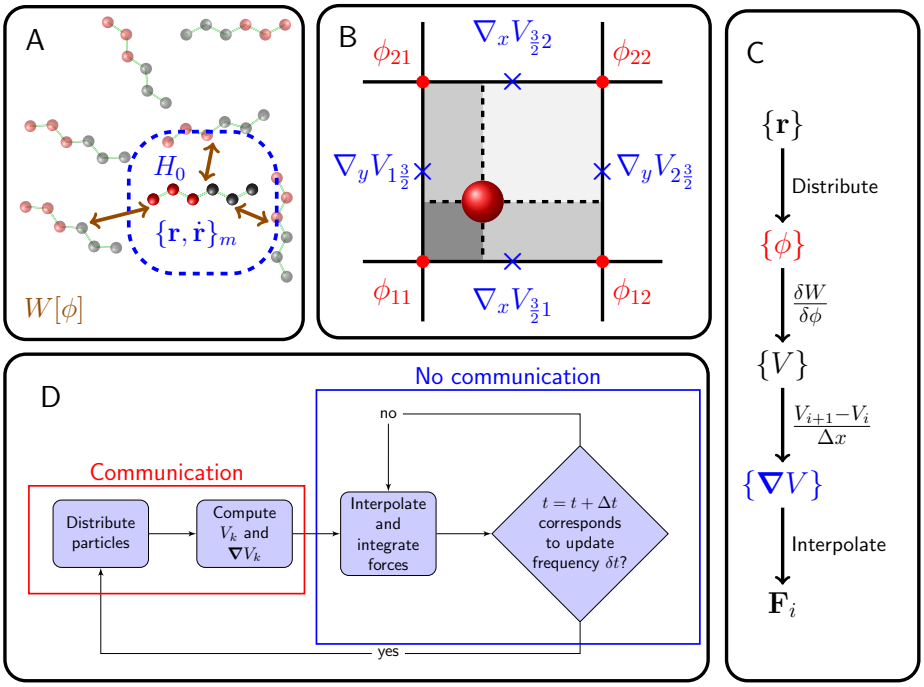

Figure 2.1: Illustration of the hybrid particle-field molecular dynamics. (A) A Polymer melt in which the polymer is subject to single-molecule Hamiltonian H_0 and is coupled to its environment through $W[\phi]$. (B) Particle-mesh routine for obtaining forces. (C) Relationship between the different variables needed for computing forces on particles. (D) Flow-chart for the molecular dynamics.

The essence of the hPF-method (see Figure 2.1) is contained in the separation

of the total energy of a molecular system into two terms:

$$H = \sum_{m=1}^{N_m} H_0(\{\mathbf{r}, \dot{\mathbf{r}}\}_m) + W([\{\phi\}]). \tag{2.1}$$

The first term is the sum over all N_m molecules of the *single-molecule Hamiltonian* $H_0(\{\mathbf{r}, \dot{\mathbf{r}}\}_m)$, which has an explicit dependence on particle positions $\{\mathbf{r}\}_m$ and velocities $\{\dot{\mathbf{r}}\}_m$. This includes the kinetic energy and the intramolecular energy. Intermolecular interactions are modeled through the second term, an *interaction energy functional* $W([\{\phi\}])$. The interaction energy functional is dependent on particle positions *only* through their set of local number densities $\{\phi\} = \{\phi_1 \dots \phi_k \dots \phi_M\}$ of the M particle species. The net effect of the interaction energy is a particle-specific external potential, which is given by (to be explained in 2.1.2):

$$V_k(\mathbf{r}) = \frac{\delta W[\{\phi\}]}{\delta \phi_k(\mathbf{r})}, \tag{2.2}$$

and a corresponding force-contribution on particle i of type k:

$$\mathbf{F}_i = -\boldsymbol{\nabla} V_k(\mathbf{r}_i). \tag{2.3}$$

Statistical properties for molecular systems with total energy expressed as (2.1), can be estimated by applying sampling methods. The single chain in mean field method (SCMF) [21] samples with *Monte Carlo* (MC), while hPF-MD method samples with *molecular dynamics* (MD).

Remarks on MD, MC and dynamics In general, MD has the advantage over MC, that it in addition to providing sampling, also can represent dynamics. However, with hPF-MD care should be taken before concluding on dynamics. One particular limitation lies within its limited ability to model sterics. Contrary to ordinary MD with pair interactions (particle-particle), where the intermolecular interactions keep particles from overlapping, sterics can only be modeled in a limited sense[1], and particles in hPF-MD can overlap. This implies that effects on dynamics, by for instance entanglement[2] or crowding, are not captured. In some sense this is problematic, because such effects are highly important for functionality. However, given the already ambitious goal of hPF-methods achieving good statistics on large macromolecular systems, dynamics should be addressed in future work. In some respects, the inaccurate modeling of steric effects is useful, as sterics can slow down the dynamics and thereby sampling. In fact, one of the keys to the success of SCMF is that molecules are more easily moved by MC (less rejection) than in particle-particle based methods [39].

[1] Due to the compressibility term, radial distribution functions obtained with hPF-MD simulations generally show a low probability at overlap-distances [31].

[2] We note that one can add on top of hPF specific models for entanglement, such as in ref. [38].

2.1.1 Molecular dynamics

In MD, sampling is done by integration of Newton's equations for the particles:

$$m_i \frac{\mathrm{d}^2 \mathbf{r}_i}{\mathrm{d}t^2} = \mathbf{F}_i, \tag{2.4}$$

where $\mathbf{F}_i$ is the total force acting on the particle i, and m_i is its mass. The integration of (2.4) is done by discretization of time into time steps. Using specialized integrators[3], such as *velocity Verlet*:

$$\mathbf{r}_i(t + \Delta t) = \mathbf{r}_i(t) + \dot{\mathbf{r}}_i(t)\Delta t + \frac{1}{2m_i}\mathbf{F}_i(t)\Delta t^2, \tag{2.5a}$$

$$\dot{\mathbf{r}}_i(t + \Delta t) = \dot{\mathbf{r}}_i(t) + \frac{1}{2m_i}\left(\mathbf{F}_i(t) + \mathbf{F}_i(t + \Delta t)\right)\Delta t, \tag{2.5b}$$

the dynamics of the particles is propagated. Assuming the *ergodic theorem*, estimates of averages of observables $\mathcal{O}$ are computed by time averaging:

$$\langle \mathcal{O} \rangle = \frac{1}{t}\int_0^t \mathrm{d}t' \ \mathcal{O}(t'), \tag{2.6}$$

when the simulation time $t \to \infty$.

2.1.2 Derivation of hPF-MD and relationship with self-consistent field theory

Equation (2.2) shows the relationship between the interaction energy and the external potential which acts on the particles. This formula, which is at the basis of hPF-MD, was first derived by following the same procedure as in self-consistent field theory (SCFT) [24, 40]. Starting from the Hamiltonian [40, p. 127]:

$$\hat{H}(\mathbf{\Gamma}) = \hat{H}_0(\mathbf{\Gamma}) + \hat{W}(\mathbf{\Gamma}), \tag{2.7}$$

where $\mathbf{\Gamma}$ specifies the microstate of the system, $\hat{H}_0$ is the energy of a noninteracting molecule, and $\hat{W}$ is the interaction energy. In the canonical ensemble, we have:

$$Z = \int \mathrm{d}\mathbf{\Gamma} \ \exp\left[-\beta\left(\hat{H}_0(\mathbf{\Gamma}) + \hat{W}(\mathbf{\Gamma})\right)\right], \tag{2.8}$$

where the integral over $\mathbf{\Gamma}$ is the the integral over the whole phase space:

$$\mathrm{d}\mathbf{\Gamma} = \prod_i^N \mathrm{d}\mathbf{r}_i \mathrm{d}\mathbf{p}_i. \tag{2.9}$$

We then assume

$$\hat{W}(\mathbf{\Gamma}) = \hat{W}(\hat{\phi}), \tag{2.10}$$

[3]Integrators for MD are designed to conserve the symplectic structure of the Hamiltonian dynamics. Most importantly, this entails conservation of the total energy.

where $\hat{\phi}$ are particle densities:

$$\hat{\phi}(\mathbf{r}, \mathbf{\Gamma}) = \sum_{i}^{N} \delta(\mathbf{r} - \mathbf{r}_i). \tag{2.11}$$

Using the δ function property:

$$\int [\mathrm{D}g(\mathbf{r})]\ \delta(f(\mathbf{r}) - g(\mathbf{r}))F[g(\mathbf{r})] = F[f(\mathbf{r})], \tag{2.12}$$

we can write (2.8) as:

$$Z = \int [\mathrm{D}\varphi(\mathbf{r})]\ \int \mathrm{d}\mathbf{\Gamma}\ \delta[\varphi(\mathbf{r}) - \hat{\phi}(\mathbf{r}, \mathbf{\Gamma})] \exp\left[-\beta\left(\hat{H}_0(\mathbf{\Gamma}) + \hat{W}(\varphi(\mathbf{r}))\right)\right]. \tag{2.13}$$

The δ function can be rewritten by Fourier transformation as follows:

$$\delta[\varphi(\mathbf{r}) - \hat{\phi}(\mathbf{r}, \mathbf{\Gamma})] = \int [\mathrm{D}w(\mathbf{r})]\ \exp\left[i \int \mathrm{d}\mathbf{r}\ w(\mathbf{r})\left(\varphi(\mathbf{r}) - \hat{\phi}(\mathbf{r}, \mathbf{\Gamma})\right)\right]. \tag{2.14}$$

Inserting (2.14) into (2.13), we get:

$$Z = \int \mathrm{d}\mathbf{\Gamma}\ \int [\mathrm{D}\varphi(\mathbf{r})]\ \int [\mathrm{D}w(\mathbf{r})]\ \exp\left[i \int \mathrm{d}\mathbf{r}\ w(\mathbf{r})\left(\varphi(\mathbf{r}) - \hat{\phi}(\mathbf{r}, \mathbf{\Gamma})\right)\right] \exp\left[-\beta\left(\hat{H}_0(\mathbf{\Gamma}) + \hat{W}(\varphi(\mathbf{r}))\right)\right] \tag{2.15}$$

We define

$$V(\mathbf{r}) \equiv i/\beta w(\mathbf{r}), \tag{2.16}$$

and the partition function of the molecules subject to $V(\mathbf{r})$ as:

$$z(V(\mathbf{r})) \equiv \int \mathrm{d}\mathbf{\Gamma}\ \exp\left[-\beta\left(\hat{H}_0(\mathbf{\Gamma}) + \int \mathrm{d}\mathbf{r}\ \hat{\phi}(\mathbf{r}, \mathbf{\Gamma})V(\mathbf{r})\right)\right]. \tag{2.17}$$

With definition (2.17) we get:

$$Z = \int [\mathrm{D}\varphi(\mathbf{r})]\ \int [\mathrm{D}w(\mathbf{r})] \exp\left[-\beta\left(-\frac{1}{\beta}\ln z + W(\varphi(\mathbf{r})) - \int \mathrm{d}\mathbf{r}\ V(\mathbf{r})\varphi(\mathbf{r})\right)\right] \tag{2.18}$$

or

$$Z = \int [\mathrm{D}\varphi(\mathbf{r})]\ \int [\mathrm{D}V(\mathbf{r})] \exp\left[-\beta\mathcal{F}([\varphi(\mathbf{r}), V(\mathbf{r})])\right], \tag{2.19a}$$

$$\mathcal{F}([\varphi(\mathbf{r}), V(\mathbf{r})]) \equiv -\frac{1}{\beta}\ln z + W(\varphi(\mathbf{r})) - \int \mathrm{d}\mathbf{r}\ V(\mathbf{r})\varphi(\mathbf{r}). \tag{2.19b}$$

The partition function can be sampled by *Field theoretic methods*, such as the ones being developed in the Fredrickson group [41]. In the self-consistent field theory, the sum over the canonical ensemble is approximated by a Gaussian integral around the most probable state that minimizes the argument of the exponential function, also referred to as the method of steepest descent. The condition determining the most probable state is given by:

$$\frac{\delta \mathcal{F}}{\delta \varphi(\mathbf{r})} = 0, \quad \frac{\delta \mathcal{F}}{\delta V(\mathbf{r})} = 0, \tag{2.20a}$$

which gives

$$V(\mathbf{r}) = \frac{\delta W[\phi]}{\delta \phi(\mathbf{r})}, \text{ and } \quad \varphi(\mathbf{r}) = -\frac{1}{\beta}\frac{\delta z}{\delta V(\mathbf{r})} = \left\langle \hat{\phi}(\mathbf{r}, \mathbf{\Gamma}) \right\rangle = \phi(\mathbf{r}). \tag{2.21}$$

Although the derivation above was done with a single component, it is easily generalized to multicomponent systems:

$$V_k(\mathbf{r}) = \frac{\delta W[\phi]}{\delta \phi_k(\mathbf{r})}, \text{ and } \quad \phi_k(\mathbf{r}) = -\frac{1}{\beta}\frac{\delta z}{\delta V_k(\mathbf{r})}, \tag{2.22}$$

where k denotes the species.

The procedure for solving SCFT is illustrated in Figure 2.2. By using densities $\phi_k(\mathbf{r})$, the external potential $V_k(\mathbf{r})$ is computed. From the external potential, the partition function for independent chains z is computed. From z, a new set of averaged out densities ϕ_k is computed, and the procedure is repeated until self-consistency is reached, corresponding to the minimal free energy of the system at field configuration $\{\phi_k^*, V_k^*\}$ [23, p. 204].

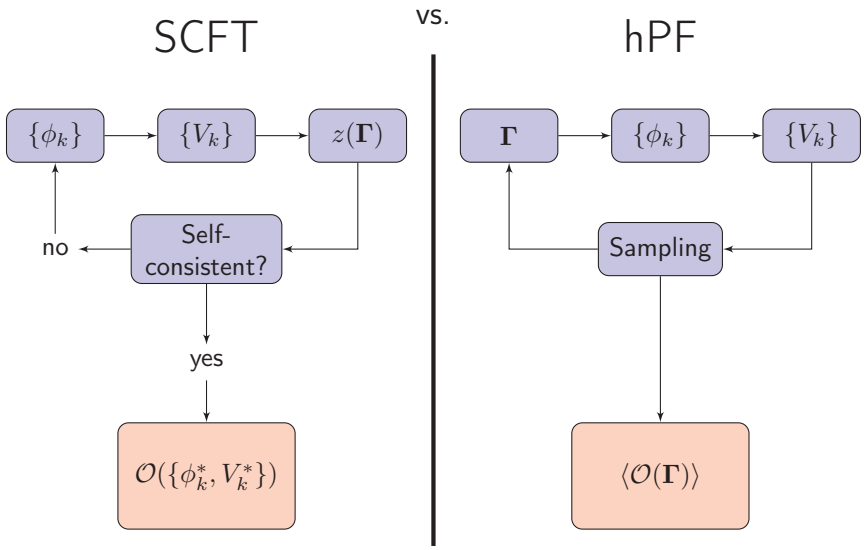

Figure 2.2: SCFT-procedure compared against hPF.

While hPF and SCMF are similar to SCFT, they are not equivalent. The use of the saddle-point approximation in SCFT amounts to considering *mean-field interactions*, because the density-fields are averaged over the single molecule partition function z. Therefore, one obtains only contributions from a single field-configuration $\{\phi_k^*, V_k^*\}$ when computing observables $\mathcal{O}(\{\phi_k^*, V_k^*\})$ [23, pp 204]. Instead, hPF-MD and SCMF consider the *instantaneous external potential* from a single molecular configuration $\mathbf{\Gamma}$, and by sampling different molecular configurations, we obtain averages of $\mathcal{O}(\mathbf{\Gamma})$. Consequently, fluctuations that are not present in SCFT, can be described by SCMF and hPF-MD [21].

An alternative manner of viewing hPF-MD is by considering the force directly from [38]:

$$\mathbf{F}_i = -\frac{\partial W}{\partial \mathbf{r}_i}, \tag{2.23}$$

which gives:

$$\mathbf{F}_i = -\int \mathrm{d}\mathbf{r}\ \frac{\delta W}{\delta \phi_k(\mathbf{r})} \frac{\partial \phi_k(\mathbf{r})}{\partial \mathbf{r}_i}, \tag{2.24}$$

or

$$\mathbf{F}_i = -\int \mathrm{d}\mathbf{r}\ V_k(\mathbf{r}) \frac{\partial \phi_k(\mathbf{r})}{\partial \mathbf{r}_i}, \tag{2.25}$$

Here the force is related to an integral over the same external potential found in our derivation by SCFT. There are multiple ways of computing this integral (such as in [38]); in the hPF-MD procedure proposed in [28], it is estimated by:

$$\mathbf{F}_i \simeq -\boldsymbol{\nabla} V_k(\mathbf{r}_i), \tag{2.26}$$

i.e. the derivative of the external potential at the position of the particle. In practice this is done by interpolation of derivatives of the external potential onto the particles (see 2.3.1).

2.2 Interaction energies

The most important interaction-energies employed in hPF-MD are in the form of:

$$W[\{\phi(\mathbf{r})\}] = \int \mathrm{d}\mathbf{r}\ w(\{\phi(\mathbf{r})\}), \tag{2.27}$$

where $w(\{\phi(\mathbf{r})\})$ is the *local interaction energy density*. Interaction energies of this particular form give rise to external potentials:

$$V_k(\mathbf{r}) = \frac{\partial w(\{\phi(\mathbf{r})\})}{\partial \phi_k(\mathbf{r})}. \tag{2.28}$$

2.2.1 Partitioning: The Flory-Huggins term

In analogy with Flory-Huggins lattice theory, and assuming each particle occupies a space of $v_0 = 1/\rho_0$, we describe interaction between densities with the

following interaction energy density [23, p. 151]:

$$w_{\tilde{\chi}}(\{\phi\}) = \frac{1}{2\rho_0} \sum_{k\ell} \tilde{\chi}_{k\ell} \phi_k(\mathbf{r}) \phi_l(\mathbf{r}), \tag{2.29}$$

where $\tilde{\chi}_{k\ell}$ is analogous to the Flory χ parameter[4]. However, unlike in ideal theory, where $\tilde{\chi}_{kl}$ is related to the potential of mean force or the partition coefficient between two species, here it is purely energetic and a phenomenological constant used to model contacts between particles. The corresponding external potential of $w_{\tilde{\chi}}$ is given by:

$$V_{\tilde{\chi},k}(\mathbf{r}) = \frac{1}{\rho_0} \sum_{\ell} \tilde{\chi}_{k\ell} \phi_l(\mathbf{r}). \tag{2.30}$$

2.2.2 Homogeneity: The excluded volume term

To control local fluctuations and avoid nonphysical accumulation of particles, a local energy density which is dependent on the sum of particle densities is often used [40, p. 164]:

$$w_{\kappa}(\phi) = \frac{1}{2\rho_0 \kappa} \left(\sum_{\ell} \phi_\ell - \rho_0 \right)^2, \tag{2.31}$$

where κ is referred to as a compressibility parameter. The external potential of (2.31) felt by a particle of species k, is given by:

$$V_{\kappa,k} = \frac{1}{\rho_0 \kappa} \left(\sum_{\ell} \phi_\ell - \rho_0 \right), \tag{2.32}$$

Note that the second term is only a constant, and therefore it does not contribute to forces. Consequently, we can relate the two terms to the $V_{\tilde{\chi}}(\mathbf{r})$ through the following relation:

$$\tilde{\chi}_{k\ell} = \frac{1}{\kappa}, \tag{2.33}$$

where the κ term is effectively an added constant to the whole $\tilde{\chi}_{kl}$ matrix.

2.3 Computational procedures for hPF-MD

Having introduced the hPF-MD formalism, we now consider the computational procedures needed to perform hPF-MD. All the procedures that are presented here have been implemented in the hPF-MD code OCCAM, which was used for obtaining the results of thesis. As is emphasized later in 2.3.4, these procedures are not unique, but they are designed to exploit the efficiencies which the hPF-MD formalism allow for.

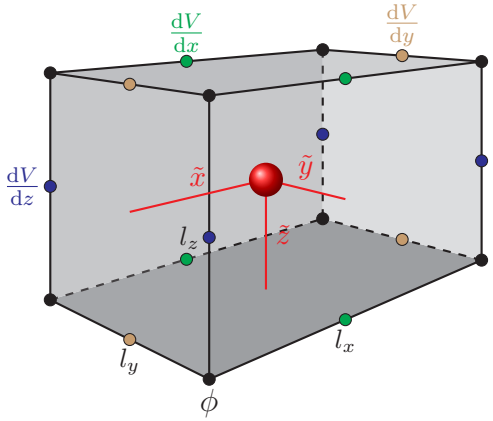

Figure 2.3: Distribution of a particle with CIC-procedure. Grid of density is indicated by black balls, while the staggered grid of the derivatives of the external potential is indicated by coloured balls.

2.3.1 Computation of densities and forces

In hPF-MD the forces due to the density-dependent interaction potential are computed through a particle-mesh approach [42]. First, the simulation box of $L_x \times L_y \times L_z$ is divided into $m_x \times m_y \times m_z$ cells (regular grid) of size $l_x = L_x/m_x, l_x = L_x/m_y, l_y = L_z/m_z$. The N particles are then distributed onto M grids for each of the M types of particles. In particle-mesh methods, the most commonly used ways of distributing particles are the nearest-grid-point (NGP) and cloud-in-cell (CIC), which differ by considering nearest grid point and grid points of the cell, respectively. In the current version of OCCAM, the CIC method, as illustrated in Figure 2.3, is used:

$$W(\tilde{x},\tilde{y},\tilde{z}) = w(\tilde{x})w(\tilde{y})w(\tilde{z}), \quad w(\tilde{x}) = 1-\tilde{x}, \quad \tilde{x} \equiv x/l_x - \text{floor}\ (x/l_x), \quad (2.34)$$

where $W(\tilde{x},\tilde{y},\tilde{z})$ is the weight prescribed to neighboring vertices. The discretized densities are then obtained by summing the contributions of all the particles onto discretized densities $\phi_k^{i_x i_y i_z}$. Using $\phi_k^{i_x i_y i_z}$, the corresponding external potential $V_k^{i_x i_y i_z}$ is computed. The force on particle i requires the gradient of the external potential at position $\mathbf{r}_i$. These gradients are computed on a staggered grid with central finite-difference approximation at the mid-points of the edges (see Figure 2.3):

$$\left.\frac{dV_k}{dx}\right|_{i_x+1/2,i_y,i_z} = \frac{1}{l_x}\left(V_k^{i_x+1,i_y,i_z} - V_k^{i_x,i_y,i_z}\right) \quad (2.35)$$

[4]Throughout this thesis we use $\tilde{\chi}$ with unit energy, which in Flory-Huggins-theory would correspond to $\tilde{\chi} = k_b T \cdot \chi$.

Finally, forces can be computed directly from the staggered grid as follows [28, 43]:

$$F_{i,x} = -w(\tilde{x}_i + 1/2)\frac{\mathrm{d}V_k}{\mathrm{d}x}_{i_x+1/2,i_y,i_z} - w(1/2 - \tilde{x}_i))\frac{\mathrm{d}V_k}{\mathrm{d}x}_{i_x-1/2,i_y,i_z}, \quad (2.36a)$$

$$F_{i,y} = -w(\tilde{y}_i + 1/2)\frac{\mathrm{d}V_k}{\mathrm{d}y}_{i_x,i_y+1/2,i_z} - w(1/2 - \tilde{y}_i)\frac{\mathrm{d}V_k}{\mathrm{d}y}_{i_x,i_y-1/2,i_z}, \quad (2.36b)$$

$$F_{i,z} = -w(\tilde{z}_i + 1/2)\frac{\mathrm{d}V_k}{\mathrm{d}z}_{i_x,i_y,i_z+1/2} - w(1/2 - \tilde{z}_i)\frac{\mathrm{d}V_k}{\mathrm{d}z}_{i_x,i_y,i_z-1/2}. \quad (2.36c)$$

2.3.2 Quasi-instantaneous external potential

One of the most important rules for numerical solution of partial differential equations is the *Courant–Friedrichs–Lewy condition* (CFL) [44]. It states that the time step used for propagating explicit time-integration schemes is limited by

$$\Delta t < C\Delta x, \quad (2.37)$$

where C is a number describing how fast the solution travels in space. Analogously for hPF-MD and SCMF, the densities are computed on a coarse grid, and their speed "C" is low. The *quasi-instantaneous* approximation exploits this fact by keeping the external potential constant over multiple time steps. Systematic benchmarks, and in particular the extensive phospholipid simulations in [29], show that the computed properties remain largely unaltered for hundreds of time steps, depending on the size of the grid. The quasi-instantaneous approximation significantly boots the efficiency of hPF-MD by reducing the amount of computation per time step. Moreover, it allows for a more efficient parallelization.

2.3.3 Parallelization

The main advantage of the hPF-MD compared to ordinary MD methods lies within the computational efficiencies that the particle-field formalism allows for. This is best understood when contrasted by MD. In ordinary MD, the most expensive routines are generally the computation of intermolecular interactions. The main computational cost lies in the computation pair interactions which are of order N^2. Years of development has resulted in methods that overcome this scaling, such as Verlet lists [37, p. 545], truncation schemes [37, p. 98] and Ewald summation-schemes [45], reducing it to $\mathcal{O}(N\log(N))$. State of the art MD-Packages, such as NAMD [46] and GROMACS [20], use *domain decomposition* as a parallelization strategy. In domain decomposition, the simulation box is divided into spatial domains, and molecules are assigned to processors according to which domain they reside. This not only reduces the memory usage but also communication among processors, as long-range interactions are computed by only considering the neighboring domains. Nonetheless, computing pair-interactions still remains the most expensive part of the simulation.

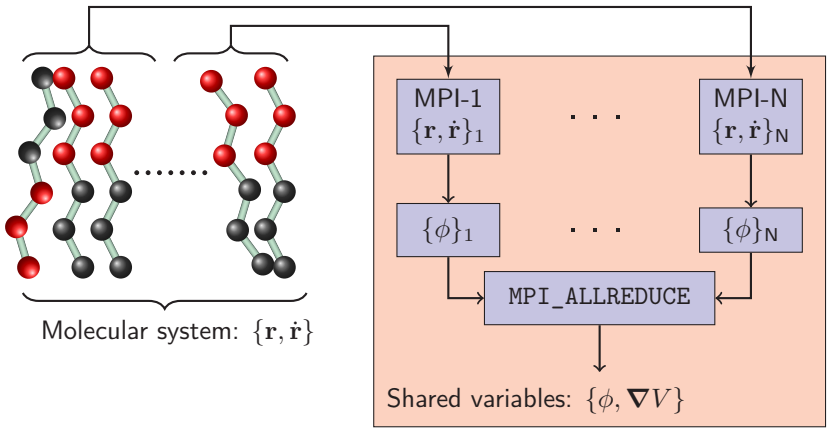

Figure 2.4: Parallelization strategy for hPF-MD. Molecules are assigned to MPI-tasks at the start of the simulation. Each MPI-task n contains only information $\{\mathbf{r}, \dot{\mathbf{r}}\}_n$ on its molecules throughout the whole simulation. The global density-field is obtained by computing density-contributions from each MPI-Task $\{\phi\}_n$, which are then combined by a single `MPI_ALLREDUCE` command. From the shared densities, the external potential and its derivative are computed on each MPI-task and are identical for all MPI-tasks.

In hPF-MD, since H_0 only involves intramolecular interactions and intermolecular interactions are computed by a particle-mesh approach, molecules naturally decouples, significantly reducing the amount of needed communication. In fact, domain decomposition is not necessary, and a simpler strategy where each MPI-task has a copy of global variables, such as the density grid, can be adopted. With this strategy, molecules are divided and assigned to MPI-tasks at the start of the simulation (Figure 2.4). Each MPI-task only contains information on its molecules (the positions and velocities of the particles). On each MPI-task, densities are computed, and by a single `MPI_allreduce` command, the densities from all the MPI-tasks are combined. This is the only major event requiring communication among all of the processors in use.

The algorithm for propagating hPF-MD and the effect of the parallelization strategy are illustrated in Figure 2.5. The algorithm is separated into two parts: one requiring communication and the second not requiring communication. This separation captures the essential features determining the overall computational efficiency. The cost of the communication part is controlled by the quasi-instantaneous update frequency $\delta t \equiv m\Delta t$ and is reduced as $1/m$, where commonly $m \sim 100$. The second part, by requiring no communication, is *trivially parallelizable*, and its contribution to computation-time is reduced as $1/N$, where N is number of MPI-tasks. This algorithm formally[5] exhibits

[5]One of the limitations of domain decomposition based codes is that the smaller the system, the fewer CPUs can be used before performance levels off. This is caused by the domains becoming too small, and resulting in increased communication.

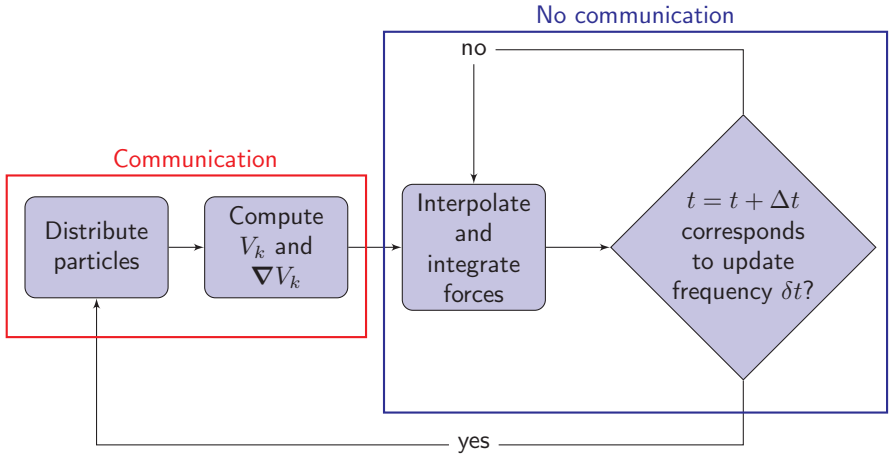

Figure 2.5: Algorithm for time propagation of hPF-MD and which parts that require communication.

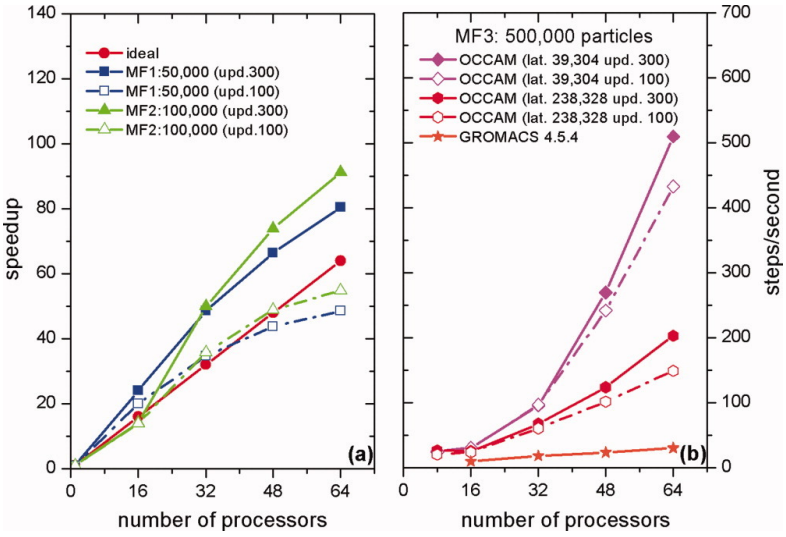

Figure 2.6: Benchmark of hPF-MD (particle-field) against GROMACS (Lennard-Jones) for monoatomic fluid systems. Left) Speedup of OCCAM with the number of processors for 50 000 particles (MF1) and 100 000 particles (MF2) and update frequency 100 and 300. Right) Performances of OCCAM program as steps/s for a system of 500 000 particles (MF3) in comparison to a Lennard-Jones fluid simulation with GROMACS 4.5.4. Results of OCCAM were obtained by using 39 304 and 238 328 lattice points with update frequency of 100 and 300. Figure is reprinted from ref. [47].

strong scaling: linear scaling for large and small systems [27]. However, for many MPI-tasks and large systems involving large grids, combining densities can become computationally expensive. Secondly, operations on the grid, such as finding the derivative of the external potential, are also computationally costly as these operations are only performed by a single MPI-task. For small systems, such operations are cheap, while for larger systems such computation can lead to a flatting out of performance. A benchmark plot of hPF-MD implemented into OCCAM [47] is presented in Figure 2.6. We recognize several of the main features which is formally exhibited by hPF-MD: close to linear scaling, and increased efficiency with lower update frequency and fewer grid points.

2.3.4 The OCCAM code

All the methods presented in this thesis were implemented into the OCCAM code[6]. The OCCAM code is a specialized molecular dynamics software for running hPF-MD. The first serial version was developed by Milano and Kawakatsu in 2009 [28] and included all the basic ingredients needed for MD and force calculation. The code was eventually extended to MPI parallelization, where molecules are divided among processors [47]. As a result of the work in this thesis, the code has been extended to include electrostatics and constant-pressure simulations. Additionally, there is an unofficial version of OCCAM including multiple-particle collisions [43].

Similar approaches and codes While we have stressed the connection between hPF-MD with SCMF, there are additional related methods and codes. GALAMOST [48], a GPU-based MD package aimed at coarse-grained simulations, has an implementation of hPF-MD with the interaction energies described in 2.2 and electrostatics [49]. Recently, Doros Theodorou [38] has developed a hPF-BD/kMC method where particles are propagated by Brownian dynamics or kinetic Monte Carlo.

[6] `http://www.occammd.org/`

Chapter 3

Introduction to the papers

This thesis contains six papers, three of which have been published in peer-reviewed journals, two have been accepted after peer-review and one is a manuscript that has been submitted for peer-review. The papers are introduced in thematic order.

3.1 Polypeptides

Paper I: *Hybrid Particle-Field Model for Conformational Dynamics of Peptide Chains*
Sigbjørn Løland Bore, Giuseppe Milano and Michele Cascella
Journal of Chemical Theory and Computation **14**, 1120–1130 (2018)

Summary

Conformational dynamics of proteins is very important in biology and medicine (protein folding, protein regulation, peptide-mediated signaling, antimicrobial peptide action, etc.), but it is also very difficult to represent by all-atom simulations. Speeding up peptide studies by reliable CG models is crucial. Paper I proposes the first ever hPF model for polypeptides. In accordance with the hPF formalism, an underlying model for the single-molecule Hamiltonian H_0 is required. The model for H_0 is based on a two-bead representation of each amino acid, with one bead being placed at the Cα-position and another placed at the center of mass of the sidechain. It is known that directional interactions are necessary to stabilize protein secondary structures [50]. To introduce this into our model we employ the dipole reconstruction method, developed by Cascella and coworkers [51], for the dipole moment of the peptide bond. Due to the rigidity of the peptide bonds, the fundamental degrees of freedom determining the conformation of the polypeptide, are the bending and torsional angles of the Cαs. It has been shown by Tozzini et al. [50] that these angles exhibit strong correlations. To take this into account, we employ a combined torsional-bending potential. On top of this, we introduce a propensity potential which models the specific amino-acid propensity towards certain conformations. The intermolecular interactions are modeled by the interaction energy with mixing and compressibility terms as described in Section 2.2. In particular, we adopt a hydrophobic-polar (HP) model, in which side chains are categorized as either hydrophobic or polar by their $\tilde{\chi}$ parameter with water. The model was implemented into OCCAM.

Through a series of test cases, we demonstrated that the model is able to reproduce key elementary structural elements, such as α-helices and β-structures.

Furthermore, we explored the phase diagram of homo sequence polypeptide in terms of the propensity and $\tilde{\chi}$ parameters, and showed that the $\tilde{\chi}$ parameter is able to signal environmental effects on conformations. Using amphiphilic sequences, we showed that the $\tilde{\chi}$ parameter can facilitate super secondary structures, with tertiary and quaternary structures requiring the $\tilde{\chi}$ interactions. Finally, when combining the polypeptide model with the model for dioleoylphosphatidylcholine (DOPC) [31], we found that by only having $\tilde{\chi}$ interactions between the polypeptide and the membrane, the multiphase environment stabilizes secondary structures that are unstable in a homogeneous environment.

Statement of significance

In the past, the hPF formalism has predominantly been applied on simpler molecules. Therefore, its application onto polypeptides constitute a major widening of the scope of hPF modeling towards complex biological molecules. At the present stage, the model is a toy model and should not be used to model specific sequences. However, with careful parameterization of propensity and the $\tilde{\chi}$ matrix, chemically specific models can be made. Lastly, by having this model within the hPF approach opens up for studying large assemblies of polypeptides and combining them with other hPF models.

Contributions

Paper I The model was primarily developed by Michele Cascella and me, and I implemented it into OCCAM. The paper was written by Michele Cascella and me with corrections and suggestions from Giuseppe Milano.

3.2 Electrostatics

Paper II: *Hybrid Particle-Field Molecular Dynamics Simulations of Charged Amphiphiles in Aqueous Environment*
Hima Bindu Kolli, Antonio De Nicola, **Sigbjørn Løland Bore**, Ken Schäfer, Gregor Diezemann, Jürgen Gauss, Toshihiro Kawakatsu, Zhongyuan Lu, You-Liang Zhu, Giuseppe Milano and Michele Cascella
Journal of Chemical Theory and Computation **14**, 4928–4937 (2018)

Paper III: *Mesoscale Electrostatics Driving Particle Dynamics in Nonhomogeneous Dielectrics*
Sigbjørn Løland Bore, Hima Bindu Kolli, Toshihiro Kawakatsu, Giuseppe Milano and Michele Cascella
Journal of Chemical Theory and Computation **15**, 2033 (2019)

Summary

The polyelectrolytic nature of biological molecules, such as polypeptides, DNA, charged surfactants, and lipids, is an important factor determining key properties, including phase behavior, structure and function. Since the use of pair interactions slow down the hPF approach, specialized methods which model electrostatics with particle-field interactions are needed. Paper II and III concern two complementary models for electrostatics within the hPF-approach.

Paper II is on an implementation and application of the hPF method for computing electrostatic interactions. The method was first developed by Zhu et al. [49] and is an adaptation of the Particle-Mesh-Ewald approach [52, 53], which replaces short-range pair interactions with short-range particle-density interactions. The combination of long and short-range interactions results in an external potential which acts on charged particles. A benchmark of the method and the implementation was carried out through applications on palmitoyloleoylphosphatidylglycerol (POPG) lipid membrane and sodium dodecyl sulfate (SDS) surfactants. We demonstrated that upon proper calibration of simulation parameters, in particular the relative dielectric constant, we achieve an excellent POPG lipid bilayer structure and concentration dependence of the SDS assembly into microtubular aggregates.

For multiphase systems, and in particular lipid bilayers, the effective relative dielectrics can change by almost two orders of magnitude. This has a profound effect on the screening of electrostatic interactions. Therefore, the use of a constant dielectrics constitutes a major approximation. Paper III expands on Paper II by considering a density dependent dielectrics and a electrostatic potential governed by the *generalized Poisson equation*. From the total electrostatic energy of the system and following the procedure as described in Section 2.1, the external potential is obtained. The external potential acting on particles contains, not only the Coulomb term, but also a polarization term acting on all particles. Through a series of applications, we verified the model's ability to correctly reproduce partition phenomena of ions in multiphase systems, benchmarking against the Born model for solvation of ideal ions. Lastly, applications on ion distribution around lipid bilayers show that the use of density-dependent dielectrics correctly predicts low penetrability of ions into the POPG lipid bilayer.

Statement of significance

The extension of software and methodology to polyelectrolytes significantly expands the applicability of the hPF approach. This is evidenced by the applications presented in Paper V on lipid A and in study in Paper VI on SDS, which before this work was beyond the scope for the OCCAM code. While the density-dependent dielectric method of Paper III was derived within the hPF formalism, it is applicable to all coarse-grained models employing explicit solvation. In particular, it could be used with MARTINI [17] on the standard nonpolarizable water model.

Contributions

Paper II My main contribution to the work presented in Paper II was to test the code by computing the forces between two charged point particles against analytic forces. I discovered a major bug in the original implementation which was related to the ordering of wavenumbers in the FFTW library [54] (fast Fourier transform). Finally, I produced the data for the benchmark of forces and assisted in writing the manuscript.

Paper III The method was derived by me and Michele Cascella. I implemented the method, on top of code developed by Hima Bindu Kolli, in addition to conducting the simulations. The manuscript was written by me and Michele Cascella with corrections from the co-authors.

3.3 Multiphase electrolytic systems

Paper IV: *Aggregation of Lipid A Variants: a Hybrid Particle-Field Model*
Antonio De Nicola, Thereza A. Soares, Denys E. S. Santos, **Sigbjørn Løland Bore**, G. J. Agur Sevink, Michele Cascella and Giuseppe Milano
BBA – General Subjects, in press (2020)

Paper V: *Beyond the Molecular Packing Model: Understanding Morphological Transitions of Charged Surfactant Micelles*
Ken Schäfer, Hima Bindu Kolli, Mikkel Killingmoe Christensen, **Sigbjørn Løland Bore**, Gregor Diezemann, Jürgen Gauss, Giuseppe Milano, Reidar Lund and Michele Cascella
Submitted for peer-review (2020)

Summary

Despite the growing sophistication and availability of experimental methods for probing multiphase soft matter and biological systems, primarily scattering experiments, it is at present, beyond regular or simple shapes, difficult to interpret what the assembled structure is like on a molecular level. From the standpoint of a theoretical chemist, multiphase electrolytic systems are particularly challenging. First, their multiphase nature is caused by *collective interactions*, and therefore an understanding cannot be ascertained by only considering the constituents in isolation. Second, the phase behavior is dictated by the long-range electrostatics, and therefore nonlocal effects and salt dependency must be accounted for. The mesoscale length and time scales prohibit the study by high resolution computational methods, such as quantum mechanical and even all-atom approaches, but are however perfectly suited for CG modeling.

Paper IV develops a hPF model for Lipid A. This lipid is particularly relevant in biology, as it is one of three components of bacterial lipopolysaccharides which comprise the outer membrane of Gram-negative bacteria. It is a complex lipid

with four tails and two negatively charged heads. We use the electrostatics code developed in Paper II and parameterize the model to be consistent with the all-atom lipid A model developed by Thereza A. Soares [55]. As parameterization procedure, we compared density profiles of all-atom simulations of solvated lipid A bilayer and tuned model parameters, mainly the relative dielectric and the $\tilde{\chi}$ matrix, to reproduce the density profiles. Upon calibration, we found that our model reproduces the structural properties of all-atom simulations and that it gives a description of phase behavior which is consistent with experiments.

Paper V continues the work of Paper II by considering in detail the phase diagram of SDS in terms of concentration of SDS and salt. In particular, we use SDS as a model system to study the validity of the packing model in systems with long range electrostatic interactions. The phase diagram is explored by scattering experiments, SAXS and SANS, and simulations with hPF-MD using the code and model developed in Paper II. The simulations and experiments are in qualitative agreement, exhibiting the same phase diagram, but with transitions from spherical to tubular micelles at quantitatively different concentrations. We find by examining the molecular structures in the simulations that the transition is not signaled by a change in packing parameter, but rather a change in the distribution of counterions near the charged heads of the SDS. On this basis, we developed a simple electrostatics model for the coordination of ions close to the SDS heads. The model suggests that at high concentration of salt, counterions transition from localized to unlocalized binding between the heads of SDS. From this insight, we propose a mechanism for the transition where the fundamental packing piece changes from a single SDS (packing parameter of a cone) to two SDS (packing parameter of cake piece). With such a transition, the packing model adequately explains the transition.

Statement of significance

Lipid A is the prototypic example of a complex, slow-diffusing lipid, for which an accelerated method like hPF is particularly suited. Having developed and benchmarked our model, it is now ready to be further applied on larger systems and to explore the phase diagram in detail. One possibility is to couple this new model with a density-dependent dielectric. This will likely require a reparameterization of the $\tilde{\chi}$ matrix, but opens up for treating electrostatics more accurately.

Paper V further strengthens the validity of the SDS model, proposed in Paper II, in accurately representing the phase diagram of SDS. While this molecule has been studied for more than a century, the molecular mechanism dictating their morphology is unknown. This paper proposes a simple model for the transition for SDS and gives a general insight to how electrostatics can affect the morphological transitions of small charged copolymers.

Contributions

Paper IV My main contribution to Paper IV was in supervising the use of the electrostatics code, and incorporating and testing of the rotational invariant gradient used for the vesicle simulations. I also contributed to the writing of the paper, with particular focus on the methods part.

Paper V I supervised the use of electrostatics code in the simulations by Ken Schäfer, and contributed with corrections and suggestions to the manuscript.

3.4 Constant-pressure simulations

Paper VI: *Hybrid Particle-Field Molecular Dynamics Under Constant Pressure*
Sigbjørn Løland Bore, Hima Bindu Kolli, Antonio De Nicola, Maksym Byshkin, Toshihiro Kawakatsu, Giuseppe Milano and Michele Cascella
The Journal of Chemical Physics, in press (2020)

Summary

The investigation of multiphase systems often requires probing the system at constant pressure. For example, lipid membranes are typically studied under constant tension conditions and is only obtained with a barostat. So far, hPF simulations have been limited to constant-volume conditions. Paper VI presents the first ever constant-pressure simulations with hPF. This development was enabled by reformulating the interaction energy, by introducing an equation of state parameter and a square-gradient density term which models interfacial energy. We first considered the model for water (four water molecules per CG-bead) and parameterized the equation-of-state parameter, such that it reproduced the correct density of water at ambient conditions. Using this parameterization, we explored the behavior of binary fluids, demonstrating that $\tilde{\chi}$ interaction results in strong excess volume effects and that the square-gradient term controls the shape of a phase separated droplet. Moreover, we considered the already developed model for DPPC by de Nicola [31], and added a square-gradient interaction between carbon and water. We found that the square-gradient term is necessary to obtain the correct area per lipid for a DPPC lipid bilayer. Moreover, initial simulations of a small lipid vesicle indicate that it improves the agreement of all properties with what has been reported for the MARTINI model [56].

Statement of significance

Paper VI expands the applicability of hPF simulations. With this new formalism, one can equilibrate simulation boxes and study a range of phenomena requiring constant-pressure simulations. The incorporation of square-gradient

has a large potential for extending the capability of hPF-models to more accurately represent surface phenomena. Despite the very simplified parameterization with square-gradient interactions between only carbon and water, we obtained remarkable improvement on many properties of the lipid model. A full reparameterization is a promising route towards hPF models with chemical specificity and accurate modeling of surface phenomena. Finally, since the method was derived for hPF-methods in general, it is also applicable for the *single chain mean field* method.

Contributions

Paper VI The new formalism, derivations and its implementation, that allowed for constant-pressure simulations with hPF, were developed by me. The applications were conducted by me. The paper was written by Michele Cascella and myself, with corrections from the other coauthors.

Chapter 4

Conclusion and outlook

This thesis has considered hPF methods for biological systems. The primary research output of this work lies in its advancement of *computational methodology*, *modeling* and *software*. These advancements allow us to use the hPF method to study new biological systems with complex electrostatics and multiphase behavior, which prior this work were beyond the scope of existing methods and implementations. This is demonstrated by the new applications of hPF-MD on a wide range of new systems, including polypeptides, charged membranes, SDS and Lipid A.

However, since the hPF-MD method is quite new, there are still many avenues to explore. In addition to the new developments, much experience has been gained on the limitations of hPF-MD. From this I strongly believe that the following lines of research can extend the capabilities of the hPF-MD approach.

Systematic parameterization procedures One of the major challenges when developing new models within the hPF-MD approach, lies in choosing the $\tilde{\chi}$ matrix for the coarse-grained beads. In the models that have been developed thus far, two main approaches have been applied for obtaining $\tilde{\chi}$ matrix: from Flory-Huggins lattice theory using data (either experimental or simulation) or from optimization by hand to reproduce some statistics. It is difficult for a specific CG bead, such as a part of the protein, to estimate the value of $\tilde{\chi}$. Moreover, the value of $\tilde{\chi}$ depends on the modeling, for example whether there is electrostatic interactions or not. I have therefore started to explore systematic procedures for choosing $\tilde{\chi}$ in collaboration with PhD student Morten Ledum, who is continuing this work. The idea is to focus less on the theory and interpretation behind the simulation parameters and more on the output of these parameters in terms of statistical properties which determine the fitness of the CG model. In particular, we have started a project on developing global optimization routines, based on machine learning of the simulation parameters, focusing on $\tilde{\chi}$ with the test case of phospholipids. This is also a promising route for obtaining chemically specific parameterization of polypeptides, lipids and ions. Moreover, it will make it less difficult to incorporate new methods and develop new models in the future when using this approach.

New interaction energies In the hPF models discussed in this thesis, we have employed mixing and compressibility terms. These terms are on one hand very simple, but on the other hand limited in their capability to represent physical phenomena. In particular, the compressibility term promotes all particles to occupy the same volume, which can be detrimental for multiphase systems where particles do not necessarily occupy the same volume. One worthwhile route (for

NVT-simulations) is to use the equivalence between the κ and the $\tilde{\chi}$ in (2.33) to add diagonal terms to the $\tilde{\chi}$ matrix. Such an approach should be able to capture particles occupying different molar volumes. Another approach is to leave behind this simplified compressibility model and move towards a more complex functional dependency on densities for the interaction energies, such as in the hPF method of Theodorou [38]. These models are also likely to be more suitable to studying the response of a system under changing thermodynamic conditions.

Rigorous force computation The computation of the forces in hPF-MD is in my opinion a topic which should be examined in detail. It is known that the shape of large vesicles are affected by the grid. For example using the standard central finite differences produces for a large vesicle with a cubic shape oriented according to the grid [43]. This can be remedied by using finite-differences stencils with rotational invariance. Derivatives computed with the fast Fourier transform might produce even better results, but it is dependent on a smooth density to avoid producing spurious oscillations. Also important is the interpolation of densities and forces. There is an extensive literature on particle-mesh methods [42], which can serve as starting point for this. A benchmark of the force computation should determine what is needed to obtain forces on particles (due to W) which are translation invariant, rotational invariant and conserve the energy. Improving these aspects will likely result in an improved method with less numerical artifacts. Also, the quasi-instantaneous approximation should be revisited more in detail. Which artifacts does it produce? Can we make it more efficient by not interpolating forces onto particles every time step? A multiple time step algorithm separating bonded forces and particle-field forces is a promising route for increasing the computational efficiency of the hPF-MD.

Coupling differential equations to hPF The procedure that was used to derive the forces on the particles in density-dependent dielectric method of Paper III, is generalizable. It tells us how we, given an interaction energy and a corresponding partial differential equation, compute the forces on the particles composing the density. While solving partial differential equations with high frequency appears computationally expensive on the surface, there are several factors which reduces the computational cost. First, the density of the particles is not an unknown, thus the complexity of many partial differential equations is reduced. For example, we only had to consider the generalized Poisson equation and not the Poisson-Boltzmann equation in Paper III. Lastly, since most methods for solving partial differential equations are based on iterations on an initial trial solution, one can reuse the previous solution to reduce the amount of needed iterations. In particular, it would be very interesting to obtain correlation between the motion of particles through hydrodynamic interactions.

Improved software The parallelization in Zhao et al. [47] drastically increased the capability of OCCAM to simulate large systems. However, given the huge

increase of computational resources, it is now in need of modernization. The newly developed SCMF code by Schneider and Müller [27] tells us how this can be carried out. First and foremost, the current version of OCCAM uses an MPI-parallelization with one CPU per MPI-task. This is problematic for large systems, as some large operations are conducted on a single CPU. This can to a large degree be fixed by an hybrid MPI and openMP parallelization. In this strategy, each MPI-task uses many CPUs (typically a whole node) and are parallelized by openMP. This alone will improve the capability of OCCAM to simulate systems that are about 40 times larger (depending on the amount of CPUs per node). Another promising route is to develop a GPU-version. The low level communication in the hPF-MD approach will make such an implementation easier than for particle-particle approaches and indeed more efficient. Such a code will allow for very cheap investigation of large systems.

Closing remarks

Limiting ourselves to the hPF-MD, we now revisit the question posed at the beginning of this thesis: "Can we understand complex biological systems, such as bacterias, organelles and cells, by considering their constituents, the atoms?" First, whether hPF-MD simulations can provide an understanding on these systems is dependent on its capability of describing the chemistry dictating the behavior of these systems. The developments presented in this thesis, in particular on electrostatics, surface tension, and in models for polypeptides and Lipid A, provide us with many of the necessary ingredients needed to model, though simplified, such systems. However, whether these models provide an understanding is dependent on their quality, and, in particular, the polypeptide model will require further parameterization. Second, in terms of size these systems are on the micrometer scale, and involve of the order billions to trillions of atoms. By the level of coarse-graining that has been adopted in this thesis, the number of degrees of freedom is reduced by a factor of about 12. With the current version of OCCAM, we have simulated systems up 20 million beads or 200 million atoms. Therefore, these systems are currently too large. However, with the development of the software as outlined in the previous paragraph, we should be able to approach dimensions of relevance for organelles, viruses, and even parts of a cell. To conclude, we are not there yet, but the work of this thesis has led us closer, and many extremely interesting systems are within the horizon of hPF-MD.

Bibliography

[1] P. A. M. Dirac, *Quantum mechanics of many-electron systems*, Proceedings of the Royal Society of London. Series A, Containing Papers of a Mathematical and Physical Character **123**, 714–733 (1929).

[2] M. Cascella and S. Vanni, *Toward accurate coarse-graining approaches for protein and membrane simulations*, Chemical Modelling **12**, 9781782622703–00001 (2015).

[3] M. J. F. et al., *Gaussian 16 Revision C.01*, Gaussian Inc. Wallingford CT, 2016.

[4] P. Carloni, U. Rothlisberger, and M. Parrinello, *The role and perspective of ab initio molecular dynamics in the study of biological systems*, Accounts of Chemical Research **35**, 455–464 (2002).

[5] K. Meier, A. Choutko, J. Dolenc, A. P. Eichenberger, S. Riniker, and W. F. Van Gunsteren, *Multi-resolution simulation of biomolecular systems: a review of methodological issues*, Angewandte Chemie International Edition **52**, 2820–2834 (2013).

[6] A. D. MacKerell Jr, D. Bashford, M. Bellott, R. L. Dunbrack Jr, J. D. Evanseck, M. J. Field, S. Fischer, J. Gao, H Guo, S. Ha, et al., *All-atom empirical potential for molecular modeling and dynamics studies of proteins*, The Journal of Physical Chemistry B **102**, 3586–3616 (1998).

[7] V. A. Voelz, G. R. Bowman, K. Beauchamp, and V. S. Pande, *Molecular simulation of ab initio protein folding for a millisecond folder ntl9 (1- 39)*, Journal of the American Chemical Society **132**, 1526–1528 (2010).

[8] K. Lindorff-Larsen, S. Piana, R. O. Dror, and D. E. Shaw, *How fast-folding proteins fold*, Science **334**, 517–520 (2011).

[9] R. O. Dror, H. F. Green, C. Valant, D. W. Borhani, J. R. Valcourt, A. C. Pan, D. H. Arlow, M. Canals, J. R. Lane, R. Rahmani, et al., *Structural basis for modulation of a g-protein-coupled receptor by allosteric drugs*, Nature **503**, 295 (2013).

[10] G. Zhao, J. R. Perilla, E. L. Yufenyuy, X. Meng, B. Chen, J. Ning, J. Ahn, A. M. Gronenborn, K. Schulten, C. Aiken, et al., *Mature hiv-1 capsid structure by cryo-electron microscopy and all-atom molecular dynamics*, Nature **497**, 643 (2013).

[11] D. Bassolino-Klimas, H. E. Alper, and T. R. Stouch, *Solute diffusion in lipid bilayer membranes: an atomic level study by molecular dynamics simulation*, Biochemistry **32**, 12624–12637 (1993).

[12] C. Hong, D. P. Tieleman, and Y. Wang, *Microsecond molecular dynamics simulations of lipid mixing*, Langmuir **30**, 11993–12001 (2014).

[13] G. A. Voth, *Coarse-graining of condensed phase and biomolecular systems* (CRC press, 2008).

[14] S. Izvekov and G. A. Voth, *A multiscale coarse-graining method for biomolecular systems*, The Journal of Physical Chemistry B **109**, 2469–2473 (2005).

[15] H. I. Ingólfsson, C. A. Lopez, J. J. Uusitalo, D. H. de Jong, S. M. Gopal, X. Periole, and S. J. Marrink, *The power of coarse graining in biomolecular simulations*, Wiley Interdisciplinary Reviews: Computational Molecular Science **4**, 225–248 (2014).

[16] T. A. Soares, S. Vanni, G. Milano, and M. Cascella, *Toward chemically resolved computer simulations of dynamics and remodeling of biological membranes*, The Journal of Physical Chemistry Letters **8**, 3586–3594 (2017).

[17] S. J. Marrink, H. J. Risselada, S. Yefimov, D. P. Tieleman, and A. H. De Vries, *The martini force field: coarse grained model for biomolecular simulations*, The Journal of Physical Chemistry B **111**, 7812–7824 (2007).

[18] D. Reith, M. Pütz, and F. Müller-Plathe, *Deriving effective mesoscale potentials from atomistic simulations*, Journal of Computational Chemistry **24**, 1624–1636 (2003).

[19] A. P. Lyubartsev, in *Coarse-grained modeling of biomolecules* (CRC Press, 2017), pp. 29–54.

[20] B. Hess, C. Kutzner, D. Van Der Spoel, and E. Lindahl, *Gromacs 4: algorithms for highly efficient, load-balanced, and scalable molecular simulation*, Journal of Chemical Theory and Computation **4**, 435–447 (2008).

[21] K. C. Daoulas and M. Müller, *Single chain in mean field simulations: quasi-instantaneous field approximation and quantitative comparison with monte carlo simulations*, The Journal of Chemical Physics **125**, 184904 (2006).

[22] K. C. Daoulas, M. Müller, J. J. De Pablo, P. F. Nealey, and G. D. Smith, *Morphology of multi-component polymer systems: single chain in mean field simulation studies*, Soft Matter **2**, 573–583 (2006).

[23] G. Fredrickson et al., *The equilibrium theory of inhomogeneous polymers*, Vol. 134 (Oxford University Press on Demand, 2006).

[24] F. Schmid, *Self-consistent-field theories for complex fluids*, Journal of Physics: Condensed Matter **10**, 8105 (1998).

[25] F. Schmid, *Theory and simulation of multiphase polymer systems*, Handbook of multiphase polymer systems, 31–80 (2011).

[26] J. A. Anderson, C. D. Lorenz, and A. Travesset, *General purpose molecular dynamics simulations fully implemented on graphics processing units*, Journal of Computational Physics **227**, 5342–5359 (2008).

[27] L. Schneider and M. Müller, *Multi-architecture monte-carlo (mc) simulation of soft coarse-grained polymeric materials: soft coarse grained monte-carlo acceleration (soma)*, Computer Physics Communications **235**, 463–476 (2019).

[28] G. Milano and T. Kawakatsu, *Hybrid particle-field molecular dynamics simulations for dense polymer systems*, The Journal of Chemical Physics **130**, 214106 (2009).

[29] A. De Nicola, T. Kawakatsu, and G. Milano, *Generation of well-relaxed all-atom models of large molecular weight polymer melts: a hybrid particle-continuum approach based on particle-field molecular dynamics simulations*, Journal of Chemical Theory and Computation **10**, 5651–5667 (2014).

[30] A. De Nicola, Y. Zhao, T. Kawakatsu, D. Roccatano, and G. Milano, *Validation of a hybrid md-scf coarse-grained model for dppc in non-lamellar phases*, Theoretical Chemistry Accounts **131**, 1167 (2012).

[31] A. De Nicola, Y. Zhao, T. Kawakatsu, D. Roccatano, and G. Milano, *Hybrid particle-field coarse-grained models for biological phospholipids*, Journal of Chemical Theory and Computation **7**, 2947–2962 (2011).

[32] G. Milano, T. Kawakatsu, and A. De Nicola, *A hybrid particle–field molecular dynamics approach: a route toward efficient coarse-grained models for biomembranes*, Physical Biology **10**, 045007 (2013).

[33] A. De Nicola, T. Kawakatsu, C. Rosano, M. Celino, M. Rocco, and G. Milano, *Self-assembly of triton x-100 in water solutions: a multiscale simulation study linking mesoscale to atomistic models*, Journal of Chemical Theory and Computation **11**, 4959–4971 (2015).

[34] Y. Zhao, M. Byshkin, Y. Cong, T. Kawakatsu, L. Guadagno, A. De Nicola, N. Yu, G. Milano, and B. Dong, *Self-assembly of carbon nanotubes in polymer melts: simulation of structural and electrical behaviour by hybrid particle-field molecular dynamics*, Nanoscale **8**, 15538–15552 (2016).

[35] S. J. Marrink, V. Corradi, P. C. Souza, H. I. Ingólfsson, D. P. Tieleman, and M. S. Sansom, *Computational modeling of realistic cell membranes*, Chemical Reviews **119**, 6184–6226 (2019).

[36] D. C. Rapaport, *The art of molecular dynamics simulation* (Cambridge university press, 2004).

[37] D. Frenkel and B. Smit, *Understanding molecular simulation: from algorithms to applications*, Vol. 1 (Elsevier, 2001).

[38] G. G. Vogiatzis, G. Megariotis, and D. N. Theodorou, *Equation of state based slip spring model for entangled polymer dynamics*, Macromolecules **50**, 3004–3029 (2017).

[39] M. Müller, *Studying amphiphilic self-assembly with soft coarse-grained models*, Journal of Statistical Physics **145**, 967–1016 (2011).

[40] T. Kawakatsu, *Statistical physics of polymers: an introduction* (Springer Science & Business Media, 2013).

[41] G. H. Fredrickson, V. Ganesan, and F. Drolet, *Field-theoretic computer simulation methods for polymers and complex fluids*, Macromolecules **35**, 16–39 (2002).

[42] R. W. Hockney and J. W. Eastwood, *Computer simulation using particles* (crc Press, 1988).

[43] G. Sevink, F Schmid, T Kawakatsu, and G Milano, *Combining cell-based hydrodynamics with hybrid particle-field simulations: efficient and realistic simulation of structuring dynamics*, Soft Matter **13**, 1594–1623 (2017).

[44] R. Courant, K. Friedrichs, and H. Lewy, *On the partial difference equations of mathematical physics*, IBM journal of Research and Development **11**, 215–234 (1967).

[45] M. Deserno and C. Holm, *How to mesh up ewald sums. i. a theoretical and numerical comparison of various particle mesh routines*, The Journal of Chemical Physics **109**, 7678–7693 (1998).

[46] J. C. Phillips, R. Braun, W. Wang, J. Gumbart, E. Tajkhorshid, E. Villa, C. Chipot, R. D. Skeel, L. Kale, and K. Schulten, *Scalable molecular dynamics with namd*, Journal of Computational Chemistry **26**, 1781–1802 (2005).

[47] Y. Zhao, A. De Nicola, T. Kawakatsu, and G. Milano, *Hybrid particle-field molecular dynamics simulations: parallelization and benchmarks*, Journal of Computational Chemistry **33**, 868–880 (2012).

[48] Y.-L. Zhu, H. Liu, Z.-W. Li, H.-J. Qian, G. Milano, and Z.-Y. Lu, *Galamost: gpu-accelerated large-scale molecular simulation toolkit*, Journal of Computational Chemistry **34**, 2197–2211 (2013).

[49] Y.-L. Zhu, Z.-Y. Lu, G. Milano, A.-C. Shi, and Z.-Y. Sun, *Hybrid particle–field molecular dynamics simulation for polyelectrolyte systems*, Physical Chemistry Chemical Physics **18**, 9799–9808 (2016).

[50] V. Tozzini, *Minimalist models for proteins: a comparative analysis*, Quarterly reviews of biophysics **43**, 333–371 (2010).

[51] D. Alemani, F. Collu, M. Cascella, and M. Dal Peraro, *A nonradial coarse-grained potential for proteins produces naturally stable secondary structure elements*, Journal of Chemical Theory and Computation **6**, 315–324 (2009).

[52] T. Darden, D. York, and L. Pedersen, *Particle mesh ewald: an $N \cdot \log(N)$ method for ewald sums in large systems*, The Journal of chemical physics **98**, 10089–10092 (1993).

[53] U. Essmann, L. Perera, M. L. Berkowitz, T. Darden, H. Lee, and L. G. Pedersen, *A smooth particle mesh ewald method*, The Journal of chemical physics **103**, 8577–8593 (1995).

[54] M. Frigo and S. G. Johnson, "Fftw: an adaptive software architecture for the fft", in Proceedings of the 1998 ieee international conference on acoustics, speech and signal processing, icassp'98 (cat. no. 98ch36181), Vol. 3 (IEEE, 1998), pp. 1381–1384.

[55] K. N. Kirschner, R. D. Lins, A. Maass, and T. A. Soares, *A glycam-based force field for simulations of lipopolysaccharide membranes: parametrization and validation*, Journal of chemical theory and computation **8**, 4719–4731 (2012).

[56] H. J. Risselada and S. J. Marrink, *Curvature effects on lipid packing and dynamics in liposomes revealed by coarse grained molecular dynamics simulations*, Physical Chemistry Chemical Physics **11**, 2056–2067 (2009).

Papers

I

Paper I

Hybrid Particle-Field Model for conformational Dynamics of Peptide Chains

Sigbjørn Løland Bore, Giuseppe Milano, Michele Cascella

Journal of Chemical Theory and Computation **14**, 1120–1130 (2018)

(This article is not included due to copyright restrictions)

Paper II

Hybrid Particle-Field Molecular Dynamics Simulations of Charged Amphiphiles in Aqueous Environment

II

Hima Bindu Kolli, Antonio De Nicola, Sigbjørn Løland Bore, Ken Schäfer, Gregor Diezemann, Jürgen Gauss, Toshihiro Kawakatsu, Zhongyuan Lu, You-Liang Zhu, Giuseppe Milano, Michele Cascella

Journal of Chemical Theory and Computation **14**, 4928–4937 (2018)

Hybrid particle-field molecular dynamics simulations of charged amphiphiles in aqueous environment

Hima Bindu Kolli,[†] Antonio de Nicola,[‡] Sigbjørn Løland Bore,[†] Ken Schäfer,[§] Gregor Diezemann,[§] Jürgen Gauss,[§] Toshihiro Kawakatsu,[‖] Zhong-Yuan Lu,[⊥] You-Liang Zhu,[#] Giuseppe Milano,[*,‡] Michele Cascella[*,†]

† Department of Chemistry and Hylleraas Centre for Quantum Molecular Sciences, University of Oslo, P.O. Box 1033 Blindern, 0315 Oslo, Norway

‡ Department of Organic Materials Science, Yamagata University, 4-3-16 Jonan Yonezawa, Yamagata-ken 992-8510, Japan

§ Institut für Physikalische Chemie, Johannes Gutenberg-Universität Mainz, Duesbergweg 10-14, 55128 Mainz, Germany

‖ Department of Physics, Tohoku University, Aoba, Aramaki, Aoba-ku, Sendai 980-8578, Japan

⊥ State Key Laboratory of Supramolecular Structure and Materials, Institute of Theoretical Chemistry, Jilin University, Changchun 130023, China

State Key Laboratory of Polymer Physics and Chemistry, Changchun Institute of Applied Chemistry, Chinese Academy of Sciences, Changchun 130022, China.

** email to: gmilano@yz.yamagata-u.ac.jp, michele.cascella@kjemi.uio.no*

Abstract

We develop and test specific coarse-grained models for charged amphiphilic systems such as palmitoyloleoyl phosphatidylglycerol (POPG) lipid bilayer, and sodium dodecyl sulphate (SDS) surfactant in aqueous environment, to verify the ability of the hybrid particle-field method to provide a realistic description of polyelectrolyte soft-matter systems. According to the hybrid approach, the intramolecular interactions are treated by a standard molecular Hamiltonian and the non-electrostatic intermolecular forces are described by density fields. Electrostatics is introduced as an additional external field obtained by a modified particle-mesh Ewald procedure, as recently proposed in [Phys. Chem. Chem. Phys 2016, 18, 9799]. Our results show that, upon proper calibration of key parameters, electrostatic forces can be correctly reproduced. Molecular dynamics simulations indicate that the methodology is robust with respect to the choice of the relative dielectric constant, yielding the same correct qualitative behavior for a broad range of values. In particular, our methodology reproduces well the organization of the POPG bilayer, as well as the SDS concentration-dependent change in the morphology of the micelles from spherical to microtubular aggregates. The inclusion of explicit electrostatics with good accuracy and low computational costs paves the way for a significant extension of the hybrid particle field method to biological systems, where the polyelectrolyte component plays a fundamental role for both structural and dynamical molecular properties.

1. Introduction

Amphiphiles are macromolecules characterized by well-defined hydrophobic and hydrophilic regions. Depending on the molecular shape and on the hydrophobic/hydrophilic balance, they tend to self-assemble into a variety of aggregates, like micelles and vesicles, lamellar structures like mono- and bilayers and structures with high aspect ratio like nanotubes and nanofibers.[1-4] These supramolecular structures are used in many industrial and biotechnological processes such as drug delivery systems,[5] micro- and nanoscale micellar reactors,[6] dispersants, detergents, emulsifiers, and coatings. The determination of the supramolecular structural organization of the amphiphilic molecule depends on a variety of factors, including the shape and flexibility of the single molecular structure the interplay of intra- and inter-molecular forces, and external thermodynamic factors like temperature, pressure, concentration, or ionic strength. Due to such complexity, the prediction and determination of the shape and size of amphiphiles, as well as their aggregation mechanisms, remains a challenging task both for experimentalist and computational scientists.

In recent times, scattering techniques such as small-angle X-ray scattering (SAXS)[7] or small-angle neutron scattering (SANS)[8,9] have been widely used for the quantitative characterization of the shape, internal structure, and interactions of macromolecular aggregates, like protein complexes in solution[10,11] as well as for micellar transformation studies.[12] Light scattering techniques are widely used to determine the shape of micelles in solution and Fluorescent spectroscopy is used to measure the aggregation number and the critical micelle concentration (CMC). Unfortunately, these techniques, having shortest temporal resolutions in the order of the millisecond, are not fast enough to capture the structural changes during the aggregation process.[13] Moreover, at lower concentrations, the interplay between shape variations and polydispersity complicates the data interpretation and could lead to ambiguous conclusions regarding the shape of surfactant micelles.

The picture is even more complex when studying biological amphiphilic systems like bio-membranes. Such bilayer structures present a chemically complex composition, being mostly formed by mixtures of phospholipids, with the addition, at very diverse stoichiometric ratios, of a variety of sphingolipids, cholesterol and the presence of both peripheral and transmembrane proteins.[14,15] Due to both their chemical complexity and their disordered nature, it is hardly possible t follow their dynamics and interactions in detail at the atomistic level.[16,17]

Computer modeling offers, in principle, an effective complementary way of exploring self-assembly processes at molecular resolution, and at highly controlled thermodynamic and stoichiometric conditions. Unfortunately, the assembling process occurs at the mesoscopic time- (>μs) and length-

scales (>100 nm), which are computationally expensive in a molecular dynamics framework employing explicit all-atom models.[18-24] For this reason, the use of coarse-grained (CG) simulations has become an alternative that aims to bridge the time and length scales involved in self-assembly phenomena.

The underlying assumption for the study of self-assembly phenomena at the CG scale is that neither the molecular structure at atomistic length scales nor its fast motion are relevant to the dynamics of the slow aggregation process. Therefore, molecular moieties can be conveniently described by a smaller number of order parameters considering just key properties like the amphiphilic nature of the individual molecular segments. CG models in both explicit and implicit solvent display a great potential for capturing critical phase behaviour of surfactants, phospholipid bilayers and generally in soft matter, as demonstrated, for example, in several studies available in the literature.[25-35]

Standard CG approaches are, in fact, subject to analogous technical computational bottlenecks of all atom models, produced by the need of the evaluation of distance-dependent intermolecular interactions.[36] As a consequence, unless massively parallel architectures are available, common CG simulations are limited to systems with sizes not larger than 100 nm length- and ~1-100 μs time scales.[37,38] These numbers are still too small compared to mesoscopic dimensionalities with length scales in the order of 100-1000 nm and time scales in the order of the millisecond.[39]

An alternative approach which is not bound to such limitation is the continuous field representation. In the framework of self-consistent field theory, the model systems are not represented by particles but by density fields and the mutual interactions between segments are decoupled and replaced by interactions with static external fields. These field-based approaches allow to simulate materials on scales much larger than the ones attainable with particle-based simulations. In recent years, the hybrid particle-field (hPF) approach combining a microscopic molecular representation to density-based potential has been introduced.[40-42] In particular, the determination of an analytical expression for local potential energy gradients, and consequently for the forces acting on the individual particles, allowed Milano and Kawakatsu to reformulate the hPF method within a molecular dynamics (MD) framework (hPF-MD hereafter).[43,44] The hPF-MD method was validated for different molecular models including molecular surfactants, atomistic models of polymers and bio membranes.[45-51]

More recently, an efficient electrostatic treatment based on the Ewald summation in the framework of hPF-MD has been proposed by Zhu et al.[52] Like for the density field, charged molecules are interacting with an external electrostatic field derived from the charge density. The long-range part of the Coulomb interaction is evaluated in reciprocal space using Fourier series just like in the standard particle-mesh Ewald method. The short-range part is evaluated by collecting the contributions of short range energy from the surrounding charges and matching with the Flory Huggins interaction parameter.

The explicit treatment of electrostatics opens up the possibility of using hPF schemes to investigate

major biological processes that are dominated by such interactions – for example ion-membrane permeation, membrane electroporation, protein/protein and protein/membrane interactions, or assembly and dynamics of nucleic acids. In fact, the hPF-MD method with electrostatics has been validated against particle-based simulations for model polyelectrolytes only.[52] In this work, we present the first application of hPF-MD to realistic soft matter models. The aim of the paper is to validate the models for charged amphiphile systems. Specifically, we investigated the ability of hPF-MD in describing both the structural properties of a constituted charged palmitoyloleoyl phosphatidylglycerol (POPG) bilayer, and the aggregation dynamics of sodium dodecyl-sulphate (SDS) in water. Our analysis provides a critical assessment of the quality performances of hPF-MD as a function of different external parameters, like the dielectric constant and χ parameters defining the effective interactions between particles and density field. The hPF-MD has been implemented in both serial and parallel versions of the OCCAM code.[47]

In section 2.1, a brief description of hPF-MD method is given. The treatment of the short- and long-range parts of the electrostatics interaction in hPF-MD is shown in the section 2.2. In section 2.3, the POPG and SDS models along with simulation details are given respectively. We discuss the calibration of the Ewald convergence parameter in section 3.1 and the simulation results on POPG bilayer and SDS aggregation are presented and discussed in sections 3.2 and 3.3. Final remarks and conclusions are presented in section 4.

2. Methods

2.1 The Hybrid Particle-Field approach

The hPF-MD method and its application to coarse-grained and atomistic models has been introduced in a series of former publications.[43-48,50,51] Here we only briefly recall the main ideas. In hPF-MD, a discrete particle based representation of several molecules interacting through pair forces between non-bonded particles, is formally transformed into a set of decoupled molecules subject to an external potential depending on density fields.

Under this transformation and considering the following functional form for the potential energy,

$$W[\{\phi(\boldsymbol{r})\}] = \frac{1}{\phi_0}\int d\boldsymbol{r}\,\left(\frac{k_B T}{2}\sum_{ij}\chi_{ij}\phi_i(\boldsymbol{r})\phi_j(\boldsymbol{r}) + \frac{1}{2\kappa}\left(\sum_i \phi_i(\boldsymbol{r}) - \phi_0\right)^2\right) \quad (1)$$

applying the saddle point approximation, by functional differentiation it is possible to obtain the mean-field external potential $V_i^{ext}(\boldsymbol{r})$ acting on an individual particle of type *i* at position $\boldsymbol{r}$, which takes the form:

$$V_i^{ext}(\boldsymbol{r}) = \frac{\delta W[\{\phi(\boldsymbol{r})\}]}{\delta \phi_i(\boldsymbol{r})} = \frac{1}{\phi_0}\left(k_B T \sum_j \chi_{ij}\phi_j(\boldsymbol{r}) + \frac{1}{\kappa}\left(\sum_j \phi_j(\boldsymbol{r}) - \phi_0\right)\right) \quad (2)$$

In equations 1, 2 k_B is the Boltzmann constant, *T* is the temperature of the system, $\phi_i(\boldsymbol{r})$ is the coarse-grained number density of the species *i* at position ***r,*** χ_{ij} is the mean field interaction strength between particles of type *i* and *j*, κ is a compressibility parameter acting against local density inhomogeneity, and ϕ_0 is the total number density of the system.

The forces acting on the individual particles are computed as the spatial gradients of the same potential in equation 2. The density field and its gradient are computed on a spatial grid and updated with a time interval $\tau > \Delta t$, where Δt is the MD time-step. This ensures fast computation of forces, in an embarrassingly parallel implementation. More details about the derivation of equation 2 and its implementation in MD simulations are reported in references [43,44,47].

2.2 The hybrid Particle-Field method with electrostatics

The electrostatic potential $\psi(\boldsymbol{r})$ produced by a distribution of charges $\rho(\boldsymbol{r})$ is computed by solving the Poisson equation:

$$-\nabla^2\psi(\boldsymbol{r}) = \frac{\rho(\boldsymbol{r})}{\varepsilon_r\varepsilon_0} \quad (3)$$

where ε_0 is the vacuum permittivity, and ε_r is the relative dielectric constant of the medium. Adopting periodic boundary conditions, the solution of the equation 3 yields the potential field $\psi(\boldsymbol{r})$:

$$\psi(\boldsymbol{r}) = \frac{1}{4\pi\varepsilon_r\varepsilon_0}\sum_{\boldsymbol{n}}\sum_{j=1}^{N}\frac{q_j}{|\boldsymbol{r}-\boldsymbol{r_j}+\boldsymbol{nL}|} \quad (4)$$

Here, the vector $\mathbf{L} = (\mathbf{L_1}, \mathbf{L_2}, \mathbf{L_3})$ defines the simulation box, and $\mathrm{n}\mathbf{L} = \mathrm{n}_1\mathbf{L_1} + \mathrm{n}_2\mathbf{L_2} + \mathrm{n}_3\mathbf{L_3}$ is the translation over a generic periodic image. Recently, an efficient method based on the particle-mesh Ewald summation was implemented in hybrid particle field simulations to compute the electrostatic potential shown in equation 4.[47] The short-range and long-range parts of the electrostatic potential in conventional Ewald sum are written as:

$$\psi^S(\boldsymbol{r}) = \frac{1}{4\pi\varepsilon_0\varepsilon_r}\sum_n\sum_j\frac{q_j\mathrm{erfc}(\alpha|\boldsymbol{r}-\boldsymbol{r_j}+n\boldsymbol{L}|)}{|\boldsymbol{r}-\boldsymbol{r_j}+n\boldsymbol{L}|} \quad (5)$$

$$\psi^L(\boldsymbol{r}) = \sum_{m\neq 0}\hat{\psi}^L(\mathbf{m})\exp(i\,\boldsymbol{m}\cdot\boldsymbol{r}) \quad (6)$$

where ψ^S is the short-range part, and ψ^L is the long-range part of the electrostatic potential. $\hat{\psi}^L$

denotes ψ^L in the reciprocal space, and it is given by:

$$\hat{\psi}^L(\boldsymbol{m}) = \frac{exp(-\mathbf{m}^2/4\alpha^2)}{\varepsilon_0\varepsilon_r V\mathbf{m}^2}\sum_{j=1}^{N} q_j \exp(-i\,\boldsymbol{m}\cdot r_j) \quad (7)$$

where V is the volume of the simulation box, **m** is the reciprocal space vector, and α is the Ewald's convergence parameter.

In hPF-MD, the charge density is expressed in terms of $Q(\boldsymbol{l}) = Q(l_1, l_2, l_3)$, the distribution of charges at the lattice points. The long-range part of the electrostatic potential at the lattice point $\boldsymbol{l}$, is computed using forward (F) and backward (F^{-1}) discrete Fourier transforms:

$$\psi^L(\boldsymbol{l}) = \sum_{m_1=0}^{N_1-1}\sum_{m_2=0}^{N_2-1}\sum_{m_3=0}^{N_3-1} \hat{\psi}^L(\boldsymbol{m})\exp\left[2\pi i\frac{m_1 l_1}{N_1}+\frac{m_2 l_2}{N_2}+\frac{m_3 l_3}{N_3}\right]$$

$$= F^{-1}\left[\left(\frac{\exp\left(\frac{-\boldsymbol{m}^2}{4\alpha^2}\right)}{\varepsilon_0\varepsilon_r V\boldsymbol{m}^2}\right) FQ\right](l_1, l_2, l_3) \quad (8)$$

The short-range part of the electrostatic potential at the lattice point of spatial position $\boldsymbol{l}$ is given by:

$$\psi^S(\boldsymbol{l}) = \frac{z_{CN}}{4\pi\varepsilon_0\varepsilon_r}\frac{\mathrm{erfc}(\alpha\sigma)}{\sigma}Q(\boldsymbol{l}) \quad (9)$$

where the parameter z_{CN} is the coordination number which takes a value of 6 for a three-dimensional cubic lattice and σ is the particle diameter. Instead of the pairwise short-range electrostatic interactions like in classic Ewald summation, the interactions are now transmitted through the mean field. The charge density and the electrostatic potential are computed on the same grid as the one used for the density field.

2.3 Simulation Details

2.3.1 POPG bilayer The POPG bilayer model was composed of 1216 POPG lipids (608 lipids for each layer), 64448 water beads, each with a density of 4 water molecules, and 1216 Na^+ counterions necessary for charge neutralization in a 20.18×20.18×23.29 nm^3 periodic box. The CG mapping of POPG is explained in Figure 1. Each POPG has a polar head (P) with net charge -1. The bead type D

mimics the presence of a double-bond in one of the aliphatic tails. The intramolecular parameters for POPG were taken from the literature.[25,53]

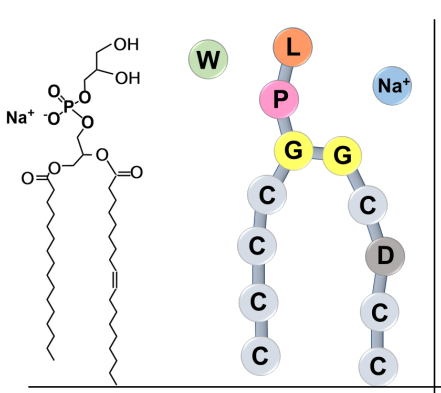

Interaction matrix $\tilde{\chi}_{ij} = \chi_{ij}.RT$ (kJ mol^{-1}) for POPG/water system

$\tilde{\chi}_{ij}$	L	P	G	C	D	Na+	W
L	0.00	-3.60	4.50	13.25	9.30	-6.00	0.00
P	-3.60	0.00	2.50	13.50	11.70	0.00	-3.60
G	4.50	2.50	0.00	8.30	8.30	-3.00	4.50
C	13.25	13.50	8.30	0.00	0.00	13.50	33.75
D	9.30	11.70	8.30	0.00	0.00	9.30	23.25
Na+	-6.00	0.00	-3.00	13.50	9.30	0.00	0.00
W	0.00	-3.60	4.50	33.75	23.25	0.00	0.00

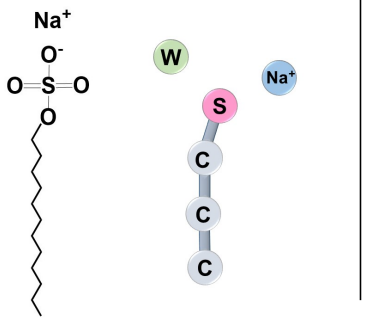

Interaction matrix $\tilde{\chi}_{ij} = \chi_{ij}.RT$ (kJ mol^{-1}) for SDS/water system

$\tilde{\chi}_{ij}$	S	C	Na+	W
S	0.00	13.50	0.00	-3.60
C	13.50	0.00	13.50	33.75
Na+	0.00	13.50	0.00	0.00
W	-3.60	33.75	0.00	0.00

Figure 1. CG model and particle field interaction parameters of POPG/water and SDS/water. *Top left:* Structure of POPG and CG mapping. *Top right:* Table showing the particle–field interaction parameters for the POPG/ water system. *Bottom left:* Structure of SDS and CG mapping. *Bottom right:* Table showing the particle–field interaction parameters for the SDS/water system.

First, the POPG bilayer was relaxed over 2 μs of particle-particle (PP) CG simulations, using the MARTINI force field.[53] The CG simulations were run in the NpT ensemble at 301.15K and 1 bar, using semi-isotropic pressure coupling. Electrostatic interactions were computed via particle-mesh Ewald summation, using a dielectric constant $\varepsilon_r = 15$, and a grid of 0.3 nm mesh. A cut-off of 1.5nm was used to truncate the van der Waals terms. The PP-CG simulations were run using the GROMACS 4.5.4 package.[54]

The final configuration obtained from the PP-CG run, was used as the starting configuration for the hPF-MD simulations. All intramolecular interactions were treated in the same manner as in the PP-CG simulations. The particle field parameters $\tilde{\chi}_{ij} = \chi_{ij}RT$ (where R is the gas constant) needed to

calculate the intermolecular interactions between particle types i and j are listed in figure 1. The value of the incompressibility parameter κ^{-1} was set to 4 RT, in agreement with previous simulations of water/lipid mixtures.[45,46,48] We consider the same grid size (32×32×36) for both particle and charge fields. The size of the grid has been chosen to keep the cell length, b ≈ 0.65nm and the explanation for this choice is given in section 3.1. The hPF-MD simulations were run using a time step of 0.03 ps in NVT ensemble, at a temperature of 301.15 K using an Andersen thermostat[55] with collision frequency of 7 ps^{-1}. A density-field update time interval $\tau = 100\ \Delta t$ was employed for both particle and charge densities.

2.3.2 SDS aggregation The SDS molecules were represented by a chain of four beads as shown in Figure 3. Each chain consists of one hydrophilic polar head bead (S) with a charge of -1 charge units and three hydrophobic beads (C1, C2 and C3), each one representing four CH2/CH3 units. The SDS bonded parameters are taken from ref. [56] The interaction matrix $\tilde{\chi}_{ij}$ used for hPF-MD are given in Figure 1. The value of the compressibility was set to κ^{-1} = 4 RT. The density update was set to $\tau = 100\ \Delta t$.

The hPF-MD simulations were performed at four different SDS concentrations: C_{SDS} = 50 mM, 72 mM, 182 mM and 400 mM, using a cubic periodic box of edge 33.2 nm, containing 1120, 1600, 4000, and 8815 SDS molecules, respectively. The chosen concentrations are all significantly higher than the CMC for SDS, which is 8 mM. An equal number of Na^+ beads were added to act as counterions; roughly ~300,000 water beads were used in all simulations. All the four systems and their compositions are shown in table 1. We consider a grid size of 50×50×50 for both charge and particle fields.

Initially, SDS, Na^+, an water were placed at random positions in the simulation box. All MD runs were performed in the NVT ensemble using Δt = 0.03 ps keeping the temperature constant at 298 K using the Andersen thermostat[55] with a collision frequency of 7 ps^{-1}.

All the hPF-MD simulations of both POPG and SDS systems were run using the parallel version of OCCAM code.[47]

Table 1. SDS systems simulated and the composition of the systems

C_{SDS}	Total no. of particles in the box	Number of SDS molecules	No. of Na^+ ions	No. of water beads
50 mM	309600	1120	1120	304000
72 mM	304000	1600	1600	296000
182 mM	306000	4000	4000	286000
400 mM	317075	8815	8815	273000

3. Results and discussion

3.1 Calibration of Ewald parameters and grid size

The hPF-MD implementation relies on a modified particle-mesh Ewald treatment to determine the short- and long-range components of the electrostatic potential. The accuracy of this approach is dependent on the grid spacing and the spread of the auxiliary Gaussian charge distribution α (equation 7). To assess this dependence, we used a model system comprised of two oppositely unit charged particles at a distance d along the z-axis in a large simulation box of edge L= 20.0 nm. Figure 2 reports the intensity of the electrostatic forces acting on the two charges as a function of the grid spacing and α, as well as the theoretical Coulomb force F_C. The profiles indicate that for values of α larger than 2.35 nm^{-1}, our implementation consistently reports similar values of the forces. For a grid of 0.65 nm, the corresponding average relative errors are 4%, while for smaller α, the error on the forces increases to 10 %. This is due to the fact that the Gaussian spread of the charge is inconsistently represented by the actual distribution of the charges on the mesh points. Furthermore, by grid refinement to a spacing of 0.45 nm, greater accuracy, especially at short distances, is achieved with an average relative error of

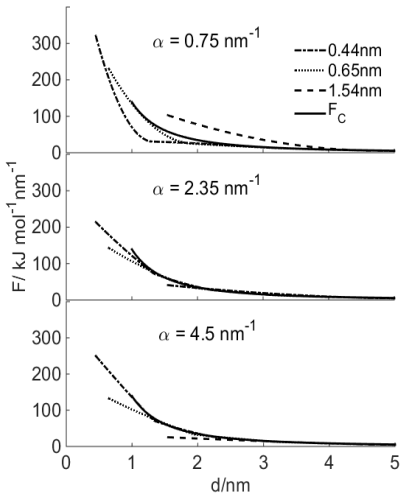

Figure 2. Electrostatic forces acting on two unit charges as a function of the distance between charges using different α values, and different grid spacing as reported in the legend. *Top*: electrostatic force for α = 0.75 nm^{-1}. *Middle*: electrostatic force for α = 2.35 nm^{-1}. *Bottom:* electrostatic force for α = 4.5 nm^{-1}. All values are compared to the theoretical Coulomb force F_C.

3%. In agreement with these findings, all the simulations were run using a value of grid spacing of 0.65 nm and $\alpha = 2.35\ nm^{-1}$.

3.2 POPG bilayer

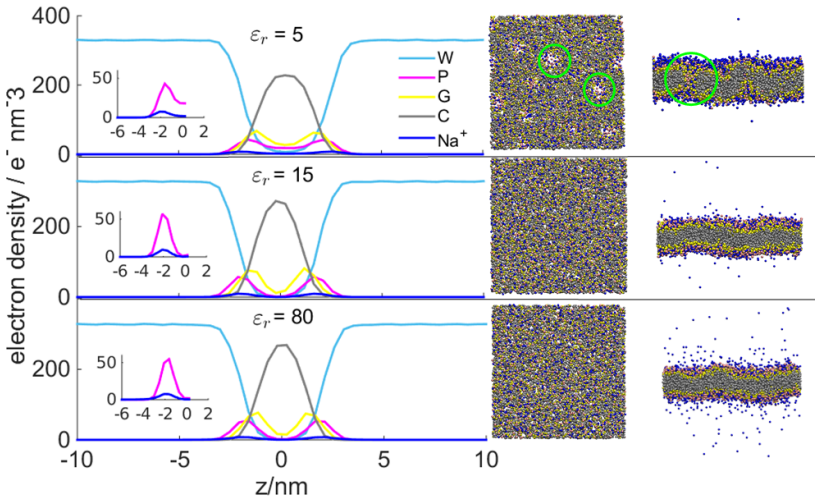

Figure 3. *Left:* The number density profile of POPG, Na^+ and water obtained from 1 μs long hPF-MD simulations with ε_r = 5, 15, and 80. *Right:* Snapshots with top and side-view of the bilayers. Water is not shown for clarity. The green circles evidence the formation of pores.

The bilayer structure of POPG was simulated using different values of the relative dielectric constant ε_r in the NVT ensemble by hPF-MD simulations. Figure 3 shows the number density profile of the POPG/water system at ε_r = 5, 15 and 80 obtained from the last 1μs out of a 2 μs long hPF-MD run along the direction normal to the plane of the bilayer. For very small values of ε_r, we observed the formation of strong ion-pairs between the positively charged Na^+ ions and the negatively charged P beads of POPG. The localization of Na^+ in the neighborhood of the lipid heads reduced drastically the effective charge at the surface of the lipids, thus enhancing the tendency of POPG to aggregate. As a result, the lateral tension of the membrane produced poration of the membrane.

In fact, the organization of POPG in a self-assembled structure is the result of the balance among competing interactions, in particular, the attractive collapse of the hydrophobic tails, the electrostatic repulsion of the charged heads, and the entropy. The electrostatic repulsion is screened by the formation of ion pairs, thus favoring the collapse of the lipids. At NVT conditions, and in periodic boundary conditions, stable flat bilayers are observed only if the global free-energy balance between such interactions produces POPG aggregates characterized by a surface area-per-lipids close to a value

$A=N_{POPG}/(L_iL_j)$, where N_{POPG} is the number of lipids in one leaflet, and L_i, L_j are the lengths of two edges of the box.

Values of ε_r higher than 10 yielded a stable bilayer structure. In these cases, the lipid moiety showed an organized lamellar structure, with a symmetric distribution of the components in the two leaflets. Overall, the thickness of the bilayer D_{HH} given appears less pronounced than in other molecular models,[57-60] and in very good agreement with experimental data (Table S1, in Supporting Information (SI)). The rather broad distribution of the G beads indicates that the membrane is quite disordered, with appearing fast-dissipating undulations, clearly observable by visual inspection of the simulation trajectory. The appearance of local distortions is correlated to the binding dynamics of the Na^+ counterions on the membrane surface. As expected, the increase in the dielectric constant, and the consequent weakening of the electrostatic forces, results into a reduced adsorption of the counterions (Figure S1, SI), and a different binding dynamic for the ions.

At very low value of the dielectric constant, we observe different shape fluctuations of the membrane. A quantitative measure of such distortions can be obtained using the Helfrich continuum model[61-65], as explained in detail in SI.

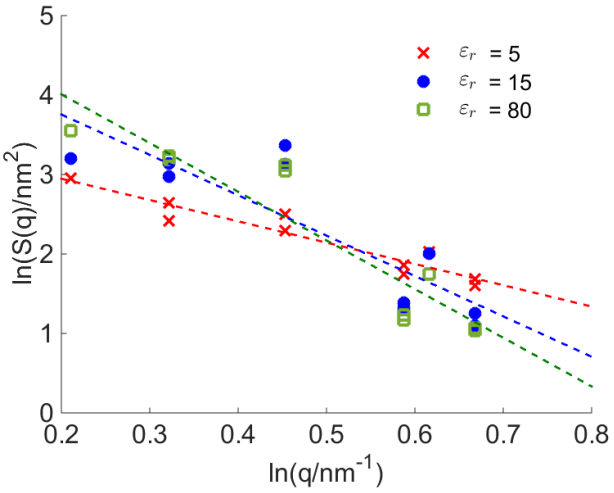

Figure 4. Frequency spectrum of POPG undulations. Intensity of the vibrational frequencies as a function of the wave number q obtained from hPF-MD simulations using three different values of ε_r = 5, 15, 80.

Figure 4 reports the fluctuation spectrum of the POPG membrane computed over the last 100 ns of the simulations. In all systems, undulations dominate at wavenumbers q smaller than 1.5 nm^{-1}.

Nonetheless, simulations at ε_r = 5 show a suppression of the low-frequency modes, and some activation of modes at higher frequency compared to simulations at ε_r = 15, and 80. Simulations at ε_r = 15 and 80 show instead a different distribution of the amplitude in the low-frequency regions, in particular, with the activation of fluctuations at wavenumbers ($q < 2$ nm^{-1}), with similar values of the amplitudes. This confirms that the morphology of the membrane is stable in a broad range of dielectric values, with the increased screening of the dielectric compensating for the unbinding of the ions from the membrane surface.

3.3 SDS Self-assembly

We simulated four different SDS/water systems with SDS concentrations C_{SDS} = 50 mM, 72 mM, 182 mM, and 400 mM for different values of ε_r, over up to 5 μs, starting from a randomly dispersed distribution of the SDS molecules and the Na^+ ions in water. Figure 5 shows the average aggregation number of SDS $\langle N_{agg} \rangle$ plotted with respect to time. N_{agg} is computed by counting the number of micelles and the molecules in each micelle with cut-off distance 1.7 σ for each configuration using the linked list algorithm. The cut-off distance was defined as 0.8 nm, corresponding to the first minimum of the radial distribution function between the P-N species. In all cases, we observed an almost instantaneous formation of small SDS aggregates, corresponding to a continuous increase of N_{agg}. With time, such small moieties fuse together to form progressively larger and larger micelles. These events correspond to a continuous rather than step-wise increase of the N_{agg} value.

The size and the shape of the micelle are directly dependent on the SDS concentration and the value of the dielectric constant. In particular, for medium values of the dielectric constant (ε_r = 45), regular spherical micelles were formed when the concentration of SDS was relatively low (C_{SDS} = 50, 72 mM). Increasing the SDS concentration (C_{SDS} = 182 mM) led to spheroidal micelles with a prolate character, and eventually to the formation of nanotubular structures (C_{SDS} = 400mM), in agreement with experiment, and previous calculations using different models.[66-68] On the contrary, high values of the dielectric constant (ε_r = 80) yielded smaller micelles that are of spherical shapes also at higher concentrations of SDS. For smaller values of ε_r (~15), the hPF-MD simulations did not produce regular assemblies, but systematically predicted a phase of irregularly-dispersed aggregated surfactants, which does not correspond to any experimentally observed assembly.

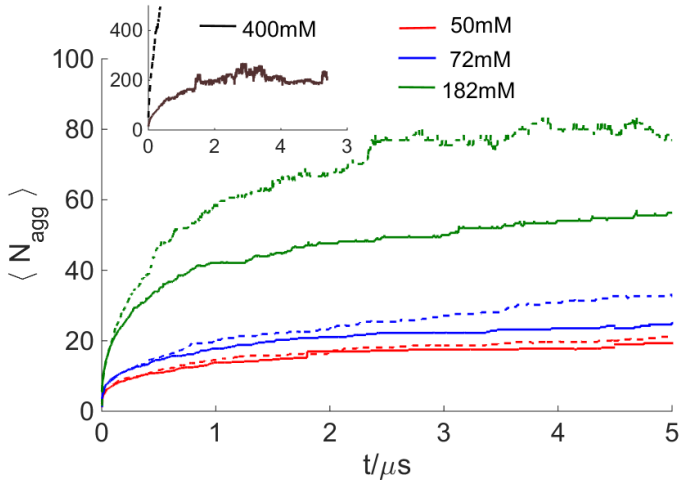

Figure 5. Average aggregation number versus time for C_{SDS} = 50 mM, 72 mM, and 182 mM. $\langle N_{agg} \rangle$ is plotted for each concentration at ε_r = 45 (dashed lines), and ε_r = 80 (solid lines). The inset shows the aggregation behaviour at high SDS concentration C_{SDS} = 400mM.

The aggregation mechanism of SDS observed in our simulations is in qualitative agreement with the kinetic mechanism proposed by Lund et al. [69] First individual SDS units rapidly accumulate to form small assemblies. The fast depletion of monomeric SDS from the solution leads to formation of rather regular spherical micelles, of diameter 0.3 nm - 0.4 nm, corresponding to roughly twice the contour length of a single SDS molecule. At this point, further growth of the micelle occurs by fusion of such aggregates rather than by accumulation of individual SDS units. The growth produces prolate spheroidal micelles that eventually fuse to form nano-tubular structures. This mechanism can be quantified following the evolution of the asphericity parameter δ of the micelle introduced by Rudnick and Gaspari.[70] This value is bounded between 0 and 1, with δ taking the values close to 0 for spherical assemblies, and reaching 1 if all the particles lie on a line (see SI).

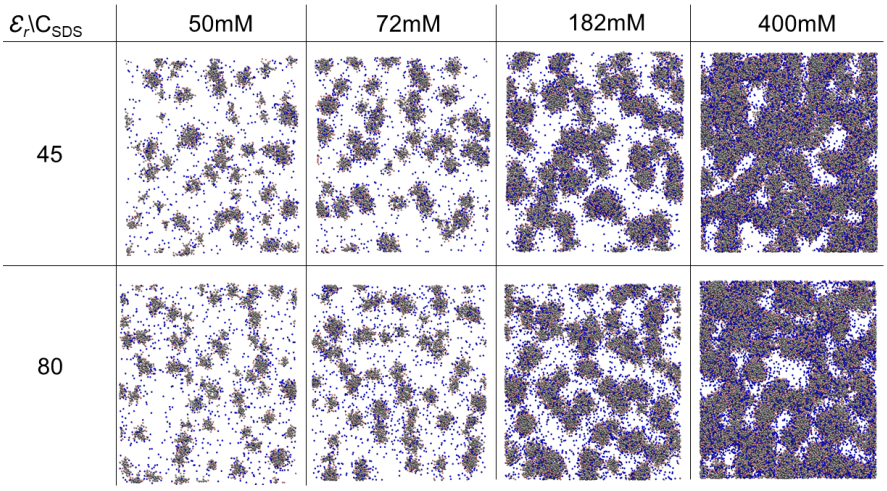

Figure 6. Final snapshots taken after 5μs of the simulations for C_{SDS} = 50 mM, 72 mM, 182 mM, and 400mM at ε_r = 45 and 80. Water is not shown for visual clarity.

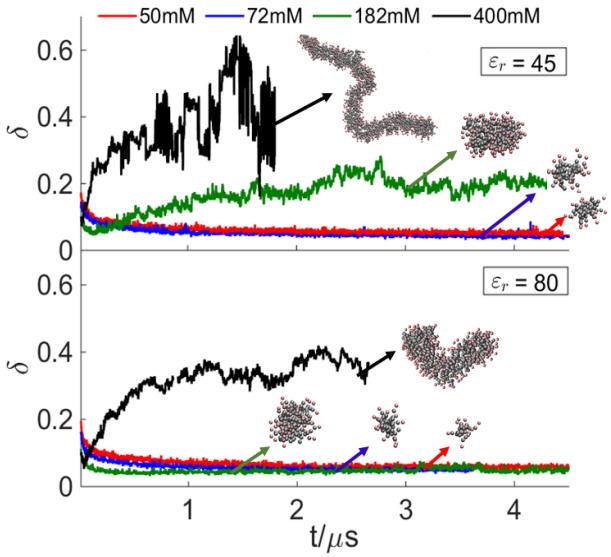

Figure 7. Asphericity parameter δ with respect to time for C_{SDS} = 50mM, 72mM, 182 mM, and 400 mM at ε_r = 45 (top panel) and ε_r = 80 (bottom panel).

Regardless of the dielectric, at all concentrations δ rapidly develops to values close to 0, indicating the initial formation of regular spherical structures (Figure 7); for higher concentrations, with ε_r = 45, δ then increases over time, signaling the metamorphosis from spherical to spheroidal (δ ~ 0.2, C_{SDS} = 182 mM) or nano-tubular aggregates (δ ~ 0.4, C_{SDS} = 400 mM). This phenomenon occurs by fusion of smaller spherical units rather than by continuous aggregation of monomeric SDS. The mechanism of fusion into tubular moieties occurs at the poles of the prolate axis of the SDS micelle, as also proposed by Lund et al. [71,69]

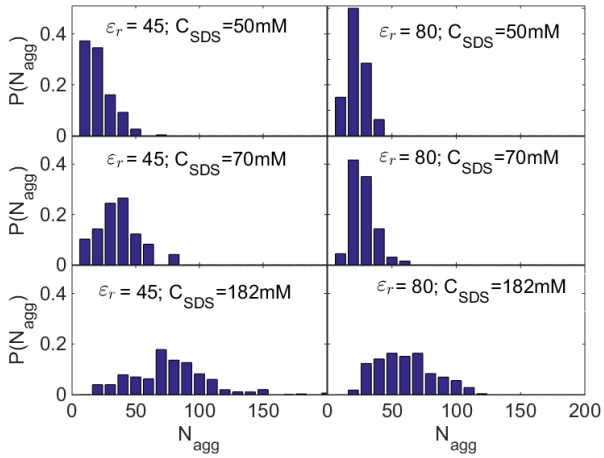

Figure 8. Probability distribution of number of micelles versus micelle size for different concentrations of SDS and value of the relative dielectric constant.

The average aggregation number of the spherical SDS micelles predicted by our model is somewhat smaller than the experimentally measured one (N_{agg} = 54 for C_{SDS} = 50mM, and N_{agg} = 68 for C_{SDS} = 72mM).[72] In fact, our samples were constituted by a very broad dispersion of micelles of different size, as evident from Figure 8 including micelles as big as those reported by the experiment, which formed in the last microseconds of simulations. It is thus likely that the smaller sizes of the micelles that we observed is a consequence of both the initial conditions (random dispersion of SDS) very far from the thermodynamic equilibrium, and the relatively short sampling time, which promotes the formation of smaller metastable micelles, which may require some activation in order to fuse into larger aggregates.

4. Final remarks and conclusion

This work showed how our new implementation of grid-based electrostatic solvers for particle-field simulations can be used to investigate realistic models of polyelectrolyte soft-matter systems. In

particular, we demonstrated that the hPF-MD approach is capable of treating amphiphilic systems either in extended aggregates, like a lipid bilayer, or in finite micellar forms. In particular, the model predicts in a qualitatively correct manner the effect of charge interactions over the morphology of the aggregates in terms of either area per lipid in bilayers, or shape and size of micelle aggregates. The predicted results are affected by the appropriate choice of the relative dielectric constant, as previously reported in other coarse-grained simulations. In fact, the behavior of these systems is dominated by the formation of ion pairs and their stability, which strongly depends on the relative hydration of the region where they occur.

The behavior of the two POPG and SDS systems is influenced by the choice of the relative dielectric constant in different ways. In particular, the assembly of the POPG bilayer seems to be loosely influenced by the choice of ε_r, yielding very good results already at relatively low values of ε_r. On the contrary, the assembly dynamics and the stability of different phases of SDS seem to be strongly dependent on the values of ε_r, and requiring relatively high ε_r values to avoid the appearance of gelatinous phases that are inconsistent with experiment.

The ability of hPF models to treat explicit electrostatics in good agreement with experiment opens up the possibility of simulating efficiently biological moieties where the polyelectrolyte character is dominant; for example, combining it to proposed models for polypeptides with explicit electrostatics.[73-76] Finally, our analysis points to the importance of carefully calibrating ε_r in studies that aim to determine dynamic or structural properties of soft-matter assemblies, especially in very specific thermodynamic conditions.

Acknowledgment

This work received the support of the Norwegian Research Council through the CoE Hylleraas Centre for Quantum Molecular Sciences (Grant No. 262695), and by the Norwegian Supercomputing Program (NOTUR) (Grant No. NN4654K). HBK received funding from the European Union's Horizon 2020 research and innovation programme under the Marie Skłodowska-Curie grant agreement No. 704491. GM and ADN wish to thank the HPC team of Enea (http://www.enea.it) for using the ENEA-GRID and the HPC facilities CRESCO (http://www.cresco.enea.it) in Portici. KS, GD and JG acknowledge financial support by the Deutsche Forschungsgemeinschaft via the TRR 146 "Multiscale Simmulation Methods for Soft Matter Systems" .

References

(1) Seidel, C. *Physics of amphiphiles: Micelles, vesicles and microemulsions.*; North Holland Physics Publishing: Amsterdam/Oxford/New York/Tokyo, 1986; Vol. 37.
(2) Gerhard Gompper, M. S., Cyril Domb, Joel L. Lebowitz In *Phase Transitions and Critical Phenomena*; Academic Press: 1994; Vol. 16.
(3) Velonia, K.; Cornelissen, J. J. L. M.; Feiters, M. C.; Rowan, A. E.; Nolte, R. J. M. In *Nanoscale Assembly: Chemical Techniques*; Huck, W. T. S., Ed.; Springer US: Boston, MA, 2005, p 119-185.
(4) Lombardo, D.; Kiselev, M. A.; Magazù, S.; Calandra, P. Amphiphiles Self-Assembly: Basic Concepts and Future Perspectives of Supramolecular Approaches *Adv. Cond. Matter Phys.* **2015**, *2015*, 151683.
(5) Salim, M.; Minamikawa, H.; Sugimura, A.; Hashim, R. Amphiphilic designer nano-carriers for controlled release: from drug delivery to diagnostics *MedChemComm* **2014**, *5*, 1602-1618.
(6) Wang, F.; Wen, M.; Feng, K.; Liang, W.-J.; Li, X.-B.; Chen, B.; Tung, C.-H.; Wu, L.-Z. Amphiphilic polymeric micelles as microreactors: improving the photocatalytic hydrogen production of the [FeFe]-hydrogenase mimic in water *Chem. Commun.* **2016**, *52*, 457-460.
(7) Chu, B.; Liu, T. Characterization of Nanoparticles by Scattering Techniques *J. Nanopart. Res.* **2000**, *2*, 29-41.
(8) Chen, S. H. Small Angle Neutron Scattering Studies of the Structure and Interaction in Micellar and Microemulsion Systems *Annu. Rev. Phys. Chem.* **1986**, *37*, 351-399.
(9) Hamley, I. W.; Pedersen, J. S.; Booth, C.; Nace, V. M. A Small-Angle Neutron Scattering Study of Spherical and Wormlike Micelles Formed by Poly(oxyethylene)-Based Diblock Copolymers *Langmuir* **2001**, *17*, 6386-6388.
(10) Koch, M. H. J.; Vachette, P.; Svergun, D. I. Small-angle scattering: a view on the properties, structures and structural changes of biological macromolecules in solution *Q. Rev. Biophys.* **2003**, *36*, 147-227.
(11) Mertens, H. D. T.; Svergun, D. I. Structural characterization of proteins and complexes using small-angle X-ray solution scattering *J. Struct. Biol.* **2010**, *172*, 128-141.
(12) Schmölzer, S.; Gräbner, D.; Gradzielski, M.; Narayanan, T. Millisecond-Range Time-Resolved Small-Angle X-Ray Scattering Studies of Micellar Transformations *Phys. Rev. Lett.* **2002**, *88*, 258301.
(13) Di Cola, E.; Grillo, I.; Ristori, S. Small Angle X-ray and Neutron Scattering: Powerful Tools for Studying the Structure of Drug-Loaded Liposomes *Pharmaceutics* **2016**, *8*, 10.
(14) Seddon, J. M.; Templer, R. H. In *Handbook of Biological Physics*; Lipowsky, R., Sackmann, E., Eds.; North-Holland: 1995; Vol. 1, p 97-160.
(15) Gutberlet, J. K. T. *Lipid Bilayers*; Springer-Verlag Berlin Heidelberg, 2001.
(16) Engelman, D. M. Membranes are more mosaic than fluid *Nature* **2005**, *438*, 578.
(17) van Meer, G.; Voelker, D. R.; Feigenson, G. W. Membrane lipids: where they are and how they behave *Nat. Rev. Mol. Cell Biol.* **2008**, *9*, 112.
(18) Lee, E. H.; Hsin, J.; Sotomayor, M.; Comellas, G.; Schulten, K. Discovery Through the Computational Microscope *Structure*, *17*, 1295-1306.
(19) Lyubartsev, A. P. Multiscale modeling of lipids and lipid bilayers *Eur. Biophys. J.* **2005**, *35*, 53.
(20) Gunsteren, W. F. v.; Bakowies, D.; Baron, R.; Chandrasekhar, I.; Christen, M.; Daura, X.; Gee, P.; Geerke, D. P.; Glättli, A.; Hünenberger, P. H.; Kastenholz, M. A.; Oostenbrink, C.; Schenk, M.; Trzesniak, D.; Vegt, N. F. A. v. d.; Yu, H. B. Biomolecular Modeling: Goals, Problems, Perspectives *Angew. Chem. Int. Edit.* **2006**, *45*, 4064-4092.
(21) Jena, B. P. In *Method. Cell Biol.*; Academic Press: 2008; Vol. 90, p 19-37.
(22) Sapay, N.; Tieleman, D. P. In *Curr. Top. Membr.*; Feller, S. E., Ed.; Academic Press: 2008; Vol. 60, p 111-130.
(23) Lyubartsev, A. P.; Rabinovich, A. L. Recent development in computer simulations of lipid bilayers *Soft Matter* **2011**, *7*, 25-39.

(24) Monticelli, L.; Tieleman, D. P. In *Biomolecular Simulations: Methods and Protocols*; Monticelli, L., Salonen, E., Eds.; Humana Press: Totowa, NJ, 2013, p 197-213.
(25) Marrink, S. J.; de Vries, A. H.; Mark, A. E. Coarse Grained Model for Semiquantitative Lipid Simulations *J. Phys. Chem. B* **2004**, *108*, 750-760.
(26) Izvekov, S.; Voth, G. A. A Multiscale Coarse-Graining Method for Biomolecular Systems *The Journal of Physical Chemistry B* **2005**, *109*, 2469-2473.
(27) Müller, M.; Katsov, K.; Schick, M. Biological and synthetic membranes: What can be learned from a coarse-grained description? *Phys. Rep.* **2006**, *434*, 113-176.
(28) Monticelli, L.; Kandasamy, S. K.; Periole, X.; Larson, R. G.; Tieleman, D. P.; Marrink, S.-J. The MARTINI Coarse-Grained Force Field: Extension to Proteins *J. Chem. Theory Comput.* **2008**, *4*, 819-834.
(29) Marrink, S. J.; de Vries, A. H.; Tieleman, D. P. Lipids on the move: Simulations of membrane pores, domains, stalks and curves *Biochim. Biophys. Acta* **2009**, *1788*, 149-168.
(30) Murtola, T.; Bunker, A.; Vattulainen, I.; Deserno, M.; Karttunen, M. Multiscale modeling of emergent materials: biological and soft matter *Phys. Chem. Chem. Phys.* **2009**, *11*, 1869-1892.
(31) Zun-Jing, W.; Markus, D. Systematic implicit solvent coarse-graining of bilayer membranes: lipid and phase transferability of the force field *New J. Phys.* **2010**, *12*, 095004.
(32) Loverde, S. M.; Pantano, D. A.; Christian, D. A.; Mahmud, A.; Klein, M. L.; Discher, D. E. Curvature, rigidity, and pattern formation in functional polymer micelles and vesicles – From dynamic visualization to molecular simulation *Curr. Opin. Solid State Mater. Sci.* **2011**, *15*, 277-284.
(33) Piggot, T. J.; Piñeiro, Á.; Khalid, S. Molecular Dynamics Simulations of Phosphatidylcholine Membranes: A Comparative Force Field Study *J. Chem. Theory Comput.* **2012**, *8*, 4593-4609.
(34) Srivastava, A.; Voth, G. A. Hybrid Approach for Highly Coarse-Grained Lipid Bilayer Models *J. Chem. Theory Comput.* **2013**, *9*, 750-765.
(35) Arnarez, C.; Uusitalo, J. J.; Masman, M. F.; Ingólfsson, H. I.; de Jong, D. H.; Melo, M. N.; Periole, X.; de Vries, A. H.; Marrink, S. J. Dry Martini, a Coarse-Grained Force Field for Lipid Membrane Simulations with Implicit Solvent *J. Chem. Theory Comput.* **2015**, *11*, 260-275.
(36) Soares, T. A.; Vanni, S.; Milano, G.; Cascella, M. Toward Chemically Resolved Computer Simulations of Dynamics and Remodeling of Biological Membranes *J. Phys. Chem. Lett.* **2017**, *8*, 3586-3594.
(37) Ingólfsson, H. I.; Lopez, C. A.; Uusitalo, J. J.; Jong, D. H. d.; Gopal, S. M.; Periole, X.; Marrink, S. J. The power of coarse graining in biomolecular simulations *WIRES Comput. Mol. Sci.* **2014**, *4*, 225-248.
(38) Klein, M. L.; Shinoda, W. Large-Scale Molecular Dynamics Simulations of Self-Assembling Systems *Science* **2008**, *321*, 798-800.
(39) Marrink, S. J.; Mark, A. E. Molecular Dynamics Simulation of the Formation, Structure, and Dynamics of Small Phospholipid Vesicles *J. Amer. Chem. Soc.* **2003**, *125*, 15233-15242.
(40) Daoulas, K. C.; Muller, M. Single chain in mean field simulations: Quasi-instantaneous field approximation and quantitative comparison with Monte Carlo simulations *J. Chem. Phys.* **2006**, *125*, 184904.
(41) Daoulas, K. C.; Muller, M.; de Pablo, J. J.; Nealey, P. F.; Smith, G. D. Morphology of multi-component polymer systems: single chain in mean field simulation studies *Soft Matter* **2006**, *2*, 573-583.
(42) Daoulas, K. C.; Cavallo, A.; Shenhar, R.; Muller, M. Phase behaviour of quasi-block copolymers: A DFT-based Monte-Carlo study *Soft Matter* **2009**, *5*, 4499-4509.
(43) Milano, G.; Kawakatsu, T. Hybrid particle-field molecular dynamics simulations for dense polymer systems *J. Chem. Phys.* **2009**, *130*, 214106.
(44) Milano, G.; Kawakatsu, T. Pressure calculation in hybrid particle-field simulations *J. Chem. Phys.* **2010**, *133*, 214102.

(45) De Nicola, A.; Zhao, Y.; Kawakatsu, T.; Roccatano, D.; Milano, G. Hybrid Particle-Field Coarse-Grained Models for Biological Phospholipids *J. Chem. Theory Comput.* **2011**, *7*, 2947-2962.
(46) De Nicola, A.; Zhao, Y.; Kawakatsu, T.; Roccatano, D.; Milano, G. Validation of a hybrid MD-SCF coarse-grained model for DPPC in non-lamellar phases *Theor. Chem. Acc.* **2012**, *131*, 1167.
(47) Zhao, Y.; Nicola, A. D.; Kawakatsu, T.; Milano, G. Hybrid particle−field molecular dynamics simulations: Parallelization and benchmarks *J. Comput. Chem.* **2012**, *33*, 868-880.
(48) De Nicola, A.; Hezaveh, S.; Zhao, Y.; Kawakatsu, T.; Roccatano, D.; Milano, G. Micellar drug nanocarriers and biomembranes: how do they interact? *Phys. Chem. Chem. Phys.* **2014**, *16*, 5093-5105.
(49) De Nicola, A.; Kawakatsu, T.; Milano, G. Generation of Well-Relaxed All-Atom Models of Large Molecular Weight Polymer Melts: A Hybrid Particle-Continuum Approach Based on Particle-Field Molecular Dynamics Simulations *J. Chem. Theory Comput.* **2014**, *10*, 5651-5667.
(50) De Nicola, A.; Kawakatsu, T.; Rosano, C.; Celino, M.; Rocco, M.; Milano, G. Self-Assembly of Triton X-100 in Water Solutions: A Multiscale Simulation Study Linking Mesoscale to Atomistic Models *J. Chem. Theory Comput.* **2015**, *11*, 4959-4971.
(51) Sevink, G. J. A.; Schmid, F.; Kawakatsu, T.; Milano, G. Combining cell-based hydrodynamics with hybrid particle-field simulations: efficient and realistic simulation of structuring dynamics *Soft Matter* **2017**, *13*, 1594-1623.
(52) Zhu, Y.-L.; Lu, Z.-Y.; Milano, G.; Shi, A.-C.; Sun, Z.-Y. Hybrid particle-field molecular dynamics simulation for polyelectrolyte systems *Phys. Chem. Chem. Phys.* **2016**, *18*, 9799-9808.
(53) Marrink, S. J.; Risselada, H. J.; Yefimov, S.; Tieleman, D. P.; de Vries, A. H. The MARTINI force field: coarse grained model for biomolecular simulations *J. Phys. Chem. B* **2007**, *111*, 7812-7824.
(54) Pronk, S.; Páll, S.; Schulz, R.; Larsson, P.; Bjelkmar, P.; Apostolov, R.; Shirts, M. R.; Smith, J. C.; Kasson, P. M.; van der Spoel, D.; Hess, B.; Lindahl, E. GROMACS 4.5: a high-throughput and highly parallel open source molecular simulation toolkit *Bioinformatics* **2013**, *29*, 845-854.
(55) Andersen, H. C. Molecular dynamics simulations at constant pressure and/or temperature *J. Chem. Phys.* **1980**, *72*, 2384-2393.
(56) Jalili, S.; Akhavan, M. A coarse-grained molecular dynamics simulation of a sodium dodecyl sulfate micelle in aqueous solution *Colloid. Surface. A* **2009**, *352*, 99-102.
(57) Elmore, D. E. Molecular dynamics simulation of a phosphatidylglycerol membrane *FEBS Lett.* **2006**, *580*, 144-148.
(58) Zhao, W.; Róg, T.; Gurtovenko, A. A.; Vattulainen, I.; Karttunen, M. Atomic-Scale Structure and Electrostatics of Anionic Palmitoyloleoylphosphatidylglycerol Lipid Bilayers with Na+ Counterions *Biophys. J.* **2007**, *92*, 1114-1124.
(59) Dickey, A.; Faller, R. Examining the Contributions of Lipid Shape and Headgroup Charge on Bilayer Behavior *Biophys. J.* **2008**, *95*, 2636-2646.
(60) Kučerka, N.; Holland, B. W.; Gray, C. G.; Tomberli, B.; Katsaras, J. Scattering Density Profile Model of POPG Bilayers As Determined by Molecular Dynamics Simulations and Small-Angle Neutron and X-ray Scattering Experiments *J. Phys. Chem. B* **2012**, *116*, 232-239.
(61) Helfrich, W. Elastic Properties of Lipid Bilayers - Theory and Possible Experiments *Z. Naturforsch. C* **1973**, *28*, 693-703.
(62) Goetz, R.; Gompper, G.; Lipowsky, R. Mobility and elasticity of self-assembled membranes *Phys. Rev. Lett.* **1999**, *82*, 221-224.
(63) Lindahl, E.; Edholm, O. Mesoscopic undulations and thickness fluctuations in lipid bilayers from molecular dynamics simulations *Biophys. J.* **2000**, *79*, 426-433.
(64) Harmandaris, V. A.; Deserno, M. A novel method for measuring the bending rigidity of model lipid membranes by simulating tethers *J. Chem. Phys.* **2006**, *125*, 204905.
(65) Brandt, E. G.; Braun, A. R.; Sachs, J. N.; Nagle, J. F.; Edholm, O. Interpretation of Fluctuation Spectra in Lipid Bilayer Simulations *Biophys. J.* **2011**, *100*, 2104-2111.

(66) Reiss-Husson, F.; Luzzati, V. The Structure of the Micellar Solutions of Some Amphiphilic Compounds in Pure Water as Determined by Absolute Small-Angle X-Ray Scattering Techniques *J. Phys. Chem.* **1964**, *68*, 3504-3511.
(67) Christov, N. C.; Denkov, N. D.; Kralchevsky, P. A.; Ananthapadmanabhan, K. P.; Lips, A. Synergistic Sphere-to-Rod Micelle Transition in Mixed Solutions of Sodium Dodecyl Sulfate and Cocoamidopropyl Betaine *Langmuir* **2004**, *20*, 565-571.
(68) Anderson, R. L.; Bray, D. J.; Del Regno, A.; Seaton, M. A.; Ferrante, A. S.; Warren, P. B. Micelle formation in alkyl sulfate surfactants using dissipative particle dynamics *J. Chem. Theory Comput.* **2018**, *14*, 2633-2643.
(69) Jensen, G. V.; Lund, R.; Gummel, J.; Narayanan, T.; Pedersen, J. S. Monitoring the Transition from Spherical to Polymer−like Surfactant Micelles Using Small−Angle X−Ray Scattering *Angew. Chem. Int. Edit.* **2014**, *53*, 11524-11528.
(70) Rudnick, J.; Gaspari, G. The Shapes of Random Walks *Science* **1987**, *237*, 384-389.
(71) Lund, R.; Willner, L.; Monkenbusch, M.; Panine, P.; Narayanan, T.; Colmenero, J.; Richter, D. Structural Observation and Kinetic Pathway in the Formation of Polymeric Micelles *Phys. Rev. Lett.* **2009**, *102*, 188301.
(72) Wang, S.; Larson, R. G. Coarse-Grained Molecular Dynamics Simulation of Self-Assembly and Surface Adsorption of Ionic Surfactants Using an Implicit Water Model *Langmuir* **2015**, *31*, 1262-1271.
(73) Cascella, M.; Neri, M. A.; Carloni, P.; Dal Peraro, M. Topologically based multipolar reconstruction of electrostatic interactions in multiscale simulations of proteins *J. Chem. Theory Comput.* **2008**, *4*, 1378-1385.
(74) Alemani, D.; Collu, F.; Cascella, M.; Dal Peraro, M. A Nonradial Coarse-Grained Potential for Proteins Produces Naturally Stable Secondary Structure Elements *J. Chem. Theory Comput.* **2010**, *6*, 315-324.
(75) Spiga, E.; Alemani, D.; Degiacomi, M. T.; Cascella, M.; Dal Peraro, M. Electrostatic-Consistent Coarse-Grained Potentials for Molecular Simulations of Proteins *J. Chem. Theory Comput.* **2013**, *9*, 3515-3526.
(76) Bore, S. L.; Milano, G.; Cascella, M. Hybrid Particle-Field Model for Conformational Dynamics of Peptide Chains *J. Chem. Theory Comput.* **2018**, *14*, 1120-1130.

Table of Contents

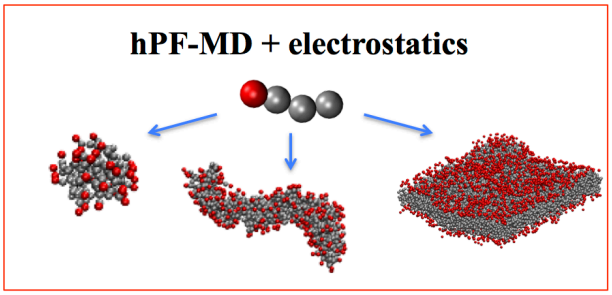

Hybrid Particle-Field Molecular Dynamics Simulations of Charged Amphiphiles in Aqueous Environment - Supporting Information

Hima Bindu Kolli,[†] Antonio de Nicola,[‡] Sigbjørn Løland Bore,[†] Ken Schäfer,[§] Gregor Diezemann,[§] Jürgen Gauss,[§] Toshihiro Kawakatsu,[‖] Zhong-Yuan Lu,[⊥] You-Liang Zhu,[#] Giuseppe Milano,[*,‡] Michele Cascella[*,†]

† Department of Chemistry and Hylleraas Centre for Quantum Molecular Sciences, University of Oslo, P.O. Box 1033 Blindern, 0315 Oslo, Norway

‡ Department of Organic Materials Science, University of Yamagata, 4-3-16 Jonan Yonezawa, Yamagata-ken 992-8510, Japan

§ Institut für Physikalische Chemie, Universität Mainz, Duesbergweg 10-14, D-55128 Mainz, Germany

‖ Department of Physics, Tohoku University, Aoba, Aramaki, Aoba-ku, Sendai 980-8578, Japan

⊥ State Key Laboratory of Supramolecular Structure and Materials, Institute of Theoretical Chemistry, Jilin University, Changchun 130023, China

State Key Laboratory of Polymer Physics and Chemistry, Changchun Institute of Applied Chemistry, Chinese Academy of Sciences, Changchun 130022, China.

** email to: gmilano@yz.yamagata-u.ac.jp, michele.cascella@kjemi.uio.no*

Table S1. Thickness (D_{HH}) of POPG bilayer from different references

System	Temp. (K)	D_{HH} (nm)
Atomistic simulations by Elmore et al.[57]	310	5.61
Atomistic simulations by Zhao et al.[58]	310	4.39
Atomistic simulations by Dickney et al.[59]	310	4.30
Experiments by Kucerka et al.[60]	303	3.73
PP-CG simulations (present work)	301	4.07
hPF-MD/e at $\varepsilon_r = 5$	301	4.71
hPF-MD/e at $\varepsilon_r = 15$	301	3.85
hPF-MD/e at $\varepsilon_r = 80$	301	3.85

Computation of undulation spectrum:

The power spectrum of undulations can be derived from for which the Helfrich continuum model. In this model, the bilayer shape can be described as a vibrating membrane *u(r)*, obtained as the sum of the surfaces of the two lipid surface layers. Any deformation mode $\tilde{u}(q)$ having wave number q can be obtained from the Fourier transform of *u(r)*. The fluctuation spectrum *S(q)* is defined as:

$$S(q) \equiv \langle |\tilde{u}(q)|^2 \rangle \cong \frac{k_b T}{a(k_c q^4)}$$

Where a is the projected area per lipid and k_c is the bending modulus. Spectra analyses reported in the main text have been performed on the last 100 ns of the hPF-MD trajectories, by fitting a grid to each monolayer with the position of each lipid, according to the procedure described by Issraelachevli[S1,S2] Two-dimensional Fourier transform of this grid have been calculated to yeld the q-space mode amplitudes, the square of which is the intensity. The average intensity per mode have been calculated by binning over wavenumbers q.

Number density

Comparison of the number density of Na+ in POPG simulations for two different values of the dielectric constant. The 0 position corresponds to the centre of the membrane, the position -2 corresponds to of the average level of the P beads. The graph shows the reduced binding of Na^+ and the dispersion into the solvent for high values of the dielectric.

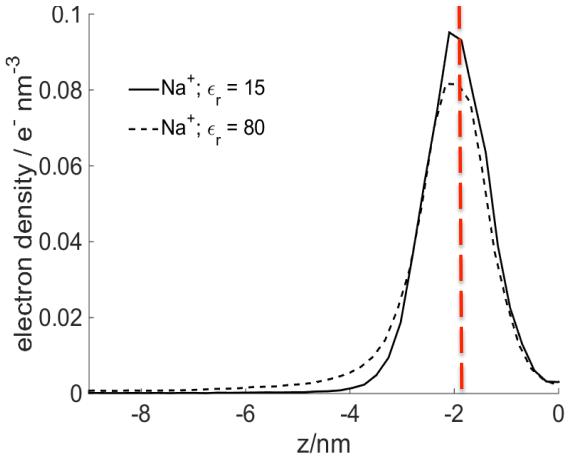

Definition of the asphericity parameter

The asphericity parameter of the micelle, characterized in terms of the invariants of a shape tensor *G* whose eigenvalues are the squares of the principal radii of gyration.

$$G_{mn} = \frac{1}{N}[\sum_i^N (\boldsymbol{r}_{mi} - R_m)(\boldsymbol{r}_{ni} - R_n)] \ \ (m, n = x, y, z) \tag{1}$$

The three eigenvalues of *G* are denoted by g_1, g_2, and g_3, *N* is the number of molecules in the aggregate and *R* is the centre of mass of the aggregate. The ratio of these three eigenvalues determines the shape of the aggregate. The definition for asphericity introduced by Rudnick and Gaspari (reference in main text) is:

$$\delta = 1 - 3\frac{\langle I_2 \rangle}{\langle I_1^2 \rangle} \tag{2}$$

where I_i are the respective invariant of the gyration tensor and is given by $I_1 = g_1 + g_2 + g_3$, $I_2 = g_1 g_2 + g_2 g_3 + g_3 g_1$, and $I_3 = g_1 g_2 g_3$. This value is bounded between zero and one. For spherical objects $\delta = 0$ and $\delta = 1$ if all the particles lie on a line.

References

S1 - Israelachveli, J. N.; Wennerström, H. Hydration or steric forces between amphiphilic surfaces? *Langmuir* **1990**, *6*, 873–876

S2 - Israelachveli, J. N.; Wennerström, H. Entropic forces between amphiphilic surfaces in liquids. *J. Phys. Chem.* **1992**, *96*, 520–531.

Paper III

Mesoscale Electrostatics Driving Particle Dynamics in Nonhomogeneous Dielectrics

Sigbjørn Løland Bore, Hima Bindu Kolli, Toshihiro Kawakatsu, Giuseppe Milano, Michele Cascella

Journal of Chemical Theory and Computation **15**, 2033 (2019)

III

Mesoscale electrostatics driving particle dynamics in non-homogeneous dielectrics

Sigbjørn Løland Bore,[†] Hima Bindu Kolli,[†,§] Toshihiro Kawakatsu,[‡] Giuseppe Milano,[¶] and Michele Cascella[*,†]

†*Department of Chemistry, and Hylleraas Centre for Quantum Molecular Sciences, University of Oslo, PO Box 1033 Blindern, 0315 Oslo, Norway*

‡*Department of Physics, Tohoku University, Aoba, Aramaki, Aoba-ku, Sendai 980-8578, Japan*

¶*Department of Organic Materials Science, Yamagata University, 4-3-16 Jonan Yonezawa, Yamagata-ken 992-8510, Japan*

§*Present address: Department of Physics and Astronomy, The University of Sheffield, United Kingdom*

E-mail: michele.cascella@kjemi.uio.no

Abstract

We introduce a density functional-based formalism to compute the electrostatic energy and forces for a mesoscopic system in the condensed phase, described with molecular resolution. The dielectric permittivity is variable in space, and it is dependent on the density fields of the individual particles present in the system. The electrostatic potential is obtained from standard numerical solutions of the generalized Poisson equation. The presence of a particle-dependent varying dielectrics produces the appearance of mesoscopic polarization forces, which are dependent on the local fluctuations of the permittivity, as well as of the electrostatic field. The proposed implementation is numerically robust, with an error on the Coulomb forces that can be systematically controlled by the mesh of spatial grid used for solving the generalized Poisson equation. We show that the method presented here is able to reproduce the concentration-dependent partitioning of an ideal salt in water/oil mixtures, in particular, reproducing the $\propto 1/\epsilon$ dependency of the partition coefficient for the free ions predicted by Born theory. Moreover, this approach reproduces the correct electrostatic features of both dipolar and charged lipid bilayers, with positive membrane and dipole potentials. The sum of both Coulomb and polarization interactions inside the membrane yields a globally repulsive potential of mean force for the ions, independently on their charge. The computational efficiency of the method makes it particularly suitable for the description of large-scale polyelectrolyte soft-matter systems.

1 Introduction

Polyelectrolytic soft matter systems are associated to a large number of important phenomena in nature, including surfactant action,[1] self-assembly of viral capsids,[2] packing of the genetic code,[3] or membrane electrochemical potentials.[4] Any computational description of polyelectrolytes is complicated by a series of factors, including the R^{-1} slowly decaying Coulomb potential, the presence of free diffusing ions and a non-homogeneous dielectric environment. These hurdles sum on the general issue that phase-separated systems appear due to selective crowding and self-assembly of the different molecular species composing the systems. This makes any computational model with molecular resolution intrinsically expensive, as the stability of such assemblies require the presence of a non-reducible number of individual components.[5]

Models comprising an all-atom resolution have benefited from years of development of efficient computer algorithms that aim for accurate and efficient computation of electrostatic forces.[6,7] This in turn has led to accurate modelling biological systems, like proteins,[8–10] lipids[11,12] or nucleic acids.[13] Nonetheless, atomistic modelling becomes computationally not feasible when addressing phenomena in the mesoscale (i.e., with size, time characteristic dimensions in the order of at least 100 nm, and milliseconds).[14,15] This is due to both the diverging number of degrees of freedom and inter-molecular interactions that need to be treated, and the relatively short integration timesteps (typically $1 - 2$ fs) imposed by the presence of fast vibrational modes.

In coarse-grained models (CG), a low-resolution representation of the molecular structure, is obtained by mapping multiple atoms into single beads.[16] This lower resolution description not only reduces the number degrees of freedom, thereby reducing computation, but also filters out high frequency modes, allowing for longer time steps. Thus, CG models offers a route to study large-scale systems while maintaining the information (albeit, at low-resolution) on the molecular structure.

Coarse-graining results in an acceleration of the dynamics, making the direct study of

time evolution and kinetics problematic. Nevertheless a variety of approaches to CG modelling,[17–22] allow us today to obtain insights on different dynamic phenomena for soft matter and biological systems, including the complex morphology of lipid membranes,[23–34] also interacting with membrane proteins[34–38] the phase behavior of surfactants ,[39,40] as well as the structural fluctuations and folding of proteins ,[17,41–51] or DNA.[52–59,59]

Nonetheless, the reduction of the degrees of freedom used to describe the molecular systems poses direct limitations in the capability of accurately describing all electrostatic features, and in particular the dielectric screening by the environment.

Through the years, several simplified methods aiming for modeling accurately electrostatics while keeping the computational advantage over atomistic approaches have been developed. Existing models can be grouped into three main categories: *(i) implicit solvent models*, which aim to describe the properties of solutes only, introducing implicitly the presence of the solvent as a background; *(ii) explicit non-polarizable solvent models*, which treat the solvent as a non-polarizable medium with specific dielectric/electrostatic properties; and *(iii) polarizable solvent models*, which introduce the dielectric response of the environment via explicit polarization.

In implicit solvent models,[60] such as Generalized Born Implicit Solvent, the screening effect of solvent molecules is modeled by representing the solute within a cavity inside a homogeneous continuum dielectric, representing the solvent. The electrostatic potential inside the cavity is then obtained by solving the generalized linearized Poisson-Boltzmann equation. Such methods can accurately model electrostatic interactions inside the bulk, but are problematic at interfaces or inside membranes. Moreover, they do not account for the entropic effects of solvent molecules.

In approaches adopting molecular mechanics-like effective CG potentials,[23] a uniform background dielectric is used to model the screening of electrostatics. This on one hand, greatly decreases computational cost due to the computation of Coulomb interactions of all the solvent molecules present in all atom simulations, but requires the calibration of

effective interactions to mimic the presence of higher-order electrostatic forces than charge-charge ones, appearing especially between charged and polar moieties. These problems are partly remedied by the model of Hess,[61] in which a salt concentration-dependent dielectrics accounts for many body effects, reproducing osmotic and coordination properties up to a 2.8 M concentration of NaCl. Nonetheless, as in implicit solvent, the use of uniform dielectric is particular poor near interfaces, making modelling of partitioning phenomena of charged species challenging.[62]

To obtain higher accuracy, solvent coarse grained models with explicit electrostatic properties have been developed.[63] The dominant approach has been to map the solvent, and in particular water, into a minimal set of bodies that mimic the existence of and environment prone to polarization by dipole orientation. From the original idea by Warshel of introducing polarizable Langevin dipoles on a grid surrounding the solute,[64] Borgis[65] proposed the use of solvating pseudoparticles carrying dipoles which are sensitive to and get polarized by the electric field of the solute. Similarly, in extended coarse-grained dipole model for water,[66] the water molecule is represented by a dipole constituted by two oppositely sites. Others recently introduced an even coarser CG mapping with four water molecules into three connected beads with opposite charges,[67] five water molecules into two charged beads,[68] or eleven water molecules into four beads in a tetrahedral arrangement, carrying each a partial charge.[69] The introduction of charges increases accuracy, but at the cost of diminishing computational gain obtained by coarse-graining.

Breaking the bottleneck of simulations of systems at molecular resolution toward the mesoscopic scale relies therefore in the definition of efficient potentials that retain the effect of a spatially variable polarizable environment without the introduction of computationally heavy electrostatic features in the solvent model.

The structural and thermodynamic properties of soft condensed systems in the mesoscale are dominated by weak interactions of order $k_\mathrm{b}T$.[70] For this reason, they can be rather accurately described by density functional based potentials in the mean-field limit.[29,71–79] In

this work, we propose a description for electrostatic interactions based on the same logic. In particular, we present a formulation of electrostatics for molecular-resolved models in the condensed phase based on the dielectric screening, the macroscopic effect of molecular polarization, rather than the molecular polarization itself. We do this by introducing a spatially resolved dielectric that depends on the local density field of the different molecular species. Our approach has the advantage of treating all the multipolar interactions that are higher in order than the direct Coulomb terms via an effective screening controlled by a smooth function, keeping the computational advantages of continuum dielectric models, and avoiding the introduction of additional degrees of freedom into the system, thus offering optimal computational performance.

2 Electrostatics in a dense molecular system

2.1 Electrostatic energy and forces

In a dense system, the total electrostatic interaction energy is expressed by the formula:[80,81]

$$W_{\text{elec}}[\{\phi(\mathbf{r})\}] = \frac{1}{2}\int \mathrm{d}\mathbf{r}\frac{\mathbf{D}(\mathbf{r})\cdot\mathbf{D}(\mathbf{r})}{\epsilon(\mathbf{r})}, \tag{1}$$

where $\mathbf{D}(\mathbf{r})$, $\epsilon(\mathbf{r})$ are the electrostatic displacement field and the dielectric function,each dependent on the set of number densities $\{\phi(\mathbf{r})\}$ of all particle species (including solvent and ions). The displacement field is particularly useful in the context of non-homogeneous dielectrics because its governing equation, the Maxwell equation for the displacement field, only involves free charges and not polarized charges.

Considering now the case of a molecular system composed by M species $\{\phi(\mathbf{r})\} = \{\phi_1, ..., \phi_k, ..., \phi_M\}$ for each k type. The mean-field potential felt by a particle of type k

at point $\mathbf{r}$, is derived through the saddle point approximation[82] as the functional derivative

$$V_{\text{ext},k}(\mathbf{r}) = \frac{\delta W_{\text{elec}}}{\delta \phi_k(\mathbf{r})}, \tag{2}$$

which involves two terms, dependent on $\mathbf{D}(\mathbf{r})$ and $\epsilon(\mathbf{r})$:

$$V_{\text{ext},k}(\mathbf{r}) = \int \mathrm{d}\mathbf{r}' \left(\frac{\delta W_{\text{elec}}}{\delta \mathbf{D}(\mathbf{r}')} \frac{\delta \mathbf{D}(\mathbf{r}')}{\delta \phi_k(\mathbf{r})} + \frac{\delta W_{\text{elec}}}{\delta \epsilon(\mathbf{r}')} \frac{\delta \epsilon(\mathbf{r}')}{\delta \phi_k(\mathbf{r})} \right). \tag{3}$$

Computing explicitly the two functional derivatives (SI 1 for detailed derivation), we obtain the mean-field potential experienced by a particle of type k as:

$$V_{\text{ext},k}(\mathbf{r}) = q_k \psi(\mathbf{r}) - \frac{1}{2} \frac{\partial \epsilon(\mathbf{r})}{\partial \phi_k(\mathbf{r})} |\mathbf{E}(\mathbf{r})|^2, \tag{4}$$

where the first term of the integrand in equation (3) yields the potential energy felt by a charged particle q_k in the electrostatic potential of the system $\psi(\mathbf{r})$, and the second term of the integrand in equation (3) defines the potential energy due to the polarization of the medium.

$$\mathbf{D}(\mathbf{r}) = -\epsilon(\mathbf{r}) \boldsymbol{\nabla} \psi(\mathbf{r}) = \epsilon(\mathbf{r}) \mathbf{E}(\mathbf{r}). \tag{5}$$

The corresponding force acting on a particle k positioned at $\mathbf{r}$ is straightforwardly obtained by the spatial derivative of the potential energy in equation (4):

$$\mathbf{F}_k(\mathbf{r}) = q_k \mathbf{E}(\mathbf{r}) + \frac{1}{2} \boldsymbol{\nabla} \left(\frac{\partial \epsilon(\mathbf{r})}{\partial \phi_k(\mathbf{r})} |\mathbf{E}(\mathbf{r})|^2 \right). \tag{6}$$

From the force on the different particles, it is possible to define the force density (force per unit volume) acting on a volume element placed at $\mathbf{r}$. In particular, the force density due to the polarization of the medium is:

$$\mathbf{f}_{\text{pol}}(\mathbf{r}) \equiv \sum_k^M \phi_k(\mathbf{r}) \frac{1}{2} \boldsymbol{\nabla} \left(\frac{\partial \epsilon(\mathbf{r})}{\partial \phi_k(\mathbf{r})} |\mathbf{E}(\mathbf{r})|^2 \right), \tag{7}$$

which is equivalent to the polarization part of the Helmholtz force density defined in a continuous medium[83] (see SI 2):

$$\mathbf{f}_{\text{pol}}(\mathbf{r}) = \frac{1}{2}\boldsymbol{\nabla}\left(\sum_{k}^{M}\phi_k(\mathbf{r})\frac{\partial\epsilon(\mathbf{r})}{\partial\phi_k}|\mathbf{E}(\mathbf{r})|^2\right) - \frac{1}{2}\boldsymbol{\nabla}\epsilon(\mathbf{r})|\mathbf{E}(\mathbf{r})|^2. \tag{8}$$

The explicit formulation of the polarization term in equation (4) depends on the modeling of the functional dependence of $\epsilon(\mathbf{r})$ on the particle densities $\{\phi(\mathbf{r})\}$. Various types of modelling exist; for example, in Levy et al.[84] the local dielectrics has been assumed to depend on the ion density. Here, we model such relationship by a weighted average of the dielectric constants for each species k present in r, similarly to what proposed in refs:[85–87]

$$\epsilon(\{\phi(\mathbf{r})\}) = \frac{\sum_k^M \epsilon_k\phi_k(\mathbf{r})}{\phi_0(\mathbf{r})}, \tag{9}$$

where $\phi_0(\mathbf{r})$ is the sum of all particle densities: $\phi_0(\mathbf{r}) = \sum_k \phi_k(\mathbf{r})$. Assuming equation (9), equation (4) becomes:

$$V_{\text{ext},k}(\mathbf{r}) = q_k\psi(\mathbf{r}) - \frac{1}{2}\frac{\epsilon_k - \epsilon(\mathbf{r})}{\phi_0(\mathbf{r})}|\mathbf{E}(\mathbf{r})|^2, \tag{10}$$

and the corresponding force on a particle positioned at $\mathbf{r}$:

$$\mathbf{F}_k(\mathbf{r}) = q_k\mathbf{E}(\mathbf{r}_i) + \frac{1}{2}\boldsymbol{\nabla}\left(\frac{\epsilon_k - \epsilon(\mathbf{r})}{\phi_0(\mathbf{r})}|\mathbf{E}(\mathbf{r})|^2\right). \tag{11}$$

The polarization component of the force on the particle is thus formed by two contributions:

$$\mathbf{F}_{k,\text{pol}}(\mathbf{r}) = -\frac{1}{2}\boldsymbol{\nabla}\epsilon(\mathbf{r})\left(\frac{|\mathbf{E}(\mathbf{r})|^2}{\phi_0(\mathbf{r})}\right) + \frac{1}{2}(\epsilon_k - \epsilon(\mathbf{r}))\boldsymbol{\nabla}\left(\frac{|\mathbf{E}(\mathbf{r})|^2}{\phi_0(\mathbf{r})}\right), \tag{12}$$

Assuming homogeneous density ($\phi_0(\mathbf{r}) = \tilde{\phi}_0$), the polarization force can be interpreted as follows. The first term corresponds to a force acting on all particles that, in the presence of an external electrostatic field, seeks to homogenize the spatial distribution of the dielectrics.

The second term tends to separate the dielectric, attracting the more polar particles (and repelling the less polar ones) towards the regions of the space characterized by a stronger electrostatic field.

2.2 Numerical solution for $\psi(\mathbf{r})$

The computation of forces through equation (11), requires the electrostatic potential $\psi(\mathbf{r})$ and is obtained by solving the *generalized Poisson equation* (GPE):

$$\boldsymbol{\nabla} \cdot (\epsilon(\mathbf{r}) \boldsymbol{\nabla} \psi(\mathbf{r})) = -\rho(\mathbf{r}). \tag{13}$$

In the context of molecular dynamics, the GPE is a linear equation as $\epsilon(\mathbf{r})$ and $\rho(\mathbf{r})$ are predetermined by particle densities. Numerous methods exist for solving the linear GPE.[88] We employ a finite difference scheme (which has been used in MD with implicit solvent,[89] or in the reaction field method[90]) on regular grid and solve the linear system of equations iteratively using the Successive over relaxation method.[91] For typical grids (∼0.6-8 nm) and potential update times ($\delta t \simeq 0.3$ ps) used in hPF calculations, the routine spends only 10% of the total simulation time even using an overly tight convergence criterion for the electrostatic potential (average change per iteration lower than 10^{-6} mV). By loosening the criterion of convergence by one order of magnitude (10^{-5} mV), the time spent by the same routine drops to 3% of total time. More details on details on the procedure are provided in SI 3.

2.3 Implementation within the hybrid particle-field molecular dynamics approach

In this study, we tested the present formulation for electrostatic interactions in combination with the hybrid particle field (hPF) method coupled to molecular dynamics.[82] In this approach, a molecular system is described by a coarse grained representation for both the solute and the solvent. The intermolecular forces are not computed by direct many-body interac-

tion terms. On the contrary, each independent particles is coupled to a density-dependent interaction energy energy functional W. The total energy of the system is written as:

$$H = H_0(\{\mathbf{r}\}) + W[\{\phi\}]. \tag{14}$$

Here, $H_0(\{\mathbf{r}\})$ is the intramolecular Hamiltonian of non-interacting chains that is dependent on the set of particle positions $\{\mathbf{r}\}$. $W[\{\phi\}]$ is an interaction term built so that the partition function of the non-interacting system that is being simulated reproduces the correct partition function of the target interacting one.[82] Here, we split the interaction energy functional into two parts:

$$W = W_{\text{non-elec}} + W_{\text{elec}}, \tag{15}$$

where the electrostatic interaction energy has already been described. The non-electrostatic interaction can be modelled in multiple ways. As in previous publications,[82] here we use:

$$W_{\text{non-elec}}\left[\{\phi\}\right] = \frac{1}{\tilde{\phi}_0}\int \mathrm{d}\mathbf{r}\left[\frac{k_\mathrm{b}T}{2}\sum_{k,\ell}\chi_{k\ell}\phi_k(\mathbf{r})\phi_\ell(\mathbf{r}) \; + \frac{1}{2\kappa}\left(\sum_k \phi_k(\mathbf{r}) - \tilde{\phi}_0\right)^2\right], \tag{16}$$

where $\chi_{k\ell}$ is the mean field coupling term between particles of type k and ℓ, κ is the compressibility constant controlling local fluctuations of densities in the system, and $\tilde{\phi}_0$ is the average number density of the whole system. The particle densities $\phi_k(\mathbf{r})$ for the different species k are obtained from the individual particle positions distributing over a grid.[82] The external potential felt by a particle of type k at position $\mathbf{r}$ is obtained, as in equation (2), by the saddle point approximation:

$$V_{\text{ext},k}(\mathbf{r}) = \frac{\delta W_{\text{non-elec}}}{\delta\phi_k(\mathbf{r})} = \frac{1}{\tilde{\phi}_0}\left[k_\mathrm{b}T\sum_l \chi_{k\ell}\phi_\ell(\mathbf{r}) + \frac{1}{\kappa}\left(\sum_\ell \phi_\ell(\mathbf{r}) - \tilde{\phi}_0\right)\right]. \tag{17}$$

The corresponding force acting on a particle of type k positioned at $\mathbf{r}$ is obtained by the spatial derivative of $V_{\mathrm{ext},k}$:

$$\mathbf{F}_{\mathrm{ext},k}(\mathbf{r}) = -\frac{1}{\tilde{\phi}_0}\left[\sum_{\ell}\left(k_{\mathrm{b}}T\chi_{k\ell} + \frac{1}{\kappa}\right)\boldsymbol{\nabla}\phi_{\ell}(\mathbf{r})\right]. \tag{18}$$

The density gradients are numerically computed on the grid, obtaining the forces for each individual particle by linear interpolation of the nearest grid points (for a detailed description, see ref:[82]).

Having a direct definition of the forces acting on the particles from equation (18), the time-evolution of the system can be computed by numerical integration of the equations of motion using standard molecular dynamics algorithms.

The method here introduced was implemented in the OCCAM hybrid particle field molecular dynamics software.[92] Next, we present three examples to benchmark the performance of the presented scheme for electrostatics coupled to hybrid particle-field molecular dynamics (hPF-MD/e hereafter).

2.4 Benchmarking of the implementation

We verified the accuracy on the calculation of the forces for a simple model system composed of two oppositely unit charged particles placed in a large box ($20 \times 20 \times 20\,\mathrm{nm}^3$) separated by a distance d under uniform dielectric $\epsilon_r = 1$. Figure 1 reports benchmarking of the accuracy (Top and middle panels). The force between two charges shows an excellent agreement with theoretical Coulomb force. For inter-particle distance approaching the grid size, the force gores towards zero. This is due to having distributed charges and not point particles. The primary determining factor of accuracy is the grid size b used for solving the GPE. The inset panel shows how the relative error of the computed force depends on the grid resolution b. The electrostatic forces can be systematically improved by increasing the grid mesh to the required precision (Figure 1). Already, using a grid size between 0.6 and 0.7 nm,

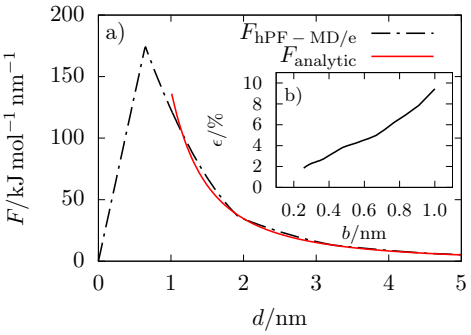

Figure 1: Benchmark on Coulomb interactions with hPF-MD/e. The main plot (panel a) reports the intensity of the forces acting on two charged particles of opposite signs as a function of the relative distance computed numerically by hPF-MD/e, $F_{\mathrm{hPF-MD/e}}$ for a grid of 0.65 nm compared to the analytic values, F_{analytic}. The inset (panel b) presents the mean relative error in the 1-5 nm range as a function of grid size b.

good accuracy is obtained. It is worth noting that, a similar grid size has been prescribed to correctly describe several non charged systems by using a density field description for non-charged matter systems by hPF-MD.[24,93]

3 Results and discussion

3.1 Partitioning of ions in a bi-phase system

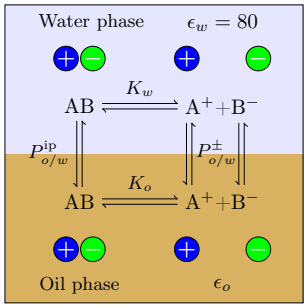

Figure 2: Partitioning and dissociation equilibria for an ideal ion couple A^+B^- in a binary phase-separated liquid composed of oil and water.

As a first test, we investigated the ability of our model to reproduce the behavior of an ideal monovalent binary salt A^+B^- dissolved in a bi-phase solution composed by water, characterized by a dielectric $\epsilon_w = 80$, and an oil of dielectric $\epsilon_o \leq \epsilon_w$. The salt species are expected to distribute between the two solvents according the chemical equilibria shown in Figure 2, which include the thermodynamic dissociation constants K_w and K_o in the water and the oil phases, and the partition coefficients $P^{ip}_{o/w}$ and $P^{\pm}_{o/w}$ for the ion couples and for the free ions, respectively. Here we assume that, for ideal ions, the partition coefficients of the positive and negative free ions are identical. The distribution coefficient, which is the most easily attainable quantity in experiments,[94] measures the total partitioning of the salt, irrespective of its protolytic state, and it is given by:

$$D_{o/w} = \frac{c_o}{c_w}, \tag{19}$$

where c_o and c_w are the total concentrations of salt [AB]+[A+], where [A+] accounts for the concentration of salt present in an ionized form, in oil and water respectively. Contrary to the individual equilibrium constants (K_w, K_o, $P^{ip}_{o/w}$, $P^{\pm}_{o/w}$), $D_{o/w}$ is dependent on the nominal salt concentration in the whole system c. Considering the stationary state concentrations of the various chemical species are bound to the coexisting chemical equilibria as depicted in Figure 2, it is possible to derive an exact relationship for $D_{o/w}$, dependent on the various equilibrium constants, and c (see ref.[94]) for a full derivation):

$$D_{o/w} = \frac{P^{\mathrm{ip}}_{o/w} + \alpha(P^{\pm}_{o/w} - P^{\mathrm{ip}}_{o/w})}{1 + \alpha(P^{\mathrm{ip}}_{o/w} - P^{\pm}_{o/w})}, \tag{20}$$

where

$$\alpha = \frac{-A + \sqrt{A^2 + 4A(1 + P^{\mathrm{ip}}_{o/w})c}}{2(1 + P^{\mathrm{ip}}_{o/w})(1 + P^{\pm}_{o/w})c}, \tag{21}$$

and

$$A = K_w(1 + P^{\pm}_{o/w})^2. \tag{22}$$

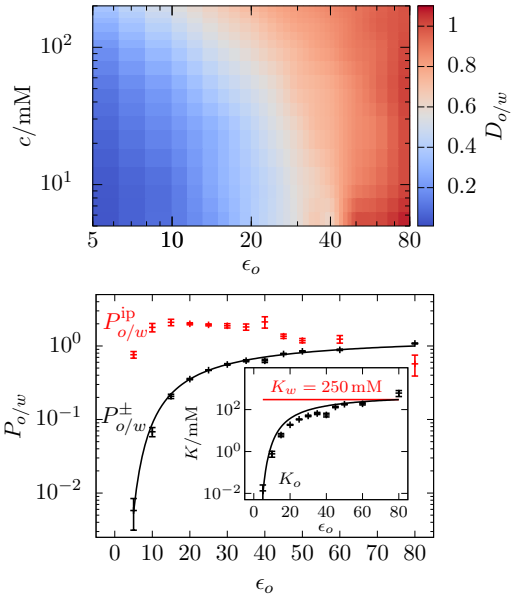

Figure 3: Partition coefficient and dissociation constants for an ideal salt in an oil/water mixture from hPF-MD/e. (Top) Distribution coefficient $D_{o/w}$ as function of the total salt concentration at different values of the dielectric constant for the oil ϵ_o. (Bottom) Partition coefficients of unpaired ions and paired ions, obtained by fitting equation (20) on the data in the top graph. The black line is obtained by fitting γ in equation (23) from data points of $P^{\pm}_{o/w}$. (Bottom inset) Dissociation constants of the ion pair in water and oil. The continuous black line is the prediction obtained from equation (25), using γ obtained from fitting (23) and assuming $P^{\mathrm{ip}}_{o/w} = 1$.

Figure 3 reports $D_{o/w}$ obtained from hPF-MD/e simulations for different concentrations c and values of ϵ_o (simulation details in SI 4.1). In agreement with equation (20), by increasing the total salt concentration we observe a decrease in the partitioning between the two phases. The concentration-independent constants can be extrapolated by fitting equation (20) against c. Figure 3 also reports the corresponding equilibrium constants for a range of dielectric values obtained by our fitting. In particular, Born theory predicts

$$\log P^{\pm}_{o/w} = \gamma \left(\frac{1}{\epsilon_w} - \frac{1}{\epsilon_o} \right), \tag{23}$$

where

$$\gamma \equiv \frac{e^2}{8\pi\epsilon_0 k_\mathrm{b} T \ln(10) r_0}. \tag{24}$$

Here r_0, the ionic radius, is dependent on the type of the ion. Fitting γ to the $P^{\pm}_{o/w}$ values obtained with hPF-MD/e, we find an excellent correspondence with the hyperbolic ϵ_o dependence predicted by Born theory. The fitted value of $\gamma = 12.15$ corresponds to an ionic radius of $r_0 \approx 1.0\,\mathrm{nm}$, which is in the order of the spread of the charge on the density grid. It should be noted that the Born expression is an approximate relation which assumes homogeneous dielectric, and that it ignores important effects around the ion, such as dielectric saturation and electrostriction.[87]

$P^{\mathrm{ip}}_{o/w}$, the partition coefficient for the ion pairs, takes values near 1, and varies little with ϵ_o. This is due to the fact that the ion pairs, having a zero net charge, are not affected as much as the free ions by the difference in the dielectric between the two media. The ion dissociation K_o is determined by the thermodynamic cycle in Figure 2:[95]

$$\log K_o = \log K_w - \log P^{\mathrm{ip}} + 2\gamma \left(\frac{1}{\epsilon_w} - \frac{1}{\epsilon_o} \right), \tag{25}$$

which is also in good agreement with the data from the hPF/e simulations.

3.2 Ion permeation in charged and polar membranes

After having verified the correct behavior of the bulk charge distribution in two liquids, we now consider the simulation of a concentration of 100 mM of ideal salt in the presence of model membranes. Specifically we take into consideration the two cases of *(i)* a dipolar lipid bilayer of palmitoyloleoyl phosphatidylcholine (POPC), and *(ii)* a negatively-charged membrane consisting of palmitoyloleoyl phosphatidylglycerol (POPG). The lipid molecules are represented using a coarse-grained mapping analogous to that of the Martini CG force-field,[23] as presented in previous works,[96] restraining the lipids to an ideal packing structure. This is done to provide optimal comparison for the different systems, as differences in the

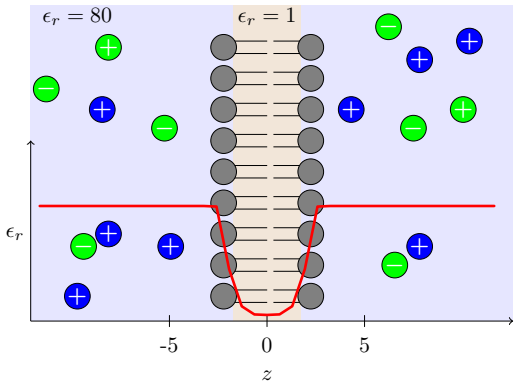

Figure 4: Scheme of the structure of the constituted lipid bilayers. The indigo region is occupied by the hydrophobic lipid tails, the gray spheres represent the polar or charged lipid heads. Ions distribute in the surrounding water. Water is not shown for clarity. The red plot reports the average dielectric value along normal axis of the lipid bilayer, as obtained from equation (9).

observed results are necessarily due to the different electrostatic treatment only. Details on the system setup are provided in SI 4.2.

In a first set of simulations, a uniform dielectric value was assigned to all beads. In particular, we tested both a uniform value of $\epsilon_{80} \equiv 80$, corresponding to the relative dielectric constant of water, as well as $\epsilon_{15} \equiv 15$ which is a commonly used value in the literature in CG studies on constituted lipid bilayers.[23] In a second set of simulations, water and ions were assigned a dielectric $\epsilon_r = 80$, while a low dielectric value ($\epsilon_r = 1$) was used for the lipids ($\epsilon_{1,80}$).

As depicted in Figure 5, the electrostatic potentials obtained for both the uniform and varying dielectric conditions contain the expected key features of charged and zwitterionic membranes. In particular, the potentials always feature a global minimum at the quota of the negatively charged phosphorous, the dipole potential (the electrostatic potential at the midpoint of the membrane) features a local maximum, and the surface potential (the potential difference between the bulk and the membrane) is positive. The intensity of the surface potential obtained for charged membranes is consistent with past Poisson-Boltzmann

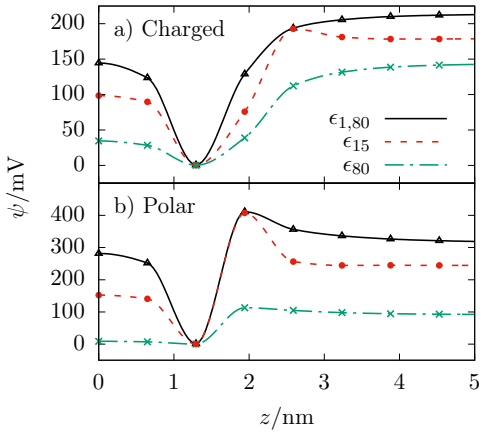

Figure 5: Average electrostatic potential ψ along the normal axis to the membrane z from its midpoint. The graph reports values of ψ obtained for the charged (panel a) and polar membranes (panel b), using varying ($\epsilon_{1,80}$) or constant values ($\epsilon_{15}, \epsilon_{80}$) of the dielectric.

calculations (in the order of 100-200 mV).[97] We observe that for both systems, the use of a varying dielectric produces systematically higher values for both the dipole and the surface potentials. In particular, in Zwitterionic membranes the dipole potential raises up too $\sim$300 mV, falling within the experimentally observed range of $200 - 1000$ mV.[98]

The polarization forces acting on the individual particles are about two orders of magnitude weaker than the Coulomb ones (for the charged lipid bilayer $\langle|\mathbf{F}_{\text{pol}}|\rangle = 0.07\,\text{kJ mol}^{-1}\,\text{nm}^{-1}$ and $\langle|\mathbf{F}_{\text{Coul}}|\rangle = 6.92$ kJ mol^{-1}nm^{-1}). Nonetheless, as they act on the totality of the particles present in the system, they contribute to the σ_{zz} component of the stress tensor with a comparable magnitude to the one of the Coulomb term (Figure 6). As also previously reported,[99] the contribution to the stress profile due to the electrostatic forces in the presence of a constant dielectric is reduced to a peak at the quota of the polar/charged heads. On the contrary, in the presence of variable dielectric, the Coulomb and polarization forces contribute differently to the stress, also depending on the electrostatic nature of the lipid head yielding an inner value different from the one at the solvent quota.

Figure 7 reports the statistical distribution of the positive and negative ions as a function

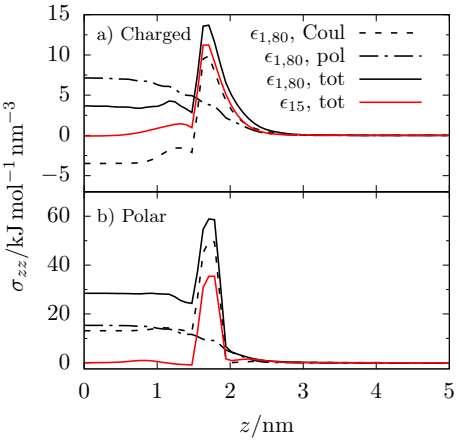

Figure 6: Contributions to the stress tensor σ_{zz} along the normal axis z using a uniform and nonuniform dielectric (ϵ_{15} and $\epsilon_{1,80}$) for a charged (panel a) and a polar membrane (panel b). The origin of the z axis is set at the midpoint of the membrane.

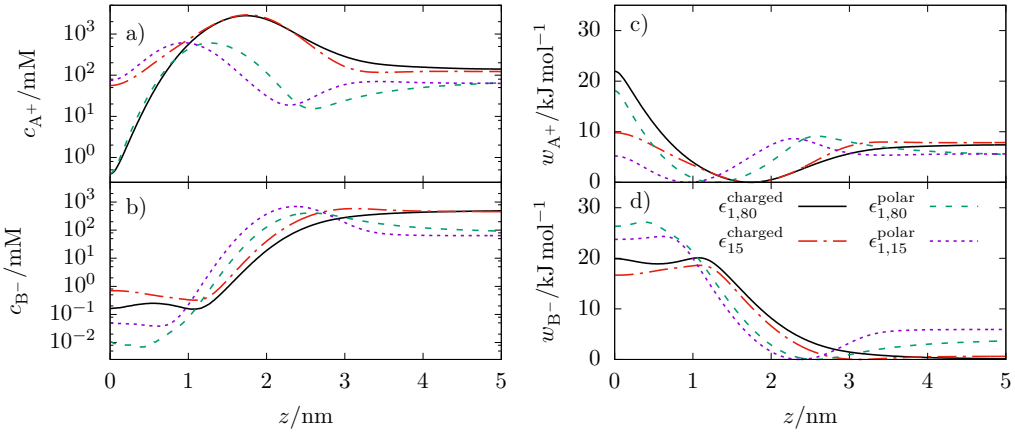

Figure 7: (Panels a, b) Concentrations c and (Panels c, d) corresponding potentials of mean force w for both the positive and negative ions A^+, B^- as a function of the normal axis z from the membrane midpoint. The graphics report values for both the charged and polar membranes, using different modelling of the dielectric.

of z, which results from the combined effect of both the Coulomb and polarization force contributions. In the presence of a zwitterionic dipolar head, the use of a constant dielectric systematically produces a rather flat potential of mean force (PMF) for the positive ions, which can almost freely diffuse through the membrane. On the contrary, the permeation in a varying dielectric environment is hindered, with a concentration of positive charges inside the membrane two orders of magnitude lower than in the bulk solvent. The permeation of the negative ions is strongly influenced by the surface potential, which for all dielectric values, is high enough to keep negatively charged ions away from the membrane and out in the bulk. The distribution of the ions in the system depends on the combined action of both the electrostatic and the polarization forces. Remarkably, only the use of a varying dielectric produces a significant increase of the potential of mean force w for both the positive and negative ions inside the membranes, which is consistent with an expected low ion permeation through the bilayer. On the contrary, the use of a constant dielectric is less capable of producing a partitioning between the aqueous and lipid phases, regardless of the dielectric value. In particular, we observe a systematic underestimation of w for the positive ions, and a consequent excessive diffusion of the same ions into the lipid bilayer.

4 Conclusion

The development of a density field-mediated particle potential for electrostatics allows a computationally inexpensive treatment of electrostatic interactions which is able to take into account the spatial distribution of individual particles producing a non-homogeneous dielectric screening. In particular, the present model describes the effect of polarization into the motion of the individual particles composing the system without the need of treating this term via additional degrees of freedom like charge-resolved solvent models, Drude-polarization charges or induced dipoles.[65,67,68] Our tests show how this model describes well the mesoscopic behaviour of ideal ions in the presence of phase-separated solvents, or at

water/lipid interfaces. In the latter case, the model is able to predict the appearance of membrane potentials that prevent both positive and negative ions from diffusing through it. This is a result that is not easily attainable in the absence of a spatially-varying dielectric, in which case reproducing the correct ion permeation requires the introduction of additional non-electrostatic effective potentials acting between the ions and the membrane or the solvent. The combined effect of the Coulomb and polarization forces produce a more complex stress profile along the normal axis of a lipid bilayer, which is absent when using a constant effective dielectric background. The appearance of such features in the stress profile implies the presence of additional physical features into the systems, which can be exploited in future calibrations of lipids and surfactants with improved structural properties like the average area-per-head or the lateral diffusion in self-assembled structures such as micelles or vesicles.

In this work, we restricted our analysis to systems containing ideal ions. This choice was done to determine with clarity what features are directly captured by the proposed electrostatic model. In fact, the description of the chemical variability of different species can be straightforwardly included by other non-electrostatic terms of the potential, for example by the standard hPF functionals described so far in the literature.[82,100–102]

In this perspective, the proposed model provides an excellent route toward an improved description of very large and complex polyelectrolytic multi-phase systems like those found in biological environments, consistently with the definition of hPF-consistent CG models for bio-polymers where the electrostatic features are explicitly taken into account.[51]

Acknowledgement

Authors acknowledge the support of the Norwegian Research Council through the CoE Hylleraas Centre for Quantum Molecular Sciences (Grant n. 262695), and by the Norwegian Supercomputing Program (NOTUR) (Grant No. NN4654K). HBK received funding

from the European Union Horizon 2020 research and innovation program under the Marie Skłodowska-Curie grant agreement No 704491.

Supporting Information Available

Full derivation of the polarization forces, documentatition on numerical solver for the GPE, and system setup for ion parititioning and ion/membrane simulations.

References

(1) Phillips, J. The energetics of micelle formation. *T. Faraday Soc.* **1955**, *51*, 561–569, DOI: 10.1039/tf9555100561.

(2) Chevreuil, M.; Law-Hine, D.; Chen, J.; Bressanelli, S.; Combet, S.; Constantin, D.; Degrouard, J.; Möller, J.; Zeghal, M.; Tresset, G. Nonequilibrium self-assembly dynamics of icosahedral viral capsids packaging genome or polyelectrolyte. *Nat. Commun.* **2018**, *9*, 3071, DOI: 10.1038/s41467-018-05426-8.

(3) Schiessel, H. The physics of chromatin. *J. Phys.: Condens. Matter* **2003**, *15*, R699, DOI: 10.1088/0953-8984/15/19/203.

(4) Cevc, G. Membrane electrostatics. *Biochim. Biophys. Acta, Rev. Biomembr.* **1990**, *1031*, 311–382, DOI: 10.1016/0304-4157(90)90015-5.

(5) Jacobson, K.; Mouritsen, O. G.; Anderson, R. G. Lipid rafts: at a crossroad between cell biology and physics. *Nat. Cell Biol.* **2007**, *9*, 7, DOI: 10.1038/ncb0107-7.

(6) Davis, M. E.; McCammon, J. A. Electrostatics in biomolecular structure and dynamics. *Chem. Rev.* **1990**, *90*, 509–521, DOI: 10.1021/cr00101a005.

(7) Sagui, C.; Darden, T. A. MOLECULAR DYNAMICS SIMULATIONS OF BIOMOLECULES: Long-Range Electrostatic Effects. *Annu. Rev. Bioph. Biom.* **1999**, *28*, 155–179, DOI: 10.1146/annurev.biophys.28.1.155.

(8) Vlachakis, D.; Bencurova, E.; Papangelopoulos, N.; Kossida, S. *Adv. Protein Chem. Struct. Biol.*; Elsevier, 2014; Vol. 94; pp 269–313, DOI: 10.1016/b978-0-12-800168-4.00007-x.

(9) Karplus, M.; Kuriyan, J. Molecular dynamics and protein function. *Proc. Natl. Acad. Sci. U. S. A.* **2005**, *102*, 6679–6685, DOI: 10.1073/pnas.0408930102.

(10) Hospital, A.; Goñi, J. R.; Orozco, M.; Gelpí, J. L. Molecular dynamics simulations: advances and applications. *Adv. Appl. Bioinf. Chem.* **2015**, *8*, 37, DOI: 10.2147/aabc.s70333.

(11) Lindahl, E.; Edholm, O. Mesoscopic undulations and thickness fluctuations in lipid bilayers from molecular dynamics simulations. *Biophys. J.* **2000**, *79*, 426–433, DOI: 10.1016/s0006-3495(00)76304-1.

(12) Feller, S. E. Molecular dynamics simulations of lipid bilayers. *Curr. Opin. Colloid Interface Sci.* **2000**, *5*, 217–223, DOI: 10.1016/S1359-0294(00)00058-3.

(13) Ivani, I.; Dans, P. D.; Noy, A.; Perez, A.; Faustino, I.; Hospital, A.; Walther, J.; Andrio, P.; Gon, R.; Balaceanu, A.; Portella, G.; Battistini, F.; Gelpi, J. L.; Gonzalez, C.; Vendruscolo, M.; Laughton, C. A.; Harris, S. A.; Case, D. A.; Orozco, M. Parmbsc1: a refined force field for DNA simulations. *Nat. Methods* **2016**, *13*, 55–58, DOI: 10.1038/nmeth.3658.

(14) Klein, M. L.; Shinoda, W. Large-Scale Molecular Dynamics Simulations of Self-Assembling Systems. *Science* **2008**, *321*, 798–800, DOI: 10.1126/science.1157834.

(15) Cascella, M.; Vanni, S. Toward accurate coarse-graining approaches for protein and membrane simulations. *Chem. Modell.* **2015**, *12*, 1, DOI: 10.1039/9781782622703-00001.

(16) Voth, G. A. *Coarse-graining of condensed phase and biomolecular systems*; CRC press, 2008.

(17) Levitt, M.; Warshel, A. Computer simulation of protein folding. *Nature* **1975**, *253*, 694, DOI: 10.1038/253694a0.

(18) Tirion, M. M. Large Amplitude Elastic Motions in Proteins from a Single-Parameter, Atomic Analysis. *Phys. Rev. Lett.* **1996**, *77*, 1905–1908, DOI: 10.1103/PhysRevLett.77.1905.

(19) Groot, R. D.; Warren, P. B. Dissipative particle dynamics: Bridging the gap between atomistic and mesoscopic simulation. *J. Chem. Phys.* **1997**, *107*, 4423–4435, DOI: 10.1063/1.474784.

(20) Ercolessi, F.; Adams, J. B. Interatomic potentials from first-principles calculations: the force-matching method. *EPL (Europhysics Letters)* **1994**, *26*, 583, DOI: 10.1209/0295-5075/26/8/005.

(21) Izvekov, S.; Parrinello, M.; Burnham, C. J.; Voth, G. A. Effective force fields for condensed phase systems from ab initio molecular dynamics simulation: A new method for force-matching. *J. Chem. Phys.* **2004**, *120*, 10896–10913, DOI: 10.1063/1.1739396.

(22) Reith, D.; Pütz, M.; Müller-Plathe, F. Deriving effective mesoscale potentials from atomistic simulations. *J. Comput. Chem.* **2003**, *24*, 1624–1636, DOI: 10.1002/jcc.10307.

(23) Marrink, S. J.; Risselada, H. J.; Yefimov, S.; Tieleman, D. P.; De Vries, A. H. The

MARTINI force field: coarse grained model for biomolecular simulations. *J. Phys. Chem. B* **2007**, *111*, 7812–7824, DOI: 10.1021/jp071097f.

(24) De Nicola, A.; Zhao, Y.; Kawakatsu, T.; Roccatano, D.; Milano, G. Hybrid particle-field coarse-grained models for biological phospholipids. *J. Chem. Theory Comput.* **2011**, *7*, 2947–2962, DOI: 10.1021/ct200132n.

(25) Sharma, S.; Kim, B. N.; Stansfeld, P. J.; Sansom, M. S. P.; Lindau, M. A Coarse Grained Model for a Lipid Membrane with Physiological Composition and Leaflet Asymmetry. *PLoS One* **2015**, *10*, 1–21, DOI: 10.1371/journal.pone.0144814.

(26) Shinoda, W.; DeVane, R.; Klein, M. L. Zwitterionic lipid assemblies: molecular dynamics studies of monolayers, bilayers, and vesicles using a new coarse grain force field. *J. Phys. Chem. B* **2010**, *114*, 6836–6849, DOI: 10.1021/jp9107206.

(27) Orsi, M.; Essex, J. W. The ELBA force field for coarse-grain modeling of lipid membranes. *PLoS One* **2011**, *6*, e28637, DOI: 10.1371/journal.pone.0028637.

(28) Deserno, M.; Kremer, K.; Paulsen, H.; Peter, C.; Schmid, F. *From Single Molecules to Nanoscopically Structured Materials*; Springer, 2013; pp 237–283, DOI: 10.1007/12_2013_258.

(29) Müller, M.; Katsov, K.; Schick, M. Biological and synthetic membranes: What can be learned from a coarse-grained description? *Phys. Rep.* **2006**, *434*, 113–176, DOI: 10.1016/j.physrep.2006.08.003.

(30) Marrink, S. J.; Mark, A. E. The mechanism of vesicle fusion as revealed by molecular dynamics simulations. *J. Am. Chem. Soc.* **2003**, *125*, 11144–11145, DOI: 10.1021/ja036138+.

(31) Risselada, H. J.; Marrink, S. J. Curvature effects on lipid packing and dynamics in

liposomes revealed by coarse grained molecular dynamics simulations. *Phys. Chem. Chem. Phys.* **2009**, *11*, 2056–2067, DOI: 10.1039/b818782g.

(32) Diggins IV, P.; McDargh, Z. A.; Deserno, M. Curvature softening and negative compressibility of gel-phase lipid membranes. *J. Am. Chem. Soc.* **2015**, *137*, 12752–12755, DOI: 10.1021/jacs.5b06800.

(33) Gardner, J. M.; Deserno, M.; Abrams, C. F. Effect of intrinsic curvature and edge tension on the stability of binary mixed-membrane three-junctions. *J. Chem. Phys.* **2016**, *145*, 074901, DOI: 10.1063/1.4960433.

(34) Vanni, S.; Hirose, H.; Barelli, H.; Antonny, B.; Gautier, R. A sub-nanometre view of how membrane curvature and composition modulate lipid packing and protein recruitment. *Nat. Commun.* **2014**, *5*, 4916, DOI: 10.1038/ncomms5916.

(35) Reynwar, B. J.; Illya, G.; Harmandaris, V. A.; Müller, M. M.; Kremer, K.; Deserno, M. Aggregation and vesiculation of membrane proteins by curvature-mediated interactions. *Nature* **2007**, *447*, 461, DOI: 10.1038/nature05840.

(36) Magdeleine, M.; Gautier, R.; Gounon, P.; Barelli, H.; Vanni, S.; Antonny, B. A filter at the entrance of the Golgi that selects vesicles according to size and bulk lipid composition. *Elife* **2016**, *5*, e16988, DOI: 10.7554/elife.16988.

(37) Pinot, M.; Vanni, S.; Pagnotta, S.; Lacas-Gervais, S.; Payet, L.-A.; Ferreira, T.; Gautier, R.; Goud, B.; Antonny, B.; Barelli, H. Polyunsaturated phospholipids facilitate membrane deformation and fission by endocytic proteins. *Science* **2014**, *345*, 693–697, DOI: 10.1126/science.1255288.

(38) Kawamoto, S.; Klein, M. L.; Shinoda, W. Coarse-grained molecular dynamics study of membrane fusion: Curvature effects on free energy barriers along the stalk mechanism. *J. Chem. Phys.* **2015**, *143*, 243112, DOI: 10.1063/1.4933087.

(39) Mandal, T.; Koenig, P. H.; Larson, R. G. Nonmonotonic Scission and Branching Free Energies as Functions of Hydrotrope Concentration for Charged Micelles. *Phys. Rev. Lett.* **2018**, *121*, 038001, DOI: 10.1103/PhysRevLett.121.038001.

(40) Anderson, R. L.; Bray, D. J.; Del Regno, A.; Seaton, M. A.; Ferrante, A. S.; Warren, P. B. Micelle Formation in Alkyl Sulfate Surfactants Using Dissipative Particle Dynamics. *J. Chem. Theory Comput.* **2018**, *14*, 2633–2643, DOI: 10.1021/acs.jctc.8b00075.

(41) Sen, T. Z.; Feng, Y.; Garcia, J. V.; Kloczkowski, A.; Jernigan, R. L. The extent of cooperativity of protein motions observed with elastic network models is similar for atomic and coarser-grained models. *J. Chem. Theory Comput.* **2006**, *2*, 696–704, DOI: 10.1021/ct600060d.

(42) Clementi, C. Coarse-grained models of protein folding: toy models or predictive tools? *Curr. Opin. Struct. Biol.* **2008**, *18*, 10–15, DOI: 10.1016/j.sbi.2007.10.005.

(43) Bahar, I.; Atilgan, A. R.; Erman, B. Direct evaluation of thermal fluctuations in proteins using a single-parameter harmonic potential. *Fold. Des.* **1997**, *2*, 173–181, DOI: 10.1016/s1359-0278(97)00024-2.

(44) Micheletti, C.; Carloni, P.; Maritan, A. Accurate and efficient description of protein vibrational dynamics: comparing molecular dynamics and Gaussian models. *Proteins: Struct., Funct., Bioinf.* **2004**, *55*, 635–645, DOI: 10.1002/prot.20049.

(45) Bahar, I.; Kaplan, M.; Jernigan, R. Short-range conformational energies, secondary structure propensities, and recognition of correct sequence-structure matches. *Proteins: Struct., Funct., Bioinf.* **1997**, *29*, 292–308, DOI: 10.1002/(sici)1097-0134(199711)29:3<292::aid-prot4>3.3.co;2-5.

(46) Hills, R.; Brooks, C. Insights from coarse-grained Gō models for protein folding and dynamics. *Int. J. Mol. Sci.* **2009**, *10*, 889–905, DOI: 10.3390/ijms10030889.

(47) Cochran, A. G.; Skelton, N. J.; Starovasnik, M. A. Tryptophan zippers: Stable, monomeric β-hairpins. *Proc. Natl. Acad. Sci. U.S.A* **2001**, *98*, 5578–5583, DOI: 10.1073/pnas.091100898.

(48) Liwo, A.; Khalili, M.; Czaplewski, C.; Kalinowski, S.; Ołdziej, S.; Wachucik, K.; Scheraga, H. A. Modification and optimization of the united-residue (UNRES) potential energy function for canonical simulations. I. Temperature dependence of the effective energy function and tests of the optimization method with single training proteins. *J. Phys. Chem. B* **2007**, *111*, 260–285, DOI: 10.1021/jp065380a.

(49) Cascella, M.; Neri, M. A.; Carloni, P.; Dal Peraro, M. Topologically based multipolar reconstruction of electrostatic interactions in multiscale simulations of proteins. *J. Chem. Theory Comput.* **2008**, *4*, 1378–1385, DOI: 10.1021/ct800122x.

(50) Alemani, D.; Collu, F.; Cascella, M.; Dal Peraro, M. A Nonradial Coarse-Grained Potential for Proteins Produces Naturally Stable Secondary Structure Elements. *J. Chem. Theory Comput.* **2010**, *6*, 315–324, DOI: 10.1021/ct900457z.

(51) Bore, S. L.; Milano, G.; Cascella, M. Hybrid Particle-Field Model for Conformational Dynamics of Peptide Chains. *J. Chem. Theory Comput.* **2018**, *14*, 1120–1130, DOI: 10.1021/acs.jctc.7b01160.

(52) Knotts IV, T. A.; Rathore, N.; Schwartz, D. C.; de Pablo, J. J. A coarse grain model for DNA. *J. Chem. Phys.* **2007**, *126*, 02B611, DOI: 10.1063/1.2431804.

(53) Freeman, G. S.; Hinckley, D. M.; de Pablo, J. J. A coarse-grain three-site-per-nucleotide model for DNA with explicit ions. *J. Chem. Phys.* **2011**, *135*, 10B625, DOI: 10.1063/1.3652956.

(54) Hinckley, D. M.; Freeman, G. S.; Whitmer, J. K.; De Pablo, J. J. An experimentally-informed coarse-grained 3-site-per-nucleotide model of DNA: Structure, thermody-

namics, and dynamics of hybridization. *J. Chem. Phys.* **2013**, *139*, 10B604_1, DOI: 10.1063/1.4822042.

(55) Jendrejack, R. M.; de Pablo, J. J.; Graham, M. D. Stochastic simulations of DNA in flow: Dynamics and the effects of hydrodynamic interactions. *J. Chem. Phys.* **2002**, *116*, 7752–7759, DOI: 10.1063/1.1466831.

(56) Ouldridge, T. E.; Louis, A. A.; Doye, J. P. DNA nanotweezers studied with a coarse-grained model of DNA. *Phys. Rev. Lett.* **2010**, *104*, 178101, DOI: 10.1103/physrevlett.104.178101.

(57) Ouldridge, T. E.; Louis, A. A.; Doye, J. P. Extracting bulk properties of self-assembling systems from small simulations. *J. Phys.: Condens. Matter* **2010**, *22*, 104102, DOI: 10.1088/0953-8984/22/10/104102.

(58) Ouldridge, T. E.; Louis, A. A.; Doye, J. P. Structural, mechanical, and thermodynamic properties of a coarse-grained DNA model. *J. Chem. Phys.* **2011**, *134*, 02B627, DOI: 10.1063/1.3552946.

(59) Petkevičiūtė, D.; Pasi, M.; Gonzalez, O.; Maddocks, J. cgDNA: a software package for the prediction of sequence-dependent coarse-grain free energies of B-form DNA. *Nucleic Acids Res.* **2014**, *42*, e153–e153, DOI: 10.1093/nar/gku825.

(60) Roux, B.; Simonson, T. Implicit solvent models. *Biophys. Chem.* **1999**, *78*, 1–20, DOI: 10.1016/s0301-4622(98)00226-9.

(61) Hess, B.; Holm, C.; van der Vegt, N. Modeling multibody effects in ionic solutions with a concentration dependent dielectric permittivity. *Phys. Rev. Lett.* **2006**, *96*, 147801, DOI: 10.1103/physrevlett.96.147801.

(62) Vorobyov, I.; Li, L.; Allen, T. W. Assessing Atomistic and Coarse-Grained Force Fields

for ProteinLipid Interactions: the Formidable Challenge of an Ionizable Side Chain in a Membrane. *J. Phys. Chem. B* **2008**, *112*, 9588–9602, DOI: 10.1021/jp711492h.

(63) Hadley, K. R.; McCabe, C. Coarse-grained molecular models of water: a review. *Mol. Simul.* **2012**, *38*, 671–681, DOI: 10.1080/08927022.2012.671942.

(64) Florián, J.; Warshel, A. Calculations of hydration entropies of hydrophobic, polar, and ionic solutes in the framework of the Langevin dipoles solvation model. *J. Phys. Chem. B* **1999**, *103*, 10282–10288, DOI: 10.1021/jp992041r.

(65) Ha-Duong, T.; Basdevant, N.; Borgis, D. A polarizable coarse-grained water model for coarse-grained proteins simulations. *Chem. Phys. Lett.* **2009**, *468*, 79–82, DOI: 10.1016/j.cplett.2008.11.092.

(66) Motevaselian, M.; Mashayak, S.; Aluru, N. Extended coarse-grained dipole model for polar liquids: Application to bulk and confined water. *Phys. Rev. E* **2018**, *98*, 052135, DOI: 10.1103/physreve.98.052135.

(67) Yesylevskyy, S. O.; Schäfer, L. V.; Sengupta, D.; Marrink, S. J. Polarizable water model for the coarse-grained MARTINI force field. *PLoS Comput. Biol.* **2010**, *6*, e1000810, DOI: 10.1371/journal.pcbi.1000810.

(68) Riniker, S.; van Gunsteren, W. F. A simple, efficient polarizable coarse-grained water model for molecular dynamics simulations. *J. Chem. Phys.* **2011**, *134*, 084110, DOI: 10.1063/1.3553378.

(69) Darré, L.; Machado, M. R.; Dans, P. D.; Herrera, F. E.; Pantano, S. Another Coarse Grain Model for Aqueous Solvation: WAT FOUR? *J. Chem. Theory Comput.* **2010**, *6*, 3793–3807, DOI: 10.1021/ct100379f.

(70) Phillips, R.; Quake, S. R. The biological frontier of physics. *Phys. Today* **2006**, *59*, 38–43, DOI: 10.1063/1.2216960.

(71) Daoulas, K. C.; Cavallo, A.; Shenhar, R.; Müller, M. Phase behaviour of quasi-block copolymers: A DFT-based Monte-Carlo study. *Soft Matter* **2009**, *5*, 4499–4509, DOI: 10.1039/b911364a.

(72) Qi, S.; Schmid, F. Hybrid particle-continuum simulations coupling Brownian dynamics and local dynamic density functional theory. *Soft Matter* **2017**, *13*, 7938–7947, DOI: 10.1039/C7SM01749A.

(73) Vu, G. T.; Abate, A. A.; Gómez, L. R.; Pezzutti, A. D.; Register, R. A.; Vega, D. A.; Schmid, F. Curvature as a Guiding Field for Patterns in Thin Block Copolymer Films. *Phys. Rev. Lett.* **2018**, *121*, 087801, DOI: 10.1103/PhysRevLett.121.087801.

(74) Matsen, M. W.; Schick, M. Stable and unstable phases of a diblock copolymer melt. *Phys. Rev. Lett.* **1994**, *72*, 2660, DOI: 10.1103/physrevlett.72.2660.

(75) Drolet, F.; Fredrickson, G. H. Combinatorial screening of complex block copolymer assembly with self-consistent field theory. *Phys. Rev. Lett.* **1999**, *83*, 4317, DOI: 10.1103/physrevlett.83.4317.

(76) Balazs, A. C.; Singh, C.; Zhulina, E. Modeling the interactions between polymers and clay surfaces through self-consistent field theory. *Macromolecules* **1998**, *31*, 8370–8381, DOI: 10.1021/ma980727w.

(77) Dickinson, E.; Pinfield, V. J.; Horne, D. S.; Leermakers, F. A. Self-consistent-field modelling of adsorbed casein interaction between two protein-coated surfaces. *J. Chem. Soc., Faraday Trans.* **1997**, *93*, 1785–1790, DOI: 10.1039/a608417f.

(78) Kawakatsu, T.; Kawasaki, K. Hybrid models for the dynamics of an immiscible binary mixture with surfactant molecules. *Physica A* **1990**, *167*, 690–735, DOI: 10.1016/0378-4371(90)90287-3.

(79) Kawakatsu, T.; Kawasaki, K.; Furusaka, M.; Okabayashi, H.; Kanaya, T. Late stage dynamics of phase separation processes of binary mixtures containing surfactants. *J. Chem. Phys.* **1993**, *99*, 8200–8217, DOI: 10.1063/1.466213.

(80) Jackson, J. D. *Electrodynamics*; Wiley Online Library, 1975.

(81) Griffiths, D. J. *Introduction to electrodynamics*; Prentice Hall, 1962.

(82) Milano, G.; Kawakatsu, T. Hybrid particle-field molecular dynamics simulations for dense polymer systems. *J. Chem. Phys.* **2009**, *130*, 214106–8, DOI: 10.1063/1.3142103.

(83) Brevik, I. Experiments in phenomenological electrodynamics and the electromagnetic energy-momentum tensor. *Phys. Rep.* **1979**, *52*, 133–201, DOI: 10.1016/0370-1573(79)90074-7.

(84) Levy, A.; Andelman, D.; Orland, H. Dielectric constant of ionic solutions: A field-theory approach. *Physical review letters* **2012**, *108*, 227801.

(85) Debye, P.; Kleboth, K. Electrical Field Effect on the Critical Opalescence. *J. Chem. Phys.* **1965**, *42*, 3155–3162, DOI: 10.1063/1.1696394.

(86) Onuki, A.; Kitamura, H. Solvation effects in near-critical binary mixtures. *J. Chem. Phys.* **2004**, *121*, 3143–3151, DOI: 10.1063/1.1769357.

(87) Onuki, A. Ginzburg-Landau theory of solvation in polar fluids: Ion distribution around an interface. *Phys. Rev. E* **2006**, *73*, 021506, DOI: 10.1103/physreve.73.021506.

(88) Holst, M.; Saied, F. Multigrid solution of the PoissonBoltzmann equation. *J. Comput. Chem.* **1993**, *14*, 105–113, DOI: 10.1002/jcc.540140114.

(89) Tan, C.; Yang, L.; Luo, R. How Well Does PoissonBoltzmann Implicit Solvent Agree with Explicit Solvent? A Quantitative Analysis. *J. Phys. Chem. B* **2006**, *110*, 18680–18687, DOI: 10.1021/jp063479b.

(90) Sharp, K. Incorporating solvent and ion screening into molecular dynamics using the finite-difference Poisson–Boltzmann method. *J. Comput. Chem.* **1991**, *12*, 454–468, DOI: 10.1002/jcc.540120407.

(91) Davis, M. E.; McCammon, J. A. Solving the finite difference linearized Poisson-Boltzmann equation: A comparison of relaxation and conjugate gradient methods. *J. Comput. Chem.* **1989**, *10*, 386–391, DOI: 10.1002/jcc.540100313.

(92) Zhao, Y.; De Nicola, A.; Kawakatsu, T.; Milano, G. Hybrid particle-field molecular dynamics simulations: Parallelization and benchmarks. *J. Comput. Chem.* **2012**, *33*, 868–880, DOI: 10.1002/jcc.22883.

(93) De Nicola, A.; Kawakatsu, T.; Rosano, C.; Celino, M.; Rocco, M.; Milano, G. Self-assembly of Triton X-100 in water solutions: a multiscale simulation study linking mesoscale to atomistic models. *J. Chem. Theory Comput.* **2015**, *11*, 4959–4971, DOI: 10.1021/acs.jctc.5b00485.

(94) Lee, S. H.; Lee, S. B. Octanol/water partition coefficients of ionic liquids. *J. Appl. Chem. Biotechnol.* **2008**, *84*, 202–207, DOI: 10.1002/jctb.2025.

(95) Van Even, V.; Haulait-Pirson, M. C. Influence of the dielectric constant on ion-pair and ion-ligand complex formation. *J. Solution Chem.* **1977**, *6*, 757–770, DOI: 10.1007/bf00650452.

(96) Kolli, H. B.; de Nicola, A.; Bore, S. L.; Schäfer, K.; Diezemann, G.; Gauss, J.; Kawakatsu, T.; Lu, Z.-Y.; Zhu, Y.-L.; Milano, G.; Cascella, M. Hybrid Particle-Field Molecular Dynamics Simulations of Charged Amphiphiles in an Aqueous Environment. *J. Chem. Theory Comput.* **2018**, *14*, 4928–4937, DOI: 10.1021/acs.jctc.8b00466.

(97) Muller, R. U.; Finkelstein, A. The effect of surface charge on the voltage-dependent conductance induced in thin lipid membranes by monazomycin. *J. Gen. Physiol* **1972**, *60*, 285–306, DOI: 10.1085/jgp.60.3.285.

(98) Wang, L. Measurements and Implications of the Membrane Dipole Potential. *Annu. Rev. Biochem.* **2012**, *81*, 615–635, DOI: 10.1146/annurev-biochem-070110-123033.

(99) Vanegas, J. M.; Torres-Sánchez, A.; Arroyo, M. Importance of Force Decomposition for Local Stress Calculations in Biomembrane Molecular Simulations. *J. Chem. Theory Comput.* **2014**, *10*, 691–702, DOI: 10.1021/ct4008926.

(100) Daoulas, K. C.; Müller, M. Single chain in mean field simulations: Quasi-instantaneous field approximation and quantitative comparison with Monte Carlo simulations. *J. Chem. Phys.* **2006**, *125*, 184904, DOI: 10.1063/1.2364506.

(101) Daoulas, K. C.; Müller, M.; Stoykovich, M. P.; Kang, H.; de Pablo, J. J.; Nealey, P. F. Directed copolymer assembly on chemical substrate patterns: A phenomenological and single-chain-in-mean-field simulations study of the influence of roughness in the substrate pattern. *Langmuir* **2008**, *24*, 1284–1295, DOI: 10.1021/la702482z.

(102) Wang, J.; Müller, M. Microphase separation of mixed polymer brushes: dependence of the morphology on grafting density, composition, chain-length asymmetry, solvent quality, and selectivity. *J. Phys. Chem. B* **2009**, *113*, 11384–11402, DOI: 10.1021/jp903161j.

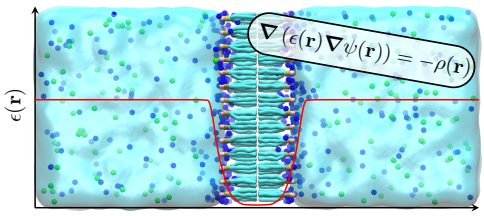
$\nabla(\epsilon(\mathbf{r})\nabla\psi(\mathbf{r})) = -\rho(\mathbf{r})$
$\epsilon(\mathbf{r})$

Supporting information for: Mesoscale electrostatics driving particle dynamics in non-homogeneous dielectrics

Sigbjørn Løland Bore,[†] Hima Bindu Kolli,[†,§] Toshihiro Kawakatsu,[‡] Giuseppe Milano,[¶] and Michele Cascella[*,†]

†*Department of Chemistry, and Hylleraas Centre for Quantum Molecular Sciences, University of Oslo, PO Box 1033 Blindern, 0315 Oslo, Norway*

‡*Department of Physics, Tohoku University, Aoba, Aramaki, Aoba-ku, Sendai 980-8578, Japan*

¶*Department of Organic Materials Science, Yamagata University, 4-3-16 Jonan Yonezawa, Yamagata-ken 992-8510, Japan*

§*Present address: Department of Physics and Astronomy, The University of Sheffield, United Kingdom*

E-mail: michele.cascella@kjemi.uio.no

Contents

1 Derivation of external electrostatic potential

The total electrostatic energy of a system can be written as:

$$W_{\text{elec}}[\{\phi(\mathbf{r})\}, \mathbf{D}(\mathbf{r})] = \frac{1}{2}\int \mathrm{d}\mathbf{r} \frac{\mathbf{D}(\mathbf{r}) \cdot \mathbf{D}(\mathbf{r})}{\epsilon(\{\phi(\mathbf{r})\})}, \tag{1}$$

where $\mathbf{D}$ is the electrostatic displacement field. In hPF, pairwise interactions are replaced by an interaction with an external field $V_{\text{ext},k}(\mathbf{r})$, specific for the particle type. This potential is obtained through:

$$V_{\text{ext},k}(\mathbf{r}) = \frac{\delta W}{\delta \phi_k(\mathbf{r})}. \tag{2}$$

To take the functional derivative we must take into account dependence on density through $\epsilon(\mathbf{r}) = \epsilon(\{\phi(\mathbf{r})\})$ and $\mathbf{D}(\mathbf{r})$. This is done by applying the chain rule:

$$V_{\text{ext},k}(\mathbf{r}) = \int \mathrm{d}\mathbf{r}' \left(\frac{\delta W_{\text{elec}}}{\delta \mathbf{D}(\mathbf{r}')} \frac{\delta \mathbf{D}(\mathbf{r}')}{\delta \phi_k(\mathbf{r})} + \frac{\delta W_{\text{elec}}}{\delta \epsilon(\mathbf{r}')} \frac{\delta \epsilon(\mathbf{r}')}{\delta \phi_k(\mathbf{r})} \right) \tag{3}$$

or

$$V_{\text{ext},k}(\mathbf{r}) = A(\mathbf{r}) + B(\mathbf{r}), \tag{4}$$

where

$$A(\mathbf{r}) \equiv \int \mathrm{d}\mathbf{r}' \frac{\delta W_{\text{elec}}}{\delta \mathbf{D}(\mathbf{r}')} \frac{\delta \mathbf{D}(\mathbf{r}')}{\delta \phi_k(\mathbf{r})}, \tag{5a}$$

$$B(\mathbf{r}) \equiv \int \mathrm{d}\mathbf{r}' \frac{\delta W_{\text{elec}}}{\delta \epsilon(\mathbf{r}')} \frac{\delta \epsilon(\mathbf{r}')}{\delta \phi_k(\mathbf{r})}. \tag{5b}$$

$A(\mathbf{r})$ is composed of two functional derivatives. The first part, the functional derivative of the interaction energy with respect to $\mathbf{D}$, we derive as follows:

$$\begin{aligned} \frac{\delta W_{\text{elec}}}{\delta \mathbf{D}(\mathbf{r}')} &= \int \mathrm{d}\mathbf{r} \frac{\delta}{\delta \mathbf{D}(\mathbf{r}')} \frac{\mathbf{D}(\mathbf{r})\mathbf{D}(\mathbf{r})}{2\epsilon(\mathbf{r})} = \int \mathrm{d}\mathbf{r} \frac{\mathbf{D}(\mathbf{r})}{\epsilon(\mathbf{r})} \frac{\delta \mathbf{D}(\mathbf{r})}{\delta \mathbf{D}(\mathbf{r}')} \\ &= \frac{\mathbf{D}(\mathbf{r}')}{\epsilon(\mathbf{r}')} = -\boldsymbol{\nabla}' \psi(\mathbf{r}'), \end{aligned} \tag{6}$$

where $\boldsymbol{\nabla}'$ is the gradient with respect to $\mathbf{r}'$. Here, we have assumed a linear dielectric, and we have used that the displacement field can be written in terms of $\psi(\mathbf{r})$ as follows:

$$\mathbf{D}(\mathbf{r}) = -\epsilon(\mathbf{r}) \boldsymbol{\nabla} \psi(\mathbf{r}). \tag{7}$$

Next, using (6) and integration by parts, we can rewrite $A(\mathbf{r})$:

$$A(\mathbf{r}) = -\int \mathrm{d}\mathbf{r}' \boldsymbol{\nabla} \psi(\mathbf{r}') \frac{\delta \mathbf{D}(\mathbf{r}')}{\delta \phi_k(\mathbf{r})} = \int \mathrm{d}\mathbf{r}' \psi(\mathbf{r}') \boldsymbol{\nabla} \cdot \frac{\delta \mathbf{D}(\mathbf{r}')}{\delta \phi_k(\mathbf{r})}. \tag{8}$$

The Maxwell equation for displacement field, with explicit density dependence of charge density $\rho(\mathbf{r})$ gives:

$$\boldsymbol{\nabla} \cdot \mathbf{D}(\mathbf{r}) = \rho(\mathbf{r}) = \sum_{k=1}^{M} \phi_k(\mathbf{r}) q_k. \tag{9}$$

From (9), assuming operations commute, we apply functional derivative and obtain:

$$\boldsymbol{\nabla} \cdot \frac{\delta \mathbf{D}(\mathbf{r})}{\delta \phi_k(\mathbf{r}')} = q_k \delta(\mathbf{r} - \mathbf{r}'). \tag{10}$$

Using (10), we get the full expression:

$$A(\mathbf{r}) = \int \mathrm{d}\mathbf{r}' \psi(\mathbf{r}') q_k \delta(\mathbf{r} - \mathbf{r}') = q_k \psi(\mathbf{r}). \tag{11}$$

Assuming local dependence of ϵ on ϕ_k, (5) can be written as:

$$B(\mathbf{r}) = \frac{\partial \epsilon(\mathbf{r})}{\partial \phi_k(\mathbf{r})} \frac{\delta W_{\text{elec}}}{\delta \epsilon(\mathbf{r})}, \tag{12}$$

The functional derivative in (12) is obtained by:

$$\begin{aligned} \frac{\delta W_{\text{elec}}}{\delta \epsilon(\mathbf{r})} &= \frac{\delta}{\delta \epsilon(\mathbf{r})} \frac{1}{2} \int \mathrm{d}\mathbf{r}' \frac{\mathbf{D}(\mathbf{r}') \cdot \mathbf{D}(\mathbf{r}')}{\epsilon(\mathbf{r}')} \\ &= \frac{1}{2} \int \mathrm{d}\mathbf{r}' \mathbf{D}(\mathbf{r}') \cdot \mathbf{D}(\mathbf{r}') \frac{\partial}{\partial \epsilon(\mathbf{r}')} \left(\frac{1}{\epsilon(\mathbf{r}')} \right) \frac{\delta \epsilon(\mathbf{r}')}{\delta \epsilon(\mathbf{r})} \\ &= -\frac{1}{2} \int \mathrm{d}\mathbf{r}' \frac{\mathbf{D}(\mathbf{r}') \cdot \mathbf{D}(\mathbf{r}')}{\epsilon(\mathbf{r}')^2} \delta(\mathbf{r} - \mathbf{r}') \\ &= -\frac{1}{2} \frac{\mathbf{D}(\mathbf{r}) \cdot \mathbf{D}(\mathbf{r})}{\epsilon(\mathbf{r})^2}, \end{aligned} \tag{13}$$

where we used that

$$\frac{\delta \epsilon(\mathbf{r}')}{\delta \epsilon(\mathbf{r})} = \delta(\mathbf{r} - \mathbf{r}'). \tag{14}$$

Inserting (13) into (5a), we find:

$$B(\mathbf{r}) = -\frac{1}{2} \frac{\partial \epsilon(\mathbf{r})}{\partial \phi_k(\mathbf{r})} \frac{\mathbf{D}(\mathbf{r}) \cdot \mathbf{D}(\mathbf{r})}{\epsilon(\mathbf{r})^2} \tag{15}$$

Finally, the external potential can be written as:

$$V_{\text{ext},k} = q_k \psi(\mathbf{r}) - \frac{1}{2} \frac{\partial \epsilon(\mathbf{r})}{\partial \phi_k(\mathbf{r})} (\boldsymbol{\nabla} \psi(\mathbf{r}))^2. \tag{16}$$

2 Relationship to the Helmholtz force density

Focusing on polarization term, the force contribution to a volume can be written as:

$$\mathbf{F} = \frac{1}{2}\int \mathrm{d}\mathbf{r} \sum_k \phi_k(\mathbf{r}) \boldsymbol{\nabla} \left(\frac{\partial \epsilon(\mathbf{r})}{\partial \phi_k} (\boldsymbol{\nabla}\psi(\mathbf{r}))^2 \right), \tag{17}$$

Using the product rule, we obtain

$$\mathbf{F} = \frac{1}{2}\int \mathrm{d}\mathbf{r} \sum_k \left(\boldsymbol{\nabla}(\phi_k(\mathbf{r}) \frac{\partial \epsilon(\mathbf{r})}{\partial \phi_k} (\boldsymbol{\nabla}\psi(\mathbf{r}))^2) - \boldsymbol{\nabla}\phi_k(\mathbf{r}) \frac{\partial \epsilon(\mathbf{r})}{\partial \phi_k} (\boldsymbol{\nabla}\psi(\mathbf{r}))^2 \right). \tag{18}$$

Equation (18) can be rewritten, by using

$$\boldsymbol{\nabla}\epsilon(\mathbf{r}) = \sum_k \boldsymbol{\nabla}\phi_k(\mathbf{r}) \frac{\partial \epsilon(\mathbf{r})}{\partial \phi_k}, \tag{19}$$

as:

$$\mathbf{F} = \frac{1}{2}\int \mathrm{d}\mathbf{r} \left(\boldsymbol{\nabla} \left(\sum_{\mathrm{k}} \phi_{\mathrm{k}}(\mathbf{r}) \frac{\partial \epsilon(\mathbf{r})}{\partial \phi_{\mathrm{k}}} (\boldsymbol{\nabla}\psi(\mathbf{r}))^2 \right) - \boldsymbol{\nabla}\epsilon(\mathbf{r}) (\boldsymbol{\nabla}\psi(\mathbf{r}))^2 \right). \tag{20}$$

The force density per volume is given by the integrand:

$$\mathbf{f}_{\mathrm{pol}} = \frac{1}{2}\boldsymbol{\nabla} \left(\sum_k \phi_k(\mathbf{r}) \frac{\partial \epsilon(\mathbf{r})}{\partial \phi_k} (\boldsymbol{\nabla}\psi(\mathbf{r}))^2 \right) - \frac{1}{2}\boldsymbol{\nabla}\epsilon(\mathbf{r}) (\boldsymbol{\nabla}\psi(\mathbf{r}))^2, \tag{21}$$

which for a single-component fluid is the Helmholtz force density.[S1] We note that, for a weighted average for $\epsilon(\mathbf{r})$, the first term sum to zero.

3 Numerical solution of GPE

A regular grid with periodic boundary conditions is used with box of size $L_x \times L_y \times L_z$ discretized by N_x, N_y and N_z points in each direction respectively. The position of the nodes are given by $x_i = i \cdot \Delta x$, $y_j = j \cdot \Delta y$, $z_k = k \cdot \Delta z$, where $\Delta x \equiv L_x/N_x$, $\Delta y \equiv L_y/N_y$ and $\Delta z \equiv L_z/N_z$. On the nodes, $\epsilon(\mathbf{r})$, $\rho(\mathbf{r})$, $\psi(\mathbf{r})$ are discretized as $\epsilon_{i,j,k}$, $\rho_{i,j,k}$, $\psi_{i,j,k}$. We

derive a finite difference scheme by approximating derivatives in GPE with central differences on half points between nodes:

$$\begin{aligned}
&\frac{1}{\Delta x}\left(\left(\epsilon\frac{\partial\psi}{\partial x}\right)_{i+1/2,j,k}-\left(\epsilon\frac{\partial\psi}{\partial x}\right)_{i-1/2,j,k}\right)+\\
&\frac{1}{\Delta y}\left(\left(\epsilon\frac{\partial\psi}{\partial y}\right)_{i,j+1/2,k}-\left(\epsilon\frac{\partial\psi}{\partial y}\right)_{i,j-1/2,k}\right)+\\
&\frac{1}{\Delta z}\left(\left(\epsilon\frac{\partial\psi}{\partial z}\right)_{i,j,k+1/2}-\left(\epsilon\frac{\partial\psi}{\partial z}\right)_{i,j,k-1/2}\right)=-\rho_{i,j,k},
\end{aligned} \tag{22}$$

which gives

$$\begin{aligned}
&\frac{1}{\Delta x^2}\left(\epsilon_{i+1/2,j,k}(\psi_{i+1,j,k}-\psi_{i,j,k})-\right.\\
&\qquad\left.\epsilon_{i-1/2,j,k}(\psi_{i,j,k}-\psi_{i-1,j,k})\right)+\\
&\frac{1}{\Delta y^2}\left(\epsilon_{i,j+1/2,k}(\psi_{i,j+1,k}-\psi_{i,j,k})-\right.\\
&\qquad\left.-\epsilon_{i,j-1/2,k}(\psi_{i,j,k}-\psi_{i,j-1,k})\right)+\\
&\frac{1}{\Delta z^2}\left(\epsilon_{i,j,k+1/2}(\psi_{i,j,k+1}-\psi_{i,j,k})-\right.\\
&\qquad\left.\epsilon_{i,j,k-1/2}(\psi_{i,j,k}-\psi_{i,j,k-1})\right)=-\rho_{i,j,k},
\end{aligned} \tag{23}$$

where

$$\epsilon_{i+1/2,j,k}\equiv\frac{1}{2}\left(\epsilon_{i+1,j,k}+\epsilon_{i,j,k}\right). \tag{24}$$

GPE can be rewritten in finite difference form as follows:

$$\begin{aligned}
&a_1\psi_{i+1,j,k}+a_2\psi_{i-1,j,k}+\\
&a_3\psi_{i,j+1,k}+a_4\psi_{i,j-1,k}+\\
&a_5\psi_{i,j,k+1}+a_6\psi_{i,j,k-1}-\\
&\qquad a_0\psi_{i,j,k}=-\rho_{i,j,k},
\end{aligned} \tag{25}$$

where we identify the a_k from equation (23) as:

$$a_1 = \frac{1}{2\Delta x^2}\left(\epsilon_{i-1,j,k} + \epsilon_{i,j,k}\right), \tag{26a}$$

$$a_2 = \frac{1}{2\Delta x^2}\left(\epsilon_{i,j,k} + \epsilon_{i+1,j,k}\right), \tag{26b}$$

$$a_3 = \frac{1}{2\Delta y^2}\left(\epsilon_{i,j-1,k} + \epsilon_{i,j,k}\right), \tag{26c}$$

$$a_4 = \frac{1}{2\Delta y^2}\left(\epsilon_{i,j,k} + \epsilon_{i,j+1,k}\right), \tag{26d}$$

$$a_5 = \frac{1}{2\Delta z^2}\left(\epsilon_{i,j,k-1} + \epsilon_{i,j,k}\right), \tag{26e}$$

$$a_6 = \frac{1}{2\Delta z^2}\left(\epsilon_{i,j,k} + \epsilon_{i,j,k+1}\right), \tag{26f}$$

and

$$a_0 = a_1 + a_2 + a_3 + a_4 + a_4 + a_6. \tag{27}$$

Solving equation (25) is equivalent to solving a system of banded linear equations, for which many methods exist (note that the accuracy is not related to the method for solving the set of equations, but the finite difference discretization). Widely used methods include Multigrid method,[S2] Conjugate gradient,[S3] or relaxation methods like Jacobi, Gauss-Seidel and successive over relaxation (SOR).[S3] Here, we employ SOR because of good efficiency and ease of implementation.

The SOR-method solves GPE iteratively by:

$$\psi^{n+1}_{i,j,k} = (1-\omega)\psi^{n}_{i,j,k} + \frac{\omega}{a_0}\left(\rho_{i,j,k} + a_1\psi^{n}_{i+1,j,k} + .a_2\psi^{n}_{i-1,j,k} + a_3\psi^{n}_{i,j+1,k} + a_4\psi^{n}_{i,j-1,k} + a_5\psi^{n}_{i,j,k+1} + a_6\psi^{n}_{i,j,k-1}\right), \tag{28}$$

where n is marks the number of iterations and ω is a relaxation parameter crucial for the convergence-rate. We use $\omega = 2.0/(1.0 + \sin(\pi/N_x))$ in accordance with.[S4] As convergence criteria we employ:

$$\left\langle \left|\psi^{n+1}_{i,j,k} - \psi^{n}_{i,j,k}\right| \right\rangle < 1 \times 10^{-6}\,\mathrm{mV}. \tag{29}$$

The number of iterations required for for convergence is dependent on system and the time δt between potential updates. Figure S1 provides the number of iterations N_{it} required for achieving (29) for a charge lipid bilayer.

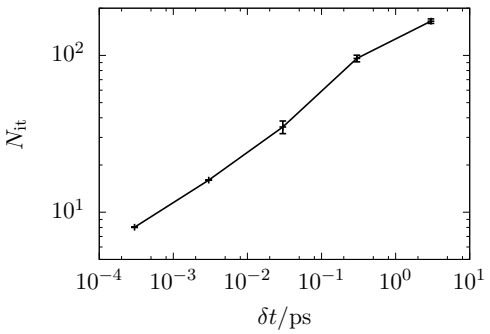

Figure S1: Mean number of steps required for convergence as function of time δt between potential updates. This particular convergence test was performed on a equilibrated charged lipid bilayer with $\epsilon_{1,80}$. Details on this system are reported in Appendix 4.2.

4 Simulation details

Settings used for molecular dynamics are provided in Table S1. All simulations are done under periodic boundary conditions

Table S1: Settings used in OCCAM simulations.

Δt[a]/ps	δt[b]/ps	δt[c]/ps	f_{col}[d]/ps^{-1}	T/K	b/nm	κ^{-1}/kJ mol^{-1}
0.03	3	0.3	7	301.15	0.65	20

[a]Time step.
[b]Time between grid update for partitioning simulations.
[c]Time between grid update for membrane simulations.
[d]Collision frequency of Andersen thermostat.

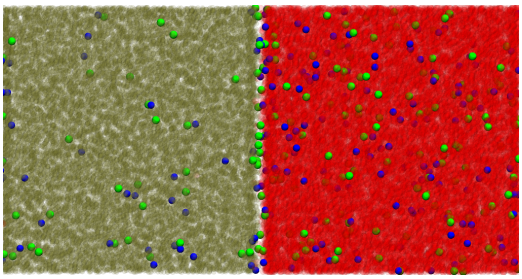

Figure S2: Random snapshot from a hPF-MD/e simulation of a 200 mM salt concentration in a oil/water bi-phase solution, using $\epsilon_o = 10$. The oil beads are colored in dark green, the water beads in red; positive and negative ions are represented by light green and blue spheres.

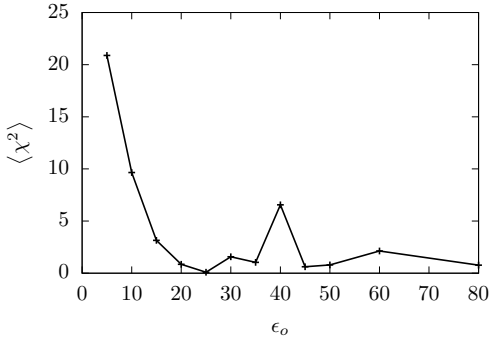

Figure S3: The $\langle \chi^2 \rangle$ of fitting for concentration dependence of $D_{o/W}$ for different ϵ_o.

4.1 Partitioning simulations

The partitioning simulations are done in a box of dimensions 29.8 nm × 14.9 nm × 14.9 nm, starting phase separated with oil on left side ($x < 14.9$ nm) and water on right side (14.9 nm $< x <$ 29.8 nm). The initial phase separation is maintained throughout the simulation by $\chi_{o,w} \times RT = 30\,\mathrm{kJ\,mol^{-1}}$. Ions are only subject to compressibility condition and electrostatic interactions $\chi_{\mathrm{ion,j}} \times RT = 0$. The simulations are performed with $\epsilon_w = 80$, $\epsilon_{\mathrm{ion}} = 80$ and $\epsilon_o = \{5, 10, 15, 20, 25, 35, 40, 45, 50, 60, 80\}$. All beads are set to a mass 72 amu. The simulations last for a total time $t = 0.97\,\mu$s. The distribution coefficient is calculated by the

time average:

$$D_{o/w} = \frac{1}{n_{\text{frames}}} \sum_{i=1}^{n_{\text{frames}}} \frac{N^i_{A^+o} + N^i_{B^-o}}{N^i_{A^+w} + N^i_{B^-w}}, \tag{30}$$

where the number of ions in each phase are counted away from the interface. The corresponding standard deviations of the mean are estimated using block averaging.[S5] For each ϵ_o from concentration dependence of $D_{o/w}$, equilibria constants are obtained by optimizing:

$$\langle \chi^2 \rangle = \left\langle \left(\frac{(\log D_{o/w} - \log D_{o/w,\text{fit}}}{\sigma_{\log D_{o/w,}}} \right)^2 \right\rangle \tag{31}$$

for equilibria constants, constraining $K_w = 250\,\text{mM}$. The $\langle \chi^2 \rangle$ for different ϵ_o are reported in Figure S3.

Table S2: System setup for ion concentration dependence of partitioning. The simulation box is $29.8 \times 14.9 \times 14.9$ nm^3 and there are 55200 solvent beads (27600 oil and 27600 water beads). $N_{\text{A}^+\text{B}^-}$ denotes number of A^+ and B^- ions.

c_{ion}/mM	5	10	25	50	100	150	200
$N_{\text{A}^+\text{B}^-}$	20	40	100	200	400	600	800

4.2 Membrane simulations

Table S3: $\chi_{ij} \times RT$/kJ mol^{-1}-matrix for membrane simulations.

	L	P	G	C	D	A^+	B^-	W
L	0.00	-3.60	4.50	13.25	9.30	0.00	0.00	0.00
P	-3.60	0.00	4.50	13.50	11.70	0.00	0.00	-3.60
G	4.50	4.50	0.00	6.30	6.30	0.00	0.00	4.50
C	13.25	13.50	6.30	0.00	0.00	0.00	0.00	33.75
D	9.30	11.70	6.30	0.00	0.00	0.00	0.00	23.25
A^+	0.00	0.00	0.00	0.00	0.00	0.00	0.00	0.00
B^-	0.00	0.00	0.00	0.00	0.00	0.00	0.00	0.00
W	0.00	-3.60	4.50	33.75	23.25	0.00	0.00	0.00

The ion membrane simulations are performed with lipid positions frozen in time. The initial setup for the bilayer are made using *insane*,[S6] a tool for creating initial setup for

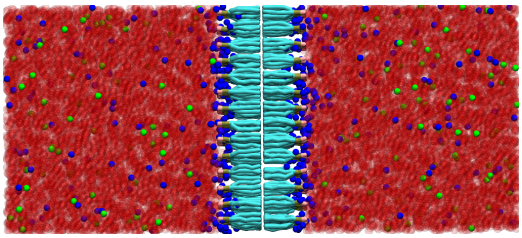

Figure S4: Snapshot of membrane simulation for charged lipid bilayer with salt. $\epsilon_{mem} = 1$ and $\epsilon_w = 80$. Water beads are colored in red, A^+ and B^- ions are represented by light green and blue spheres. The lipids are represented in sticks.

membranes. The polar/charged bilayers are composed of 391/392 lipids, respectively, placed along the xy-plane of a simulation box of $10.18 \times 10.18 \times 23.29\,\mathrm{nm}^3$ dimensions. The polar membrane was simulated in the presence of 145 A^+B^- ion couples, and 15887 water beads. The charged system contained 537 A^+ and 145 B^- ions, as well as 15495 waters. The χ_{ij}-matrix used for modeling intermolecular interactions is provided in Table S3. A snapshot of the simulation setup for a charged membrane is shown in Figure S4.

References

(S1) Brevik, I. Experiments in phenomenological electrodynamics and the electromagnetic energy-momentum tensor. *Phys. Rep.* **1979**, *52*, 133–201, DOI: 10.1016/0370-1573(79)90074-7.

(S2) Holst, M.; Saied, F. Multigrid solution of the PoissonBoltzmann equation. *J. Comput. Chem.* **1993**, *14*, 105–113, DOI: 10.1002/jcc.540140114.

(S3) Davis, M. E.; McCammon, J. A. Solving the finite difference linearized Poisson-Boltzmann equation: A comparison of relaxation and conjugate gradient methods. *J. Comput. Chem.* **1989**, *10*, 386–391, DOI: 10.1002/jcc.540100313.

(S4) Yang, S.; Gobbert, M. K. The optimal relaxation parameter for the SOR method

applied to the Poisson equation in any space dimensions. *Appl. Math. Lett.* **2009**, *22*, 325–331, DOI: 10.1016/j.aml.2008.03.028.

(S5) Flyvbjerg, H.; Petersen, H. G. Error estimates on averages of correlated data. *J. Chem. Phys.* **1989**, *91*, 461–466, DOI: 10.1007/bfb0105461.

(S6) Wassenaar, T. A.; Ingólfsson, H. I.; Böckmann, R. A.; Tieleman, D. P.; Marrink, S. J. Computational Lipidomics with insane: A Versatile Tool for Generating Custom Membranes for Molecular Simulations. *J. Chem. Theory Comput.* **2015**, *11*, 2144–2155, DOI: 10.1021/acs.jctc.5b00209.

Paper IV

Aggregation of Lipid A Variants: a Hybrid Particle-Field Model

Antonio De Nicola, Thereza A. Soares, Denys E. S. Santos, Sigbjørn Løland Bore, G. J. Agur Sevink, Michele Cascella, Giuseppe Milano

BBA – General Subjects, in press (2020)

IV

Paper V

Beyond the Molecular Packing Model: Understanding Morphological Transitions of Charged Surfactant Micelles

Ken Schäfer, Hima Bindu Kolli, Mikkel Killingmoe Christensen, Sigbjørn Løland Bore, Gregor Diezemann, Jürgen Gauss, Giuseppe Milano, Reidar Lund, Michele Cascella

Submitted for peer-review (2020)

V

Paper VI

Hybrid Particle-Field Molecular Dynamics Under Constant Pressure

Sigbjørn Løland Bore, Hima Bindu Kolli, Antonio De Nicola, Maksym Byshkin, Toshihiro Kawakatsu, Giuseppe Milano, Michele Cascella

The Journal of Chemical Physics, in press (2020)